6 Ultrafast spectroscopy on the doped single-layer copper oxide Bi2201

6.1 Electronic structure

The structure of all members of the series Bi-cuprates are formed by deficient perovskite-like blocks intercalated by Bi-O bilayers. In the $n = 1$ phase (Bi2201) the perovskite-like blocks contains just one CuO2 layer. In the $n = 2$ (Bi2212) and $n = 3$ (Bi2223) phases (see Figure 6.1), the perovskite-like block contain 2 and 3 CuO2 layers, respectively, separated by La/Sr atoms. The averaged structure are described by unit cells with parameters $a = 5.362$ Å , $b = 5.374$ Å, $c = 24.622$ Å, 30.9 Å and 37 Å for Bi2201, Bi2212, Bi2223 respectively. However, cation substitutions, oxygen off-stoichiometry, difference in translation periods of different layers make the real structure of these compounds much more complicated.
The peculiarities of their crystal structure make them very attractive beyond their superconducting properties (a complete review on the crystal structure of the High-Tc cuprates superconductors can be find in [Park and Snyder, 1995]). Their structure exhibits a characteristic incommensurate modulation, with a modulation vector $\mathbf{q} = \lambda_1 \mathbf{a}^* + \lambda_2 \mathbf{c}^*$. The origin of this structure modulation and its effect on the superconductive phase is still debated. A detailed study on this modulation can be found in [Finnemore et al., 2001]. The sample used in this work is a single-layer crystal $Bi_2Sr_{2-x}La_xCuO_{6+\delta}$ (see Figure 6.2). The x in this stoichiometric formula means that stronzium atoms can be substituted by the lantanium with a doping technique that changes abruptly the properties of the compound.

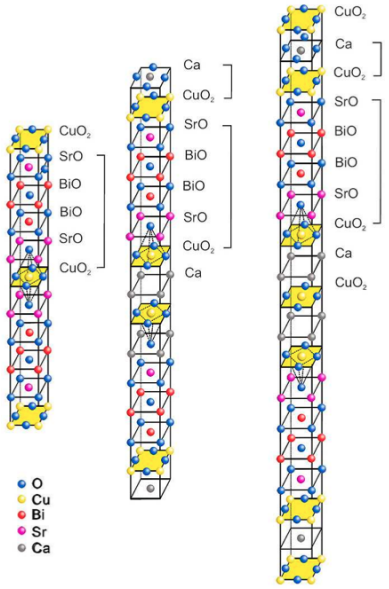

Figure 6.1: Tetragonal crystallographic unit cells of the Bismuth-cuprate series. From left to right the one-layer (Bi2201), two-layer (Bi2212), and three-layer (Bi2223) variations are shown.

6.2 Doping

In the single Cu-O layer cuprate $Bi_2Sr_{2-x}La_xCuO_{6+\delta}$ hole doping can be accurately controlled by replacing Sr by La. By choosing which combinations of outside layers are used for dopant oxygen atoms, T_C of cuprates may be raised up to 164 K. The relationship between T_C

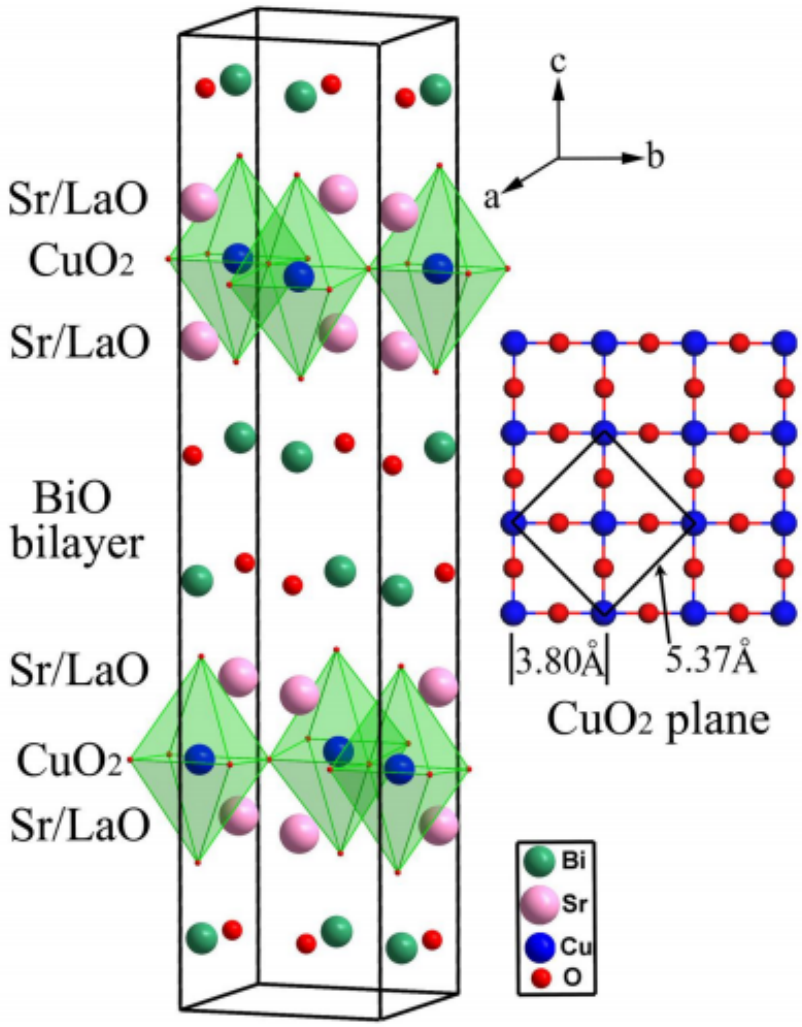

Figure 6.2: Basic crystal structure of $Bi_2Sr_{2-x}La_xCuO_{6+\delta}$. Unit cell parameters are $a = 5.362$ Å, $b = 5.374$ Å, $c = 24.622$ Å. The CuO_2 plane is also schematically shown in the figure. [Chen et al., 2013]

and the number of carriers p in hole-doped cuprate superconductors is universal and independent on the variety of the chemical and structural complexes hosting superconducting CuO_2 layers. In this relationship T_C is maximum at $p_{opt} = 0.16$ [Rohler, 2020]. In the specific case of $Bi_2Sr_{2-x}La_xCuO_{6+\delta}$ superconductivity starts at $p \geqslant 0.10$ and fades away already at $p \geqslant 0.22$. In Figure 6.3 taken from [Ono and Ando, 2003] the in-plane resistivity as a function of the temperature for several doping level samples of $Bi_2Sr_{2-x}La_xCuO_{6+\delta}$ is shown.

The samples starts to be superconductor at $p \geqslant 0.10$ while, for lower doping, the resistivity diverges approaching zero temperature. At $p = 0.16$ the temperature where the resistivity drops to zero is maximum. The optimal doping is unaffected by different crystal growth routes, varying Pb^{+3}/Bi^{+3} substitutions, and maxima range from 18 K in poly to 34 K in monocrystalline samples. La^{3+}/Sr^{2+} substitution in BSCO is chemically correlated with the insertion of excess oxygen atoms between the "insulating" Bi^{3+}-O, and "separating" La^{3+}/Sr^{2+}-O layers. The excess oxygen atoms may reside at interstitial "A" and "B" sites, close to the octahedral apex and to the octahedral faces, respectively (see Figure 6.4). La^{3+} bonds both, O^A and O^B, but, while O^A may oxidize the CuO_2 layers, O^B may compensate just the La^{3+}/Sr^{2+} charge contrast. In Figure 6.5 [Rohler, 2020] the relation between the lanthanum concentration x and the total number of oxygen excesses atoms $\delta = \delta_{O^A} + \delta_{O^B}$ has been modelled by a tilted "roof" (thick green line). It peaks at $\delta = 0.33$ for $x = 0.33$. In the La−rich regime the sample is insulating and antiferromagnetic, hence accommodates only $\delta = 0.5$ oxygen excess atoms in a nonoxidizing $[2La\text{-}O^B]_{0.5}$ reactant. Removal of La^{3+} from the parent compound will nominally redistribute up to $\delta = 0.5$ oxygen excess atoms from B to oxidizing A sites in the reactant $[O^A\text{-}La\text{-}O^B]_{0.5}$.

The nonoxidizing fraction follows the thin blue diagonal line and the separation between the green and the blue line gives the effective oxidizing oxygen excess atoms that is the actual doping. As indicated by the red vertical arrow in Figure 6.5, $x_{opt} = 0.33$ dopes $p_{opt} = 0.165$ holes.

For our work we have used the same sample of single layer La in $Bi_2Sr_{2-x}La_xCuO_{6+\delta}$ for six different level of doping with respective critical temperature shown in Table 6.1. The level of doping for which the critical temperature T_C is maximum is called *optimal doping* (OP). In our case it is $p = 0.16$ so that sample will be called OP16. When the doping is lower than the optimal value, the samples are called Under-Doped (UD); when the doping is higher than the optimal value, we will use the label (OD) that stands for Over-Doped.

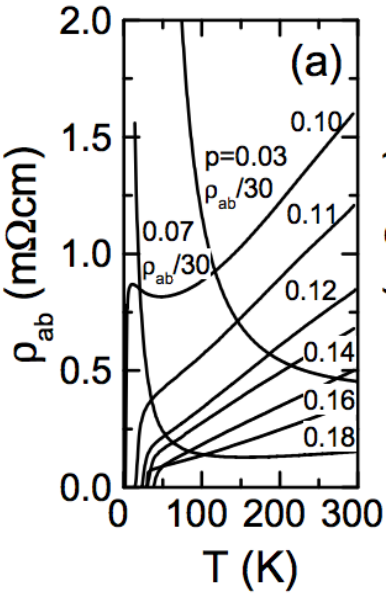

Figure 6.3: Temperature dependences of the in-plane resistivity ρ_{ab} of the $Bi_2Sr_{2-x}La_xCuO_{6+\delta}$ crystals for various p. [Ono and Ando, 2003]

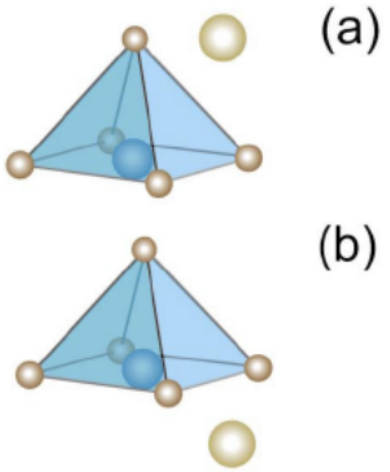

Figure 6.4: a) The excess of oxygen atoms can reside close to the octahedral apex: *A-site disorder*. It strongly couple to apical oxygen. b) *B-site disorder*: does not couple to apical oxygen.

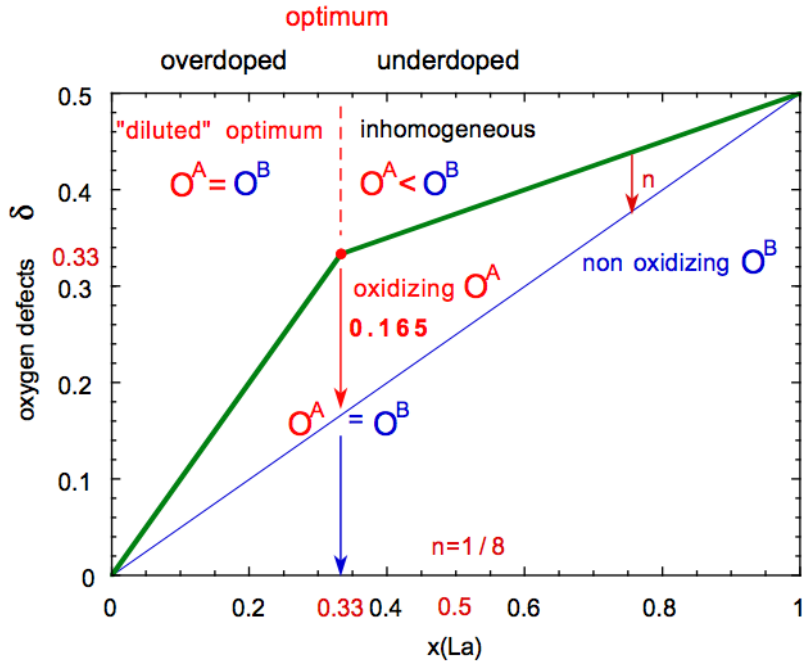

Figure 6.5: Number of oxygen excess atoms at interstitial A and B sites as a function of La in $Bi_2Sr_{2-x}La_xCuO_{6+\delta}$. O^B compensates theLa^{3+}/Sr^{2+} charge contrast, O^A oxidizes the CuO_2 layers. Resulting hole numbers n are indicated by the vertical arrows. The universal optimum $n_{opt} \simeq 0.16$ occurs for $x = 0.33$.

La Concentration x	Hole doping p (%)	$T_C(K)$	Sample Label
1.0	0.03	/	UD03
0.8	0.10	/	UD10
0.7	0.12	13	UD12
0.6	0.13	17	UD13
0.4	0.16	33	OP16
0.2	0.18	19	OD18

Table 6.1: Lantanum concentration, percentage of hole doping and critical temperature of the six samples analysed in this work.

6.3 *Optical Properties at Equilibrium*

In Figure 6.6 the real part of the optical conductivity $\sigma_1(\omega)$ and the reflectivity $R(\omega)$ as a function of the hole doping is reported. These measurements have been provided by S.Lupi and have been already published in [Lupi et al., 2009]. The $ab-$plane reflectivity $R(\omega)$ of the five samples was measured at near-normal incidence from ~ 0 to 2.72 eV at different T, shortly after cleaving the sample. The real part of the optical conductivity $\sigma_1(\omega)$, is obtained from $R(\omega)$ via Kramers-Kronig tranformations. The extrapolations to high frequency were based on the data of [Terasaki et al., 1990] and those to zero frequency on Drude-Lorentz fits. Looking at the very low

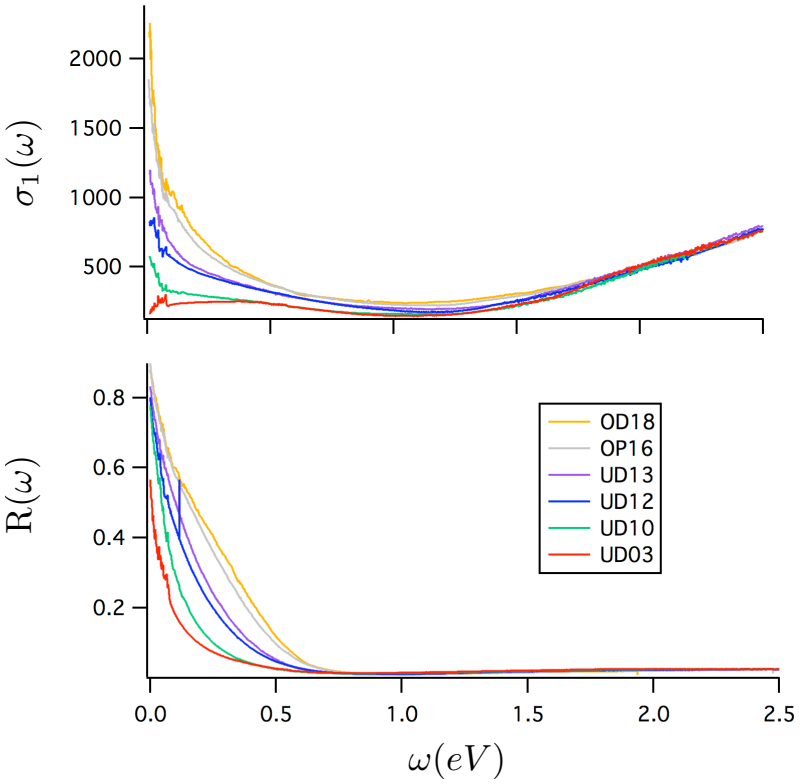

Figure 6.6: Optical conductivity $\sigma_1(\omega)$ and reflectivity $R(\omega)$of $Bi_2Sr_{2-x}La_xCuO_{6+\delta}$ under various doping $0.03 < p < 0.18$

frequency regime ($\lesssim 0.2$ eV) the conductivity increases strongly with the doping. This is in agreement with the qualitative picture of a larger concentration of free carriers that drives the system to a more metallic behaviour. In fact, with the exception of the UD03 sample (red line), the conductivities show a metallic Drude response. As shown in [Lupi et al., 2009] where they compare these samples with an even more underdoped sample of $Y_{1-x}Ca_xBa_2Cu_3Cu_3O_6$, from the high doping to the low (or absent) doping regime the metal-insulator

transition occurs. If we focus around 0.4 eV another feature can be observed. Especially in the underdoped samples it is possible to see the presence of a mid-IR peak also observed in [Lee et al., 2005]. This kind of resonance is predicted by a detailed analysis of the electronic structure of doped Mott-insulators (see Section 3.4 on the optical properties of cuprates) and can be associated to the transition that occurs between the lower Hubbard band to the conduction band of the oxygen $2p$ (as shown in Figure 6.7). Upon doping, spectral weight appears inside the charge-transfer gap of the undoped compounds, defining this mid-IR band [Dagotto, 1994].

The third main feature of these optical conductivity curves is a series of interband transitions starting around 2 eV. At this energy there is a broad features which has been associated with the onset of charge transfer (CT) excitations between Cu-$3d$ and O-$2p$ orbitals [Uchida et al., 1991].

The experimental data are fitted using the Drude-Lorentz model presented in Section 3.1, eventually adding a glue function to account for the coupling with bosonic fluctuations at low frequencies. Figure 6.8 reports the real ($\sigma_1(\omega)$) and imaginary ($\sigma_2(\omega)$) parts of the UD10 sample optical conductivity. In the graph inset, the reflectivity $R(\omega)$ is presented. From these data we can clearly see that, below 0.2 eV, the optical properties are dominated by the Drude response of free carriers, whereas in the high- energy region (> 2 eV), a major role is played by the interband transitions. The best fit to the data, performed simultaneously on $\sigma_1(\omega)$ and $\sigma_2(\omega)$ is reported on the same graph as thin solid black lines. This fit has been obtained modelling the optical conductivity as:

$$\sigma(\omega) = \sigma_D(\omega) + \sum_{i=1}^{m} \sigma_{L_i}(\omega) \tag{6.1}$$

where $\sigma_D(\omega)$ and $\sigma_{L_i}(\omega)$ represent the Drude and the Lorentz oscillators, the latter being indexed by i. Figure 6.9 reports the different contributions of the single oscillators to the real part of the optical conductivity $\sigma_1(\omega)$. Three regions are evident: 1) the Intraband one, governed by the Drude contribution; 2) a region up to 0.4 eV characterized by the presence of the mid-IR peak already discussed, and related to the transitions between the LHB to the conduction band of the O_2p; 3) an intense feature (represented by transitions i=1,2,3,4,5) which represents the reminiscence of the charge-transfer (CT) gap, starting around 2 eV and the excitations at higher energies involving the O-$2p$ orbitals. In details, the parameters used to fit the experimental data are reported in Table 6.3.2. At this point it is useful to go deeper in details dividing the spectra of the optical properties of the samples in the low-energy regime (below 2 eV) and

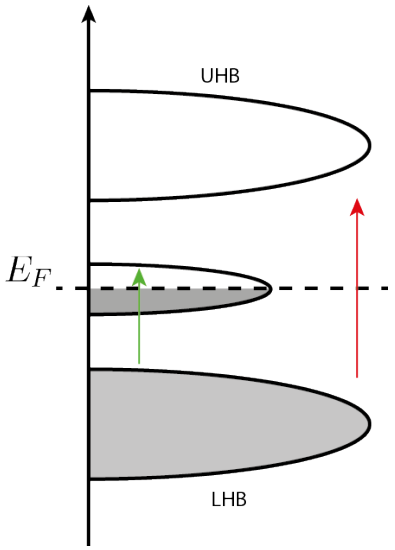

Figure 6.7: Schematic global density of states of hole-doped Mott insulators. The band around the Fermi level, the upper Hubbard band (UHB), and the lower Hubbard band (LHB) are schematically illustrated. The red arrow represents the charge-transfer excitation, the green arrow identifies the excitations in the mid-IR region.

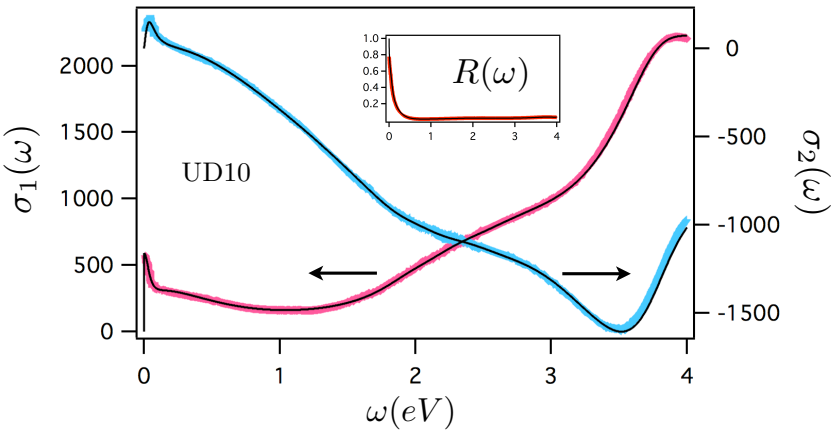

Figure 6.8: Real $\sigma_1(\omega)$ and imaginary $\sigma_2(\omega)$ part of the optical conductivity of UD10 sample. $\sigma_1(\omega)$ is the pink line, $\sigma_2(\omega)$ is the light blue one. The solid thin black lines are the best fit. In the inset the reflectivity $R(\omega)$ is also reported.

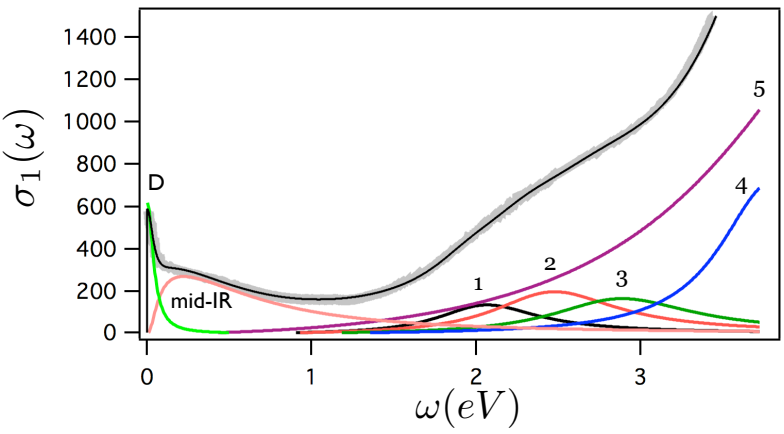

Figure 6.9: Optical conductivity $\sigma_1(\omega)$ of UD10 sample (grey line) together with the best fit (black line) obtained adding together the different contributions of Drude term (light green line) mid-IR peak (pink line) and five oscillator starting at 2.0 eV. The detailed parameters of the oscillators are reported in Table 6.3.2.

Parameter	Value	Unit
ϵ_∞	1.05	
ω_{p0}	1789	cm^{-1}
γ_{imp}	203	cm^{-1}
$\omega_{0_{mid-IR}}$	1959	cm^{-1}
$\omega_{p_{mid-IR}}$	4544	cm^{-1}
γ_{mid-IR}	6142	cm^{-1}
ω_{0_1}	17130	cm^{-1}
ω_{p_1}	3199	cm^{-1}
γ_1	6002	cm^{-1}
ω_{0_2}	19946	cm^{-1}
ω_{p_2}	4276	cm^{-1}
γ_2	7351	cm^{-1}
ω_{0_3}	23255	cm^{-1}
ω_{p_3}	4167	cm^{-1}
γ_3	8337	cm^{-1}
ω_{0_4}	30616	cm^{-1}
ω_{p_4}	7523	cm^{-1}
γ_4	6289	cm^{-1}
ω_{0_5}	38014	cm^{-1}
ω_{p_5}	22167	cm^{-1}
γ_5	21596	cm^{-1}

Table 6.2: Position (ω_0), plasma frequency (ω_p) and width (γ) expressed in cm^{-1} of the Drude, mid-IR and interband transitions contributions at the best fit for UD10 optical conductivity. (For clarity: 8064 cm^{-1}=1 eV)

high-energy regime (above 2 eV).

6.3.1 *Low-energy Optical Properties: Drude peak and mid-IR peak*

The previous analysis on the best fit to reproduce the equilibrium optical properties with different contributions is related to the underdoped sample UD10. If we move towards higher doping concentrations and we want to analyse the optical properties at equilibrium of the OD18 (that is the most over-doped sample available) we need to introduce the glue function in order to correctly fit the data. The glue function, as explained in Section 3.2, represents a coupling of the free carriers with a bath of bosons that extends up to 0.4 eV. Figure 6.10 shows the best fit of the OD18 sample with its related glue function $\Pi(\omega)$ in the inset. The black line is the Drude term, the blue line is the mid-IR peak and the red line refers to the interband transition of the CT excitation (which will be tackled in the next section). As a comparison, a zoom of the best fit for the UD10 sample with the different contributions is also reported. In the first panel the OD18 optical conductivity data are fitted by a simple Drude term (black line) plus a T-independent mid-IR band peaked at 0.4 eV (blue line) and the onset of the charge-transfer excitations described by

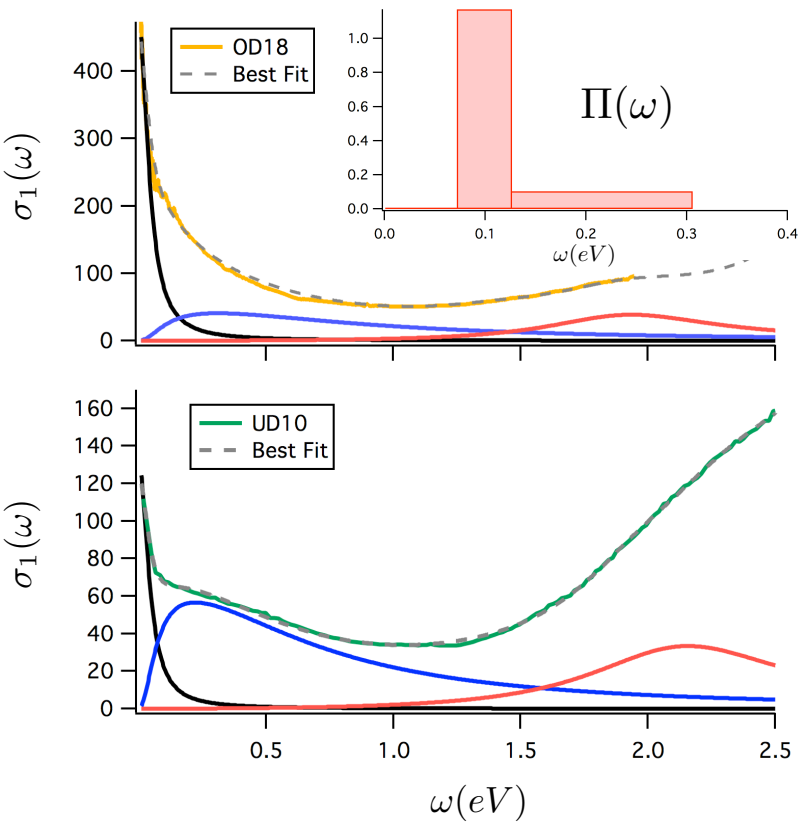

Figure 6.10: a) Best fit (dashed grey line) of the optical conductivity $\sigma_1(\omega)$ of the OD18 sample (yellow line) with the three main contributions: Drude (black line), mid-IR (blue) and the first CT oscillator (red). In the inset the glue function $\Pi(\omega)$ obtained by the best fit. b) Best fit (dashed grey line) of the optical conductivity $\sigma_1(\omega)$ of the UD10 sample (green line). The best fit is obtained without any glue function.

a Lorentz oscillator centred around 2 eV (red line). In addition, a T-dependent glue function $\Pi(\omega)$ has been added at low frequencies up to ∼0.3 eV. This spectrum, represents the electron-boson coupling strength at boson frequency ω multiplied by the boson density of states at the same boson frequency. An histogram-like form for the glue function has been assumed. The spectrum is characterized (even though very weak) by a low-energy part (up to 80 meV), compatible with the coupling to acoustic phonons [Johnston, 2011] and Raman-active optical phonons, involving c-axis motion of the Copper ions [Kovaleva et al., 2004]; a narrow, intense peak centered at 100 meV, attributed to the anisotropic coupling to either out-of-plane buckling and in-plane breathing Cu-O optical modes [Devereaux et al., 2004] or bosonic excitations of electronic origin, such as spin fluctuations [Dahm et al., 2009], and, finally, a broad continuum, extending up to 310 meV ([Norman and Chubukov, 2006], [Hwang et al., 2007], [van Heumen, 2009]). Note that the mid-IR peak intensity decreases increasing the doping. The evolution of the $\omega_{p_{mid-IR}}$ with the doping is reported in Figure 6.11.

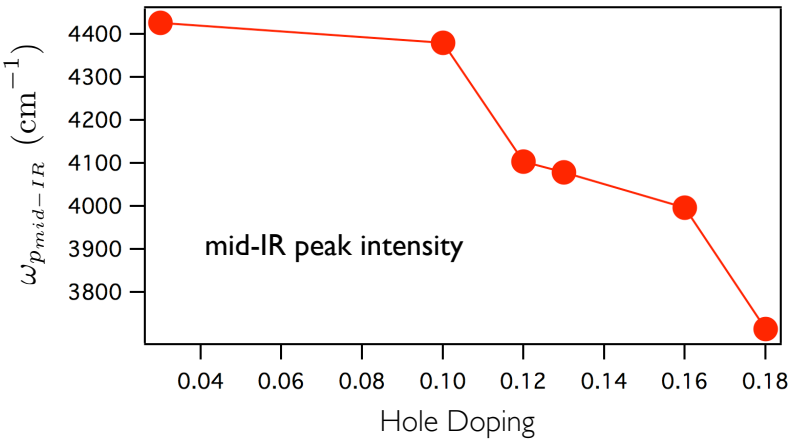

Figure 6.11: Intensity, expressed in cm^{-1} of the mid-IR peak $\omega_{p_{mid-IR}}$ as a function of the doping. Moving towards the overdoped regime, the mid-IR peak decreases.

In Figure 6.12 a comprehensive panel with the optical conductivity at low frequencies for every doping and at different temperatures has been presented. The temperature affects mainly the part of the spectrum at very low frequencies, i.e. $\hbar\omega$ <0.2 eV. As already shown before, the mid-IR band is T-independent. From the overdoped regime, decreasing doping, the Drude peak decreases until it disappears in the very underdoped sample. Figure 6.13 shows the real part of the optical conductivity $\sigma_1(\omega)$ for two different temperatures on the OD18 sample together with the best fit at both temperatures. Cooling down the sample from 300K to 100K, the data are fitted changing the temperature in formula 3.11 that describes the coupling with

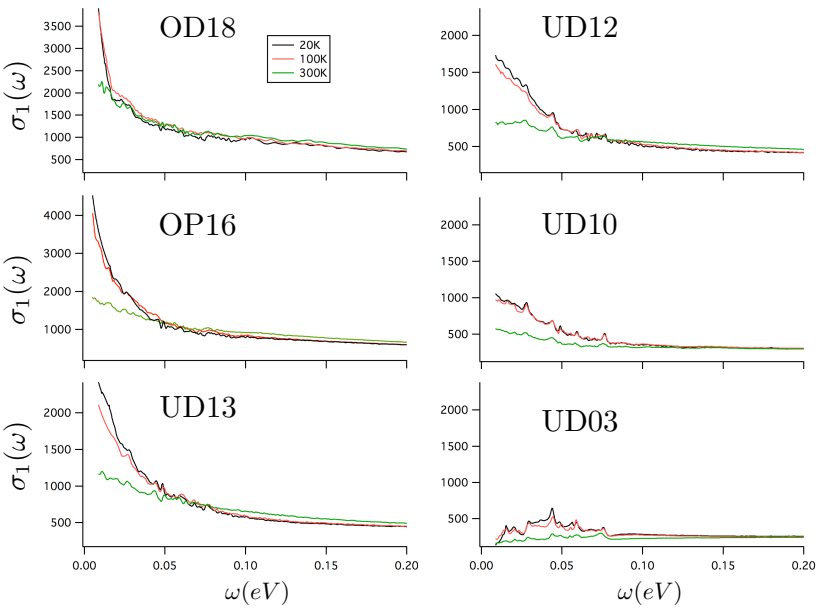

Figure 6.12: Comprehensive panel of the optical conductivities $\sigma_1(\omega)$ of the six samples studied in this work. The three lines in each graph represents the evolution of the optical conductivity in temperature: black line (T=20 K), red line (T=100 K), green line (T=300 K).

the bath of bosons but also slightly changing the shape of the glue function $\Pi(\omega)$ in the inset. The narrow peak centered at 0.1 eV has been narrowed and shortened. So, assuming a certain coupling with the bosons and changing the population of these bosons with temperature together with a different coupling with the bosonic excitations it is possible to follow the behaviour of the real data. Regarding the UD10 sample temperature behaviour (shown in Figure 6.14) the absence of the glue function and the coupling with bosons already at 300K can be phenomenologically modelled by assuming a temperature dependence of the optical properties to the scattering rate of the free particles in formula 3.11. Changing the parameter γ_{imp} it is possible to well reproduce the data.

6.3.2 *High-energy Optical Properties: Charge-Transfer excitation*

The main results of the present work refers to the charge-transfer excitations at high energy $\hbar\omega \sim 1.8 - 2.4$ eV. In a charge-transfer insulator, the charge-transfer excitation is the energy needed to move an electron from the O-2p band to the Cu-3d band. It is defined as the lowest excitation that can occur in these insulators, giving origin to a charge-transfer gap Δ_{pd}[1] that is of the order of 2 eV. If we consider the initial state $d_i^n p_i^m$ on the i-th unit cell (where n and m are the number of electrons on the Cu-3d and O-2p orbitals respectively), the charge transfer excitation is responsible to drive the system in $d_i^{n+1} p_i^{m-1}$ where an extra charge (hole) is present on the Copper (Oxi-

[1] p and d refer to the initial and final orbitals between which the charge-transfer occurs.

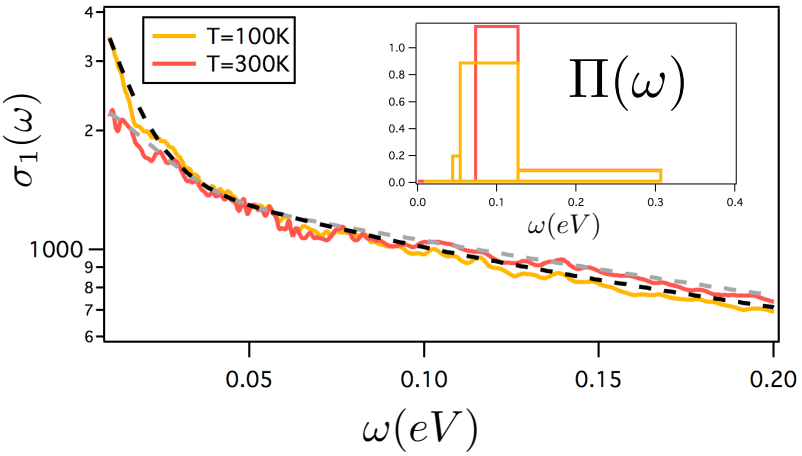

Figure 6.13: Best fit for the optical conductivity $\sigma_1(\omega)$ for the OD18 sample at two temperatures T=100 K (yellow line) and T=300 K (red line). In the inset the variation of the glue function with the temperature is also shown.

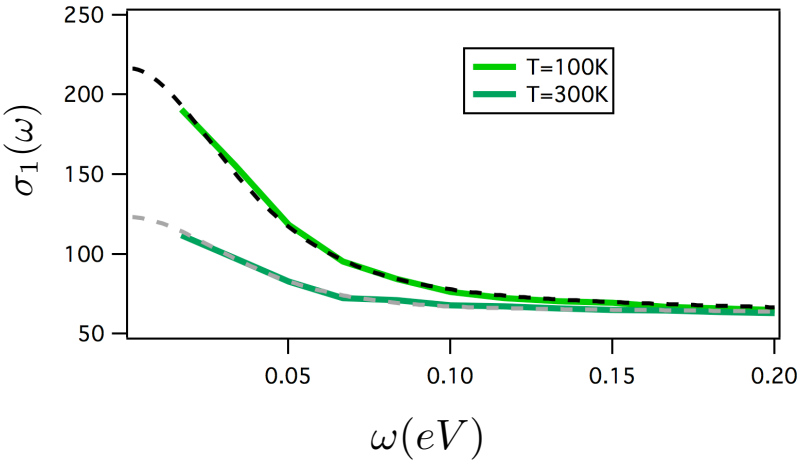

Figure 6.14: Best fit for the optical conductivity $\sigma_1(\omega)$ for the UD10 sample at two temperatures T=100 K (light green line) and T=300 K (dark green line).

gen) orbitals. Even though the $Bi_2Sr_{2-x}La_xCuO_{6+\delta}$ cannot become a charge-transfer insulator (differently from the $Y_{1-x}Ca_xBa_2Cu_3Cu_3O_6$), we can take the most underdoped UD03 sample (where the excitations at low energies are almost completely suppressed) as the closest reference to that situation. With this in mind, fitting the reflectivity data for all the six samples with the Drude-Lorentz model it is possible to extract the various oscillators that contributes to the absorption at high energy. In Figure 6.15 the reflectivity curves for six different doping concentrations, together with the best fit at high energies, are reported (note that the y-axis is in logarithmic scale to highlight the differences in the frequency range of 0.5-2.5 eV).

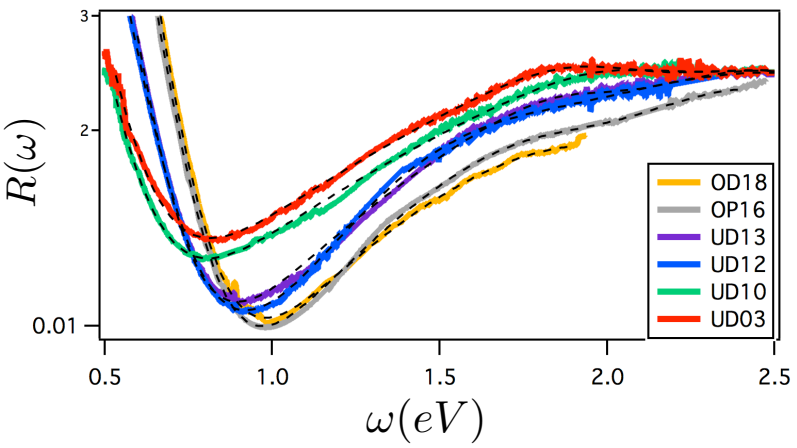

Figure 6.15: Reflectivity data $R(\omega)$ at different dopings. The best fit (dashed black lines) is obtained using the Drude-Lorentz model.

Besides the Drude peak and the mid-IR peak that fit the curves at low energies (already discussed in the present chapter), in Figure 6.16 we report the first two oscillators needed to fit the data at higher energies only for the UD03 and OP16 samples. We can see that the first oscillator centered around 2 eV is present for all the doping, from the underdoped to the overdoped. For our purposes the important parameters of these oscillators are their center position and their width. In Table 6.3.2 the parameters of the oscillator, extracted by the best fit, are reported. First of all it is important to note that the first oscillators, even tough with different spectral weight, it is present for all the doping. This means that the excitation at 2 eV lays under the optical properties at equilibrium for both the over and underdoped regime. The error bar of 0.1 eV on the position of the oscillators has been evaluated comparing the chiSq that doesn't change sensibly with different configurations of the other parameters. From the best fit comes out that the position of the first oscillator is always the same centered at 2 eV in all the sample and so, it is independent from the doping.

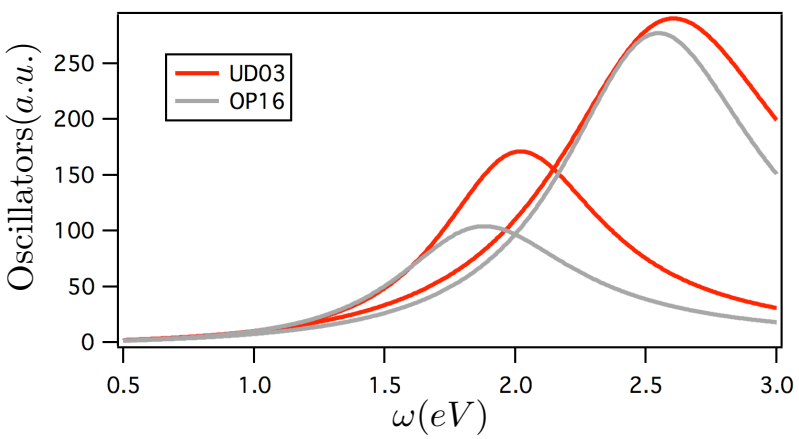

Figure 6.16: First two oscillators describing the charge-transfer excitations in UD03 and OP16 samples.

Sample	Osc1 Position (eV)	Osc1 Width (cm^{-1})	Osc2 Position (eV)	Osc2 Width (cm^{-1})
OD18	2.00±0.1	6913	2.41±0.1	7942
OP16	1.88±0.1	6714	2.54±0.1	7365
UD13	1.94±0.1	5498	2.58±0.1	8620
UD12	2.10±0.1	6006	2.54±0.1	7532
UD10	1.92±0.1	5870	2.59±0.1	8679
UD03	2.02±0.1	6185	2.60±0.1	8787

Table 6.2: Position and width of the first two oscillators used to fit the reflectivity of the samples for all the doping. In Figure 6.16 only the oscillators for the UD03 and OP16 samples are reported.

For the analysis presented in the next section, it is important to make sure that the oscillator centered around 2 eV is really related to the charge-transfer excitation from the O-2p band to the Cu-3d band. This can be proved saying that, taking the UD03 sample as a reference (because the closest to the charge-transfer insulator), excluding the Drude part of the spectrum and the mid-IR peak that are associated to different physical processes, the oscillator at 2 eV is the lowest-energy electronic excitation. This is true not only for the most underdoped sample but also for the others. So we can conclude that the oscillator centered at 2 eV, required to fit the optical properties at equilibrium, is the charge-transfer oscillator O-2p $\rightarrow$ Cu-3d and it is true for all the doping concentrations. Our result is well confirmed by literature [Falck et al., 1992] where an analysis on the charge-transfer insulator La_2CuO_4 shows that the charge-transfer excitation at 300 K is described by an oscillator centered at 2.08 eV with a width of 5680 cm^{-1} (see Figure 3.6). This is in agreement with our results.

6.4 Optical Properties Out Of Equilibrium

Once the equilibrium optical properties of the material under investigation are completely understood it is possible to look at a differential model. In other words, the equilibrium, experimentally measured (usually by ellipsometric techniques) complex optical conductivity $\sigma(\omega, T) = \sigma_1(\omega, T) + \sigma_2(\omega, T)$ must be satisfactorily reproduced by fitting to it a model composed of a Drude oscillator (in the Extended Drude formalism) and a sum of Lorentz oscillators, representing respectively the mid-IR transitions (low-energy part) and the interband transitions (high-energy part). This model will constitute the static, equilibrium optical conductivity $\sigma_{eq}(\omega, T)$, the starting point of our differential analysis. Usually this model is constituted by a huge number of parameters (30-40). The final quantity we measure with the time-resolved spectroscopic setup is the transient reflectivity $\Delta R/R(\omega, t)$, which includes the frequency information ω and where t is the pump-probe delay. This quantity is defined as follows:

$$\Delta R/R(\omega, t) = \frac{R_{excited}(\omega, t) - R_{eq}(\omega)}{R_{eq}(\omega)} \tag{6.2}$$

where $R_{eq}(\omega)$ is the equilibrium reflectivity (which does not depend upon t, since it is measured without the pump beam), related to $\sigma_{eq}(\omega)$ through formula 3.1, and $R_{excited}(\omega, t)$ is the transient reflectivity measured after the pump excitation(which now depends upon the pump-probe delay t). $R_{excited}(\omega, t)$ will be related to a new, non-equilibrium optical conductivity, which we call pumped optical

conductivity, indicated with $\sigma_{excited}(\omega, t)$. This optical conductivity will describe the effect of the pump excitation on the material electronic structure. In principle, this optical conductivity will be as similar as possible to the static one: our approach is to vary the smallest subset of parameters necessary to catch the transient reflectivity spectrum at delay t, with most of the parameters being unvaried. The number of oscillators is never modified. Only slight perturbations of the parameters are considered throughout this work (as we work in a linear regime of fluences).

In the next two sections we are going to show what happens to the reflectivity of the samples, due to the external excitations, in one of the simplest case: the excitation process is entirely converted, on a time scale of few femtoseconds, in a local heating of the electronic temperature. From this moment, when we speak about "heating" we refer to the impulsive heating of the electrons that leads to an effective electronic temperature T_{eff}. This is not to be confused with an average heating of the entire lattice to the thermodynamic equilibrium. This kind of average heating, working with a laser setup based on a repetition rate of 1KHz can be excluded.

The pump excitation effect on the equilibrium optical conductivity, resulting in a non-equilibrium optical conductivity, can be of different nature. After the excitation, teh energy deposited by the pump, impulsively heats the electrons. Such electrons then can exchange energy on a fast time scale (<100 fs) with bosonic excitations of electronic origin. After that, on a longer time scale (>100 fs) the energy is dissipated through the strongly coupled phonons and then, on the ps time scale the energy is shared with the whole lattice. This is a mainly thermal effect, which means the transient spectrum can be reproduced by varying only the temperatures of the Extended Drude formalism (in other words, changing the temperature of the bath of bosons) (see Section 3.2), or can be of different kind (though a small heating of the system is obviously always present, which is given by the energy deposited in the system by the pump pulse). If we consider other effects related to the low-energy part of the dielectric function, the pump pulse can for example modify the shape of the glue function in the Extended Drude model. While if we consider the high-energy part of the dielectric function, a pump-induced modification of the Lorentz oscillator parameters can take place. A plasma frequency modification for some oscillators indicates a spectral weight shift, while a modification in the central frequencies or widths of some oscillators, may suggest a modification of the band structure.

6.4.1 *Low-energy Regime*

Figure 6.18 and Figure 6.19 report the transient reflectivity

$$\frac{\Delta R}{R}(\omega; T_{eff}, T_0) = \frac{R(\omega, T_{eff}) - R(\omega, T_0)}{R(\omega, T_0)}. \tag{6.3}$$

assuming that the effect of the pump is to change the bosons population through the T_{eff} (Figure 6.18 on the OD18 sample), or to increase the dumping term $\gamma_{imp}$with a consequent reduction of the conventional scattering time $\tau = \gamma^1_{imp}$ (Figure 6.19 on the UD10 sample). In the first case, changing the effective temperature means to change the boson population maintaining informations on its spectrum. In the second case, changing γ_{imp} one loose the structure of the boson spectrum at low-frequencies but at higher frequencies the result is the same then in the first case.

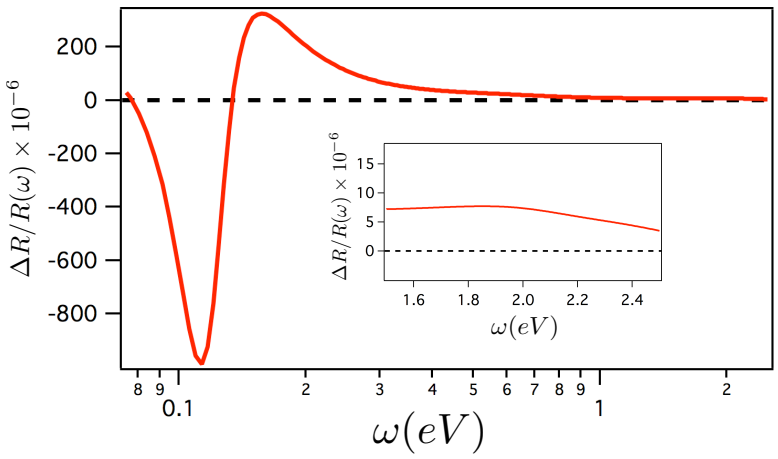

Figure 6.18: Simulated reflectivity variation $\Delta R/R(\omega)$ increasing the temperature of the OD18 sample from 100 to 300 K. In the inset a zoom to our region of interest between 1.5 eV to 2.5 eV

In both the case the variation of the reflectivity follows a similar behaviour. It is negative below a certain frequency (0.13 eV for the OD18 and 0.14 eV for the UD10) but then turns to be positive above that frequency. In this work we are interested in a frequency window within 1.8 and 2.4 eV so, in the inset of the two figures we have reported a zoom of that frequency range so that it is easy to see that the reflectivity variation is positive for both the sample in that frequency range.

6.4.2 *High-energy Regime*

For what concerns the effect of an external excitations on the high-energy regime, we concentrate on the frequency range 1.8-2.4 eV. This is exactly the energy range probed by the measurements that are

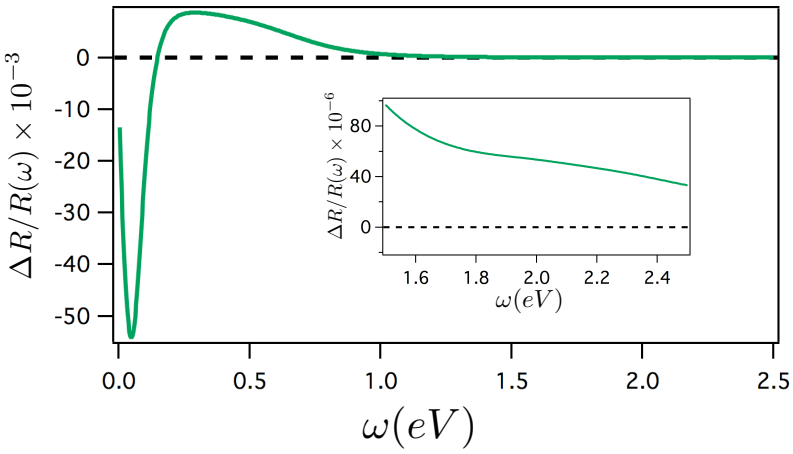

Figure 6.19: Simulated reflectivity variation $\Delta R/R(\omega)$ increasing the temperature of the UD10 sample from 100 to 300 K increasing the scattering rate γ_{imp}. In the inset a zoom to our region of interest between 1.5 eV to 2.5 eV

the clue point of the present work. We have already seen, with the analysis of the optical properties at equilibrium in Section 6.3.2, that this frequency range is characterized by the presence of the charge-transfer oscillator centered around 2.0 eV. The effect of the pump on an oscillator can be to modify its parameters: position, height and width. At this point we can show how the reflectivity could change if the effect of the pump is to move the central position of an oscillator (we will see that the real data are well reproduced changing just this parameter). We start, for example, from the best fit of the UD13 sample. The fit of its reflectivity at equilibrium is characterized by the presence of an oscillator centered at 2.10 eV. If we assume that the effect of the pump on the reflectivity is to change the position of such oscillator, what we obtain is presented in Figure 6.20. If the

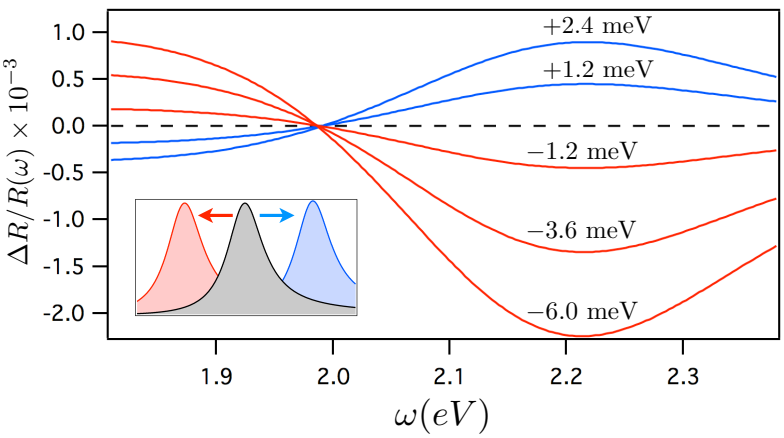

Figure 6.20: Transient reflectivity $\Delta R/R(\omega)$ due to a redshift (red) and blueshift (blue) of the oscillator at 2.1 eV in the reflectivity of UD13 sample.

oscillator moves towards higher energies (the blueshift described by

blue lines) the effect is to increase the reflectivity above 2.0 eV and reduce it below this photon energy. On the contrary, if the oscillator moves towards lower frequencies, the effect is the opposite: a positive variation below 2.0 eV and negative above.

6.5 Time- and Frequency-resolved Data

6.5.1 Time-Resolved measurements with OPA-based System

In this section we present the time and frequency resolved pump probe reflectivity measurements performed at T=300K on $Bi_2Sr_{2-x}La_xCuO_{6+\delta}$. The probed energy range is $1.8 - 2.4$eV while the pump is set at 1.37 eV with 2.0 mJ/cm^2 of fluence[2] and a pulse length of 6 fs (for the details of the experimental setup see Section 5.2. Figure 6.21 presents the complete set of measurements performed on six different samples with different doping levels. The six panels of Figure 6.21 show the transient reflectivity ($\Delta R/R(\omega, t)$) after the perturbation due to the pump laser pulse. The measurements have been performed under the same condition of temperature and pump fluence. We start discussing panel a) of Figure 6.21 which represents $\Delta R/R(\omega, t)$ measured on the overdoped OD18 sample. We can see that the reflectivity variation is positive and does not present any defined feature throughout the whole frequency range investigated. This may suggest that, as we have seen in the differential analysis of Section 6.4.1, the $\Delta R/R(\omega, t)$ signal can be attributed to a thermal effect, described by a variation of the effective temperature of the bath of bosons. In the inset we report the dynamics of this positive variation. This trace is obtained by a Singular Value Decomposition analysis. The temporal dynamics of the variation is actually described by two different decay rates: one fast of the order of few tens of femtoseconds and one slower of the order of one hundred femtoseconds . The detailed analysis on the time domain of these traces will be presented later in Section 6.6. Following the evolution of the data with the doping concentrations (panels b)-f)), we note that: 1) the positive variation persists at lower frequencies and maintains its dynamics; 2) in the frequency range between 2.0 and 2.4 eV a negative signal appears and becomes wider in frequencies as the doping decreases. This negative variation is also visible in the dynamics (insets) and also presents two different decay constants (discussed later in 6.6). This can be clearly seen in Figure 6.22 where the time trace $\Delta R/R(\omega, t = 100fs)$ is reported. For the UD samples the reflectivity variation curve, after 100 fs, lays below the zero line for a large part of the spectrum, in contrast to the results on OP and OD regime, where the reflectivity variation (at $t = 100$ fs) lays always

[2] Calculated from an energy per pulse of 40 nJ and a beam diameter of 100μJ

above the zero line.

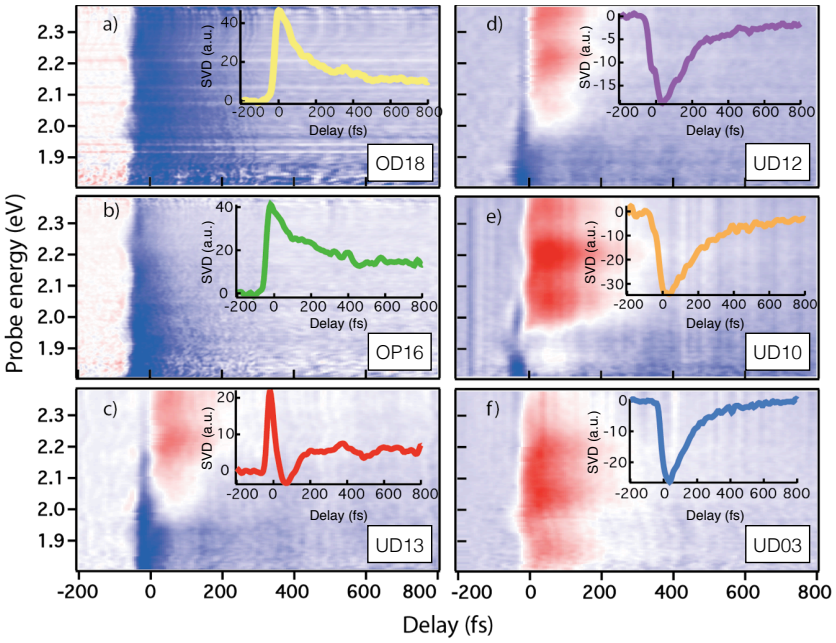

Figure 6.21: $\Delta R/R(\omega, t)$ performed on six different doping levels of Bi2201: a) OD18, b) OP16, c) UD13, d) UD12, e) UD10, f) UD03. The blue color means positive variation, the red color means negative variation. In the insets a dynamics trace obtained by the SVD analysis is shown.

In the insets of Figure 6.21, for each panel, the time trace obtained by a Singular Value Decomposition (SVD) analysis of the matrices is shown. The SVD analysis consists in decomposing $\Delta R/R(\omega, t) = \sum_k \Psi_k(\omega)\delta\phi_k(t)$. The SVD analysis confirms that 97% of the signal is reproduced by the first eigenvalue ($k = 1$), i.e.,$\Delta R/R(\omega, t) \simeq \Psi_1(\omega)\delta\phi_1(t)$ where $\Psi_1(\omega)$ is the eigenvector in the frequency domain that relaxes with the dynamics $\delta\phi_1(t)$. $\delta\phi_1(t)$ curve extracted from SVD retains the same information of the experimental time-traces, while providing the global dynamics of the whole spectrum. The sign and amplitude of the time trace at any frequency ω can be reconstructed by multiplying $\delta\phi_1(t)$ by $\Psi_1(\omega)$. This is very useful to extract a temporal dynamics that, even though may change in intensity and sign, remains the same (in terms of decay time) along the whole spectrum. Therefore the time traces in the inset are not just a slice of the matrix at a certain frequency but can be considered as the global dynamics of the whole spectrum. From the traces in the insets we can see that in panels a) and b) the $\delta\phi_1(t)$ is positive and described by two decay times. In panel c) $\delta\phi_1(t)$ presents two dynamics with opposite signs, one positive and one negative. For the other three samples (UD12, UD10, UD03) $\delta\phi_1(t)$ is completely negative. So, the negative variation visible in the data matrices for the under doped samples, is visible also in the time SVD traces.

Note a clear oscillation in the time domain trace of the UD13

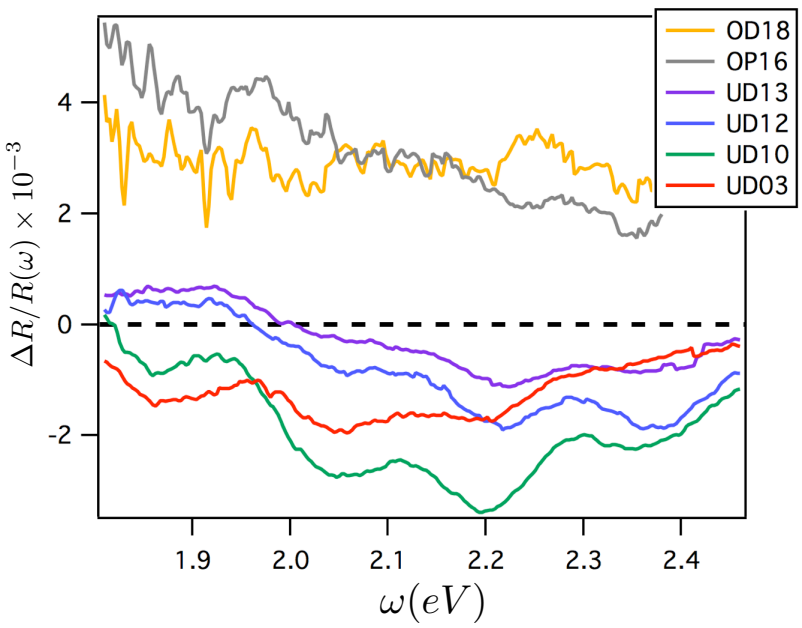

Figure 6.22: Reflectivity variation for the six samples at $\tau = 100$ fs.

sample. The period of this oscillation is 187 fs and corresponds to a coherent phonon mode of frequency 178 cm−1. In literature this mode is associated to the phonon Raman disordered-induced mode of the Bi/Sr in a an ideal tetragonal structure $I4/mmm$ [Kovaleva et al., 2004] [Kakihana et al., 1996]. A different kind of oscillation is also present in the frequency domain of the measurements in Figure 6.21. This oscillation is due to an experimental artefact related to.... To demonstrate this we compare these data to the results obtained with a different setup that uses directly the output of a Ti:Sapphire oscillator as explained in details in Section 5.1. These data are reported in Figure 6.23 and here the oscillation in questions are absent.

6.5.2 *Time-Resolved measurements with Ti:Sapphire Oscillator*

In order to investigate a different regime of excitations, characterized by lower fluences, and different photon energy of the pump pulse, we performed comparative measurements using a different experimental setup. The measurements on UD10 are reported in Figure 6.23. The measurements have been performed by using the supercontinuum light produced by a photonic fiber seeded by the output of a Ti:Sapphire oscillator. The temporal resolution of the system is given by the cross correlation between pump and probe pulse and it is of 120 fs. The repetition rate is set at 543 KHz and the

used pump fluence ranges from $120\mu J/cm^2$ to $590\mu J/cm^2$. The three panels of Figure 6.23 report the transient reflectivity of the UD10 sample with an energy range within 1.1-2.4 eV and a time window of 4 ps after the pump excitation. The panels a), b) and c) shows the transient reflectivity for pump fluences of $590\mu J/cm^2$, $240\mu J/cm^2$, $120\mu J/cm^2$ respectively. Comparing the measurements of Figure 6.23 with the panel e) of Figure 6.21 it is interesting to note that the discontinuity from a negative to a positive variation of the reflectivity occurs between 1.8 and 2.0 eV. Figure 6.24 shows the temporal

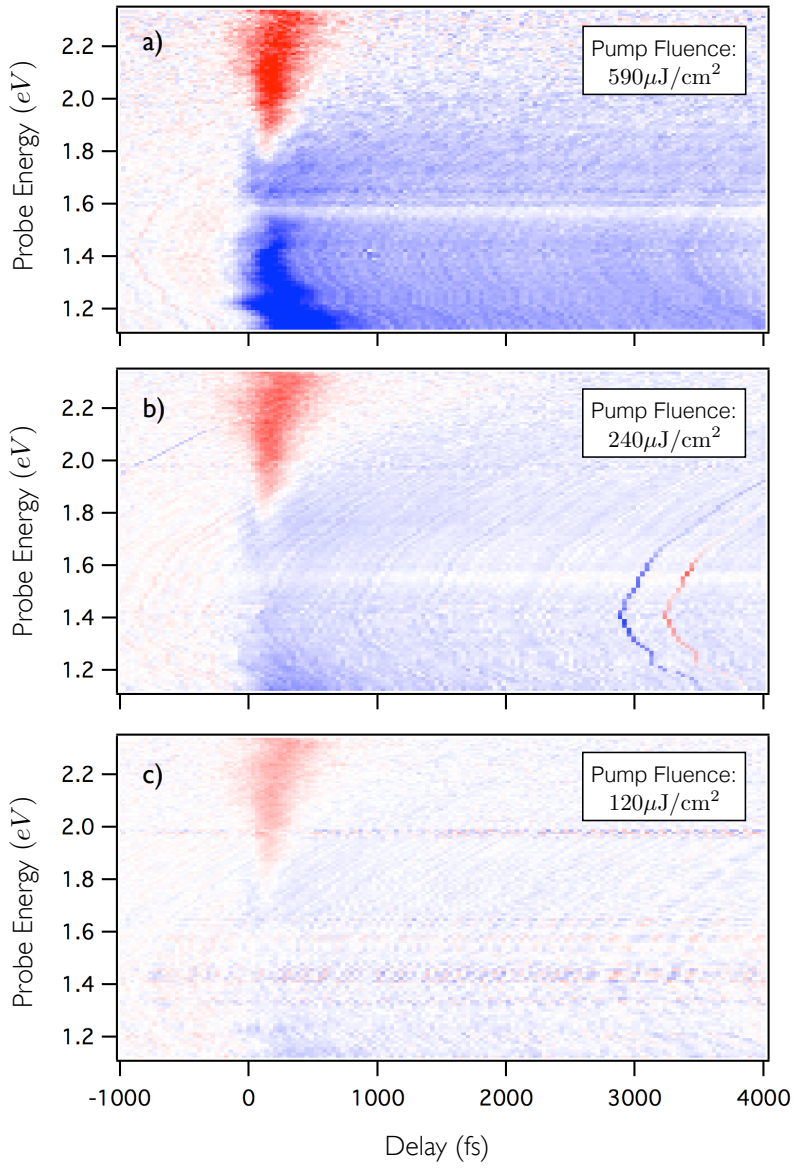

Figure 6.23: Transient reflectivity of the UD10 sample. The panels a), b) and c) shows the transient reflectivity for a pump fluence of $590\mu J/cm^2$, $240\mu J/cm^2$, $120\mu J/cm^2$ respectively.

traces obtained taking a slice of the 2D data at $\hbar\omega = 2.1$ eV. The inset displays the evolution of the intensity of the negative peak as a function of the fluence. We can see that this parameter is linear with the fluence, confirming that we are in a linear regime of excitation.

The dynamics in Figure 6.24 can be fitted by a single exponential

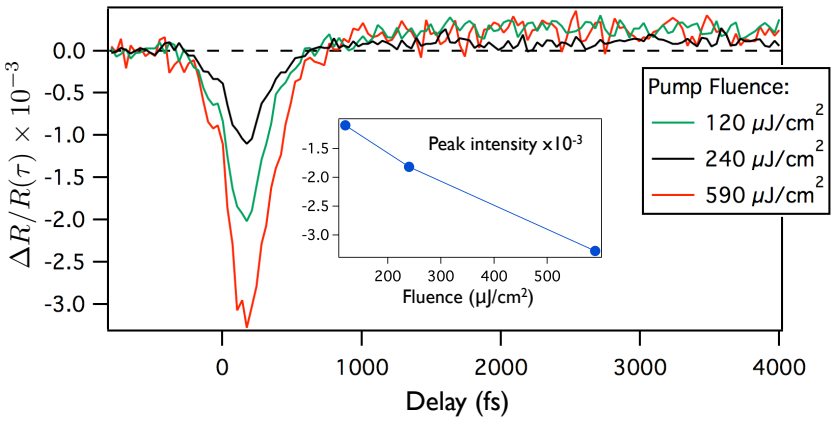

Figure 6.24: Transient reflectivity at $\hbar\omega = 2.1$ eV of the UD10 sample for a pump fluence of $590\mu J/cm^2$, $240\mu J/cm^2$, $120\mu J/cm^2$.

decay, independent of the fluence of $\tau = 130$ fs. The lack of the faster dynamics ($\tau_1 = 42$ fs) observed in the OPA-based measurements is related to the worse time resolution[3] of the oscillator-based system that is not able to resolve dynamics faster than its pulse length.

[3] The OPA system has a pulse length of 6 fs while the oscillator has a 120 fs pulse length.

Another important issue to be pointed out is the behaviour of the transient reflectivity at very long delays ($\simeq$ 3 ps). Frequency traces, extracted from the data matrices at 3 ps, are reported in Figure 6.25. We note that the variation of the reflectivity is positive along the whole spectrum. At this time the system can be considered as locally thermalized and the behaviour of its optical properties can be reproduced by assuming an increase of the effective temperature of the whole system. This demonstrates that the doping evolution at 2 eV energy scale is inaccessible to equilibrium spectroscopies which probe the thermodynamic ground state equivalent to the $\Delta R/R(\omega, t)$ data at times longer than the local thermalization.

6.6 *Data Analysis*

The main evidence that comes out from the experimental data of time resolved spectroscopy on $Bi_2Sr_{2-x}La_xCuO_{6+\delta}$ is the clear different behaviour of the transient reflectivity in samples with different doping. As clearly shown in Figure 6.22 in the UD samples there is a negative component of the transient reflectivity at $\hbar\omega = 2.0 - 2.5$ eV that is absent in the OP and OD sample. In order to give an explanation

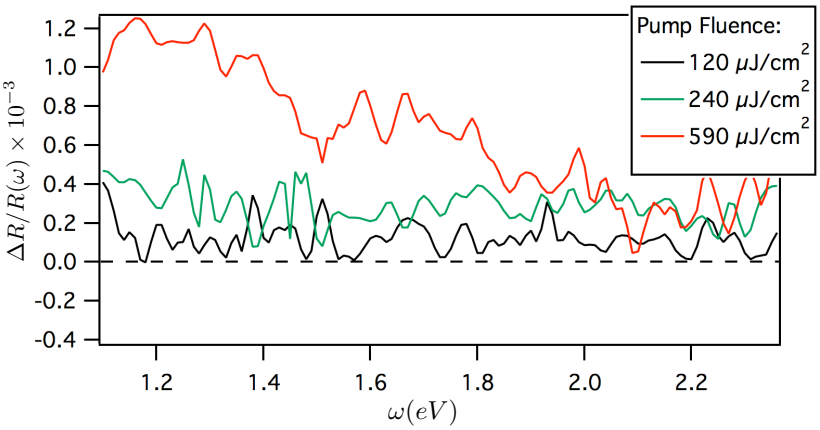

Figure 6.25: Transient reflectivity at $t = 3$ ps of the UD10 sample for a pump fluence of $590\mu J/cm^2$, $240\mu J/cm^2$, $120\mu J/cm^2$

of this behaviour we observe that the energy window that we are probing goes from 1.8 eV to 2.5 eV. This frequency range, according to the analysis on the optical properties at equilibrium (see Section 6.3.2), is centered on the charge-transfer excitation O-2p $\rightarrow$Cu-3d. In order to describe, in a quantitative way, the effect of the pump on the systems, we will assume the following two scenarios:1) quasi-thermal excitation, in which the transient spectrum can be reproduced by varying only the effective temperatures in the Extended Drude formalism or the scattering rate between quasiparticles and the boson bath (see Section 6.4); 2) pump-induced modification of the Lorentz oscillator parameters (position, intensity or width).

6.6.1 *Optimally- and Over-Doped Regime*

Let us focus first on the over and optimally doped samples. From the data fits comes out that the effect of the pump excitation is to induce a modification of the effective temperature in the Extended Drude formalism that describes the system at equilibrium. As already seen in Section 6.4.1, the modification of this parameter gives a positive transient reflectivity in the frequency range probed by our measurements. Figure 6.26 shows the transient reflectivity $\Delta R/R(\omega, t = 100\text{fs})$. The best fit is obtained just changing the temperature that is present in the extended Drude model from 300K to 3960K. At the microscopic level, we can say that the effect of the pump is to increase the effective temperature of the system changing the population of bosons with which the electrons can exchange energy. The resulting effect, within this scenario, is a positive variation of the reflectivity around 2 eV, as described in Figure 6.13.

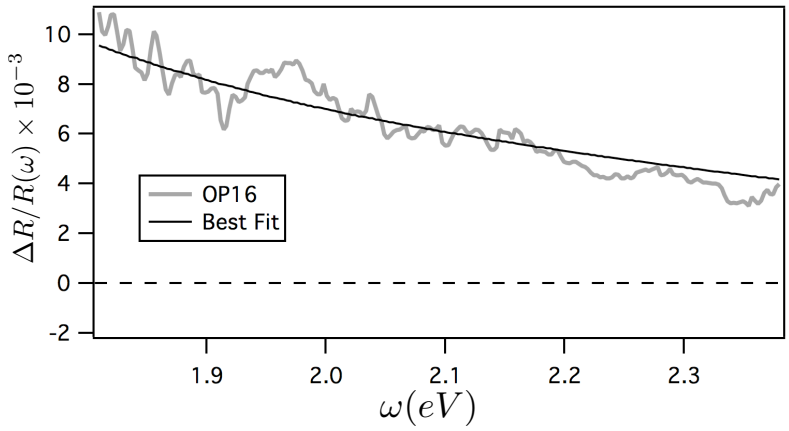

Figure 6.26: Transient reflectivity $\Delta R/R(\omega, t = 100\text{fs})$. The best fit is obtained just changing the effective temperature that is present in the extended Drude model.

6.6.2 *Under-Doped Regime*

Moving towards the low doping concentrations, the situation dramatically changes. The reflectivity variation of the four underdoped samples (UD13, UD12, UD10, UD03) is partially or completely negative around 2 eV. There is no way to reproduce this behaviour just by changing the effective temperature of the system or the scattering rate between electrons and bosonic excitations. The only way to reproduce this effect and to fit the data is to vary the parameters of the oscillators responsible of the charge-transfer excitations at 2 eV. We start, for example, from the best fit to the UD13 sample. The fit of its reflectivity at equilibrium is characterized by the presence of an oscillator centred at 2.10 eV. From the data analysis comes out that the effect of the pump on the reflectivity is to change the position of such oscillator. The fit that we obtain is displayed in Figure 6.27. In order to reproduce the experimental data, it is sufficient to redshift the oscillator of a value of 2.9meV from the equilibrium position of 2.1 eV. The amount of the redshift (2.9 meV) is linear with the fluence

The same analysis has been done on each underdoped sample (taking the fluence fixed at 2mJ/cm^2), and the best fit is shown in Figure 6.28 The central position of the oscillator obtained fitting the reflectivity at equilibrium and the amount of the redshift of such oscillator after the differential fitting is expressed in details in Table 6.3: The amount of the redshift $\Delta\omega_0$ at 2mJ/cm^2 (expressed in

Sample	Oscillator position at equilibrium (eV)	Redshift (meV)
UD13	2.10	2.9
UD12	2.19	5.2
UD10	2.12	8.4
UD03	2.01	2.9

Table 6.3: Oscillator position (in eV) and amount of the redshift (in meV) induced by a pump fluence of 2mJ/cm^2 for the four underdoped samples.

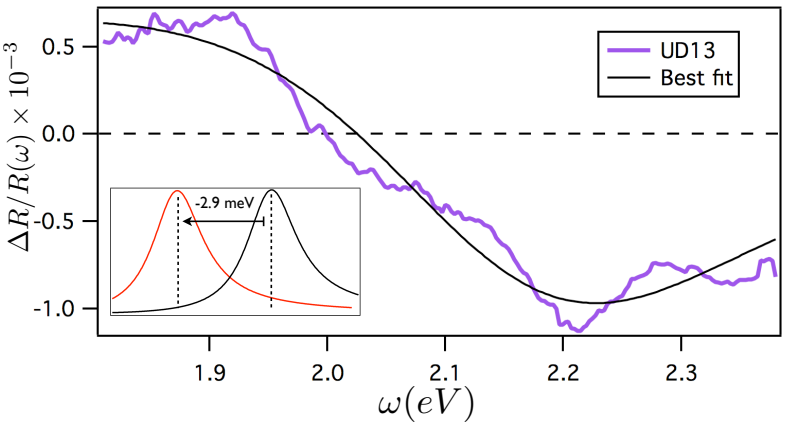

Figure 6.27: Transient reflectivity $\Delta R/R(\omega)$ induced by the pump excitation after 100 fs. The best fit is obtained moving the position of the oscillator at 2.10 eV (used to fit the reflectivity at equilibrium) by an amount of 2.9 meV towards lower energies.

meV) for each doping is displayed in Figure 6.29. For the overdoped ($p = 0.18$) and the optimally doped ($p = 0.16$) the redshift is zero.

In order to summarize these first results we can say:

- In the over and optimally doped regime, the variation of the reflectivity induced by the pump excitation can be reproduced by simply changing the effective temperature of the system. This means that the effect of the external excitation can be rationalized by assuming that energy delivered to the charge carriers is rapidly released (0-40 fs) to the boson bath (see [Conte, 2014]). This process results in a rapid increase of the effective temperature of the boson bath which successively relaxes by exchanging energy with the phonons [Conte, 2014] [Dal Conte et al., 2012]. The rapid energy exchange is compatible with the coupling to antiferromagnetic excitations. In these samples the external excitation doesn't affect the oscillator at 2 eV.

- In the uderdoped regime the situation is completely different. Even though the heating of the electronic temperature occurs, this is no longer enough to describe the negative reflectivity at 2.0-2.5 eV. To reproduce the experimental data we need to introduce a shift in the position of the oscillators that characterizes the reflectivity around 2 eV. More in details, we observe a redshift towards lower frequencies of about 3-9 meV at pump fluence of 2mJ/cm^2.

6.6.3 *DMFT Analysis*

In principle, the effect of the pump on the charge-transfer oscillator could be to modify each of its three parameters: position, width and intensity. Concerning this, Dynamical Mean Field Theory (DMFT)

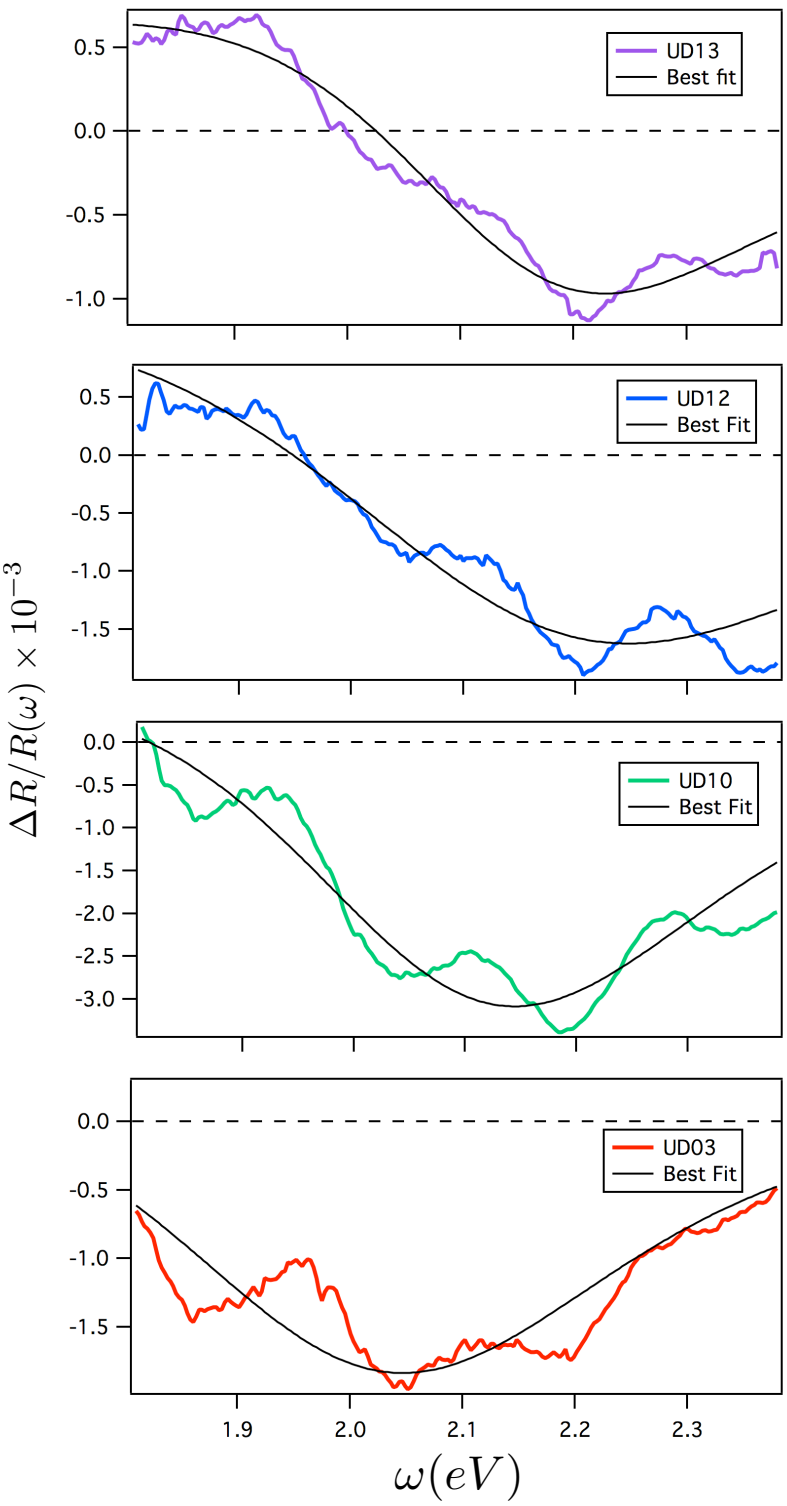

Figure 6.28: Transient reflectivity $\Delta R/R(\omega)$ induced by the pump excitation after 100 fs. The best fit is obtained moving the position of the oscillator around 2.0 eV for all the underdoped samples (UD13, UD12, UD10, UD03).

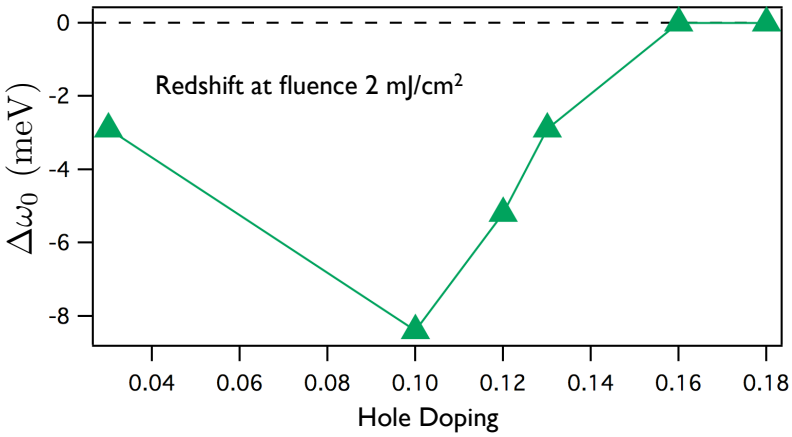

Figure 6.29: Redshift $\Delta\omega_0$ at 2mJ/cm^2 (expressed in meV) for each doping.

calculations performed by Massimo Capone at SISSA (Trieste) suggested, beside the redshift of the charge-transfer oscillator, also a reduction of its spectral weight. DMFT is based on a mapping of lattice models onto quantum impurity models. The very complex problem of a many body lattice is reduced looking at the dynamics of a single lattice site that interacts with a bath that contains the information of the lattice. The method can be used for the determination of phase diagrams (by comparing the stability of various types of long-range order), and the calculation of thermodynamic properties, one-particle Green's functions, and response functions [Georges et al., 1996]. Using this technique, the real part of the optical conductivity $\sigma_1(\omega)$ has been calculated and reported in the inset of Figure 6.30. The red line refers to the optimal doping sample, the blue line to the underdoped sample. We have integrated the spectral weight over the frequency range 2.4-5 eV (red and blue solid areas that refers to the energies of the interband transitions) and we have reported the results of this integration, for the two different dopings, at various temperature, in the main graph. We can see that the behaviour in temperature of the interband transitions spectral weight is opposite for the two levels of doping. In the optimally doped sample the spectral weight increases with temperature. For the under doped sample the spectral weight decreases. The behaviour of the optimally doped sample is well described by a picture where the effect of the temperature is just to broad the Drude part of the spectrum at low energies that have a the consequence of an increase of the spectral weight at higher energies (see Section 6.4.1). This is confirmed by the integration of the spectral weight of the Drude part as a function of the temperature (see Figure 6.31): integrating at very low frequencies (0-0.1 eV) the result of an effective heating is a broadening of the Drude peak

with a reduction of its spectral weight in the low-frequency range. In the underdoped sample the behaviour is opposite and the spectral weight at high energies decreases. Also the effect at low frequencies is opposite. This suggest a completely different description of the effect of the temperature on the system and we have seen that our analysis confirms that. The DMFT calculations may suggest a spectral weight decreasing (i.e. a reduction of the intensity of the oscillators of the interband transitions) that moves towards lower frequencies to compensate the reduction of the Drude part due to an effective heating. In our previous analysis (see Section 6.6.2) we couldn't appreciate this effect. We can reproduce the non equilibrium data just with a redshift of the oscillator maintaining constant its intensity. The reason of that could be that the effect of a reduction of the intensity is much lower than a shift of the oscillator and, even though present, it is not appreciable. In the future, more quantitatively analysis on this problem could provide more solid answers.

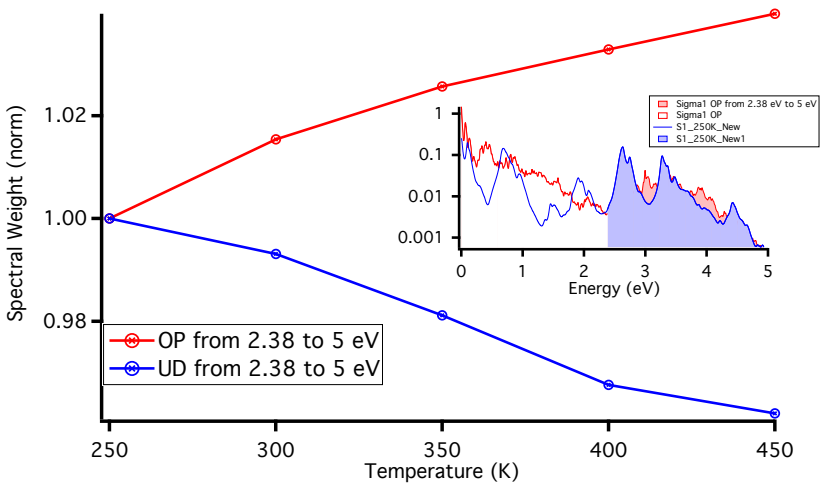

Figure 6.30: Evolution of the spectral weight of the optical conductivity $\sigma_1(\omega)$ integrated over a frequency range of 2.4-5 eV for two doping levels: optimally doped (red) under doped (blue). The spectral weight has been normalized on the lowest temperature value. The optical conductivity data are obtained with DMFT calculations and are reported in the inset for just the lowest temperature. The solid blue and red areas indicate the range of frequencies used for the integration.

6.6.4 *Time-Domain Analysis*

As shown in Figure 6.32, the transient reflectivity $\Delta R/R(\omega)$ presents a clear evolution in time. We show in Figure 6.32, as an example, the data referring to the UD12 sample. Taking four frequency traces at different delays (50, 100, 200, 600 fs) reported in the second panel of Figure 6.32, we note that the intensity of this variation is maximum around 50 fs while decreasing for larger delays. As already discussed in the previous section, this negative variation is reproduced by a redshift of the charge-transfer oscillator around 2 eV. We have fitted the $\Delta R/R(\omega)$ for each delay in the range $-200 \div 800$ fs and

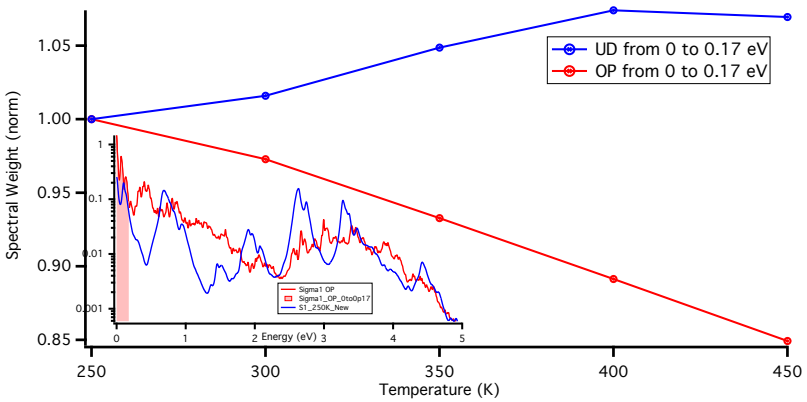

Figure 6.31: Evolution of the spectral weight of the optical conductivity $\sigma_1(\omega)$ integrated over a frequency range of 0-0.1 eV for two doping levels: optimally doped (red) under doped (blue). The spectral weight has been normalized on the lowest temperature value. The optical conductivity data are obtained with DMFT calculations and are reported in the inset for just the lowest temperature. The solid blue and red areas indicate the range of frequencies used for the integration.

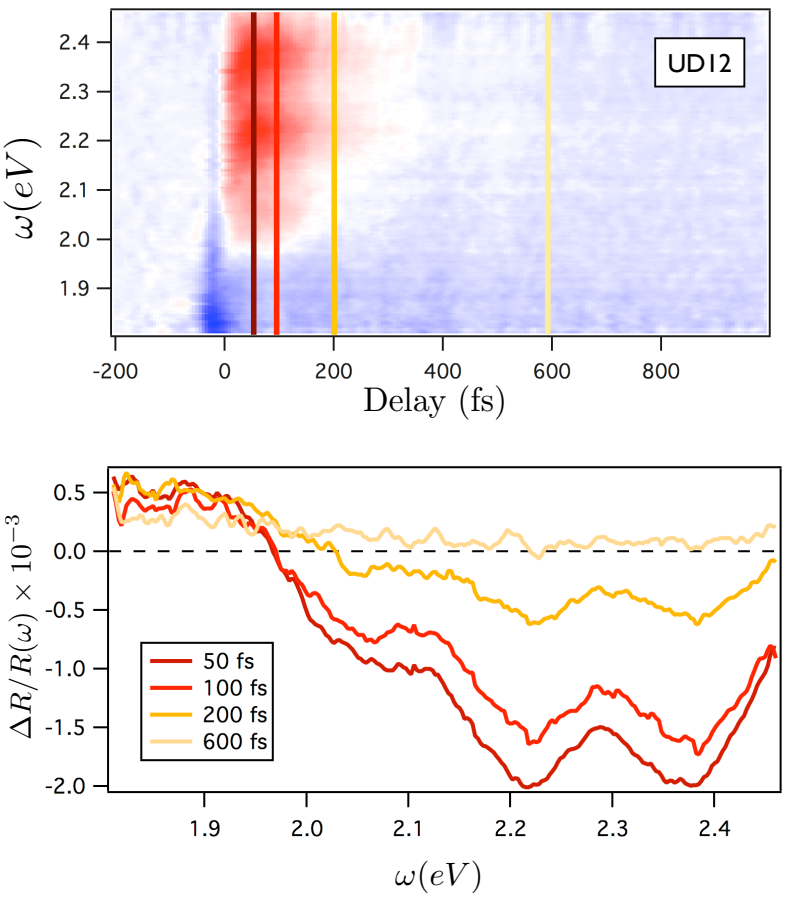

Figure 6.32: a) Transient reflectivity $\Delta R/R(\omega, \tau)$ of the UD12 sample. The four lines represents the position of the slices taken at different delays: 50, 100, 200, 600 fs. The reflectivity variation at such delays are reported in the second panel of the figure.

we plot the amount of the redshift as a function of the time in Figure 6.33. The equilibrium position of the oscillator is set at 2.19 eV; the maximum shift of the oscillator in respect to the equilibrium position is reached at 44 fs after the external excitation (see the inset) and then it decreases exponentially with a dynamics of 117 fs. This decay time is obtained by fitting the trace with a single negative exponential $f(t) = I \exp^{-t/\tau}$

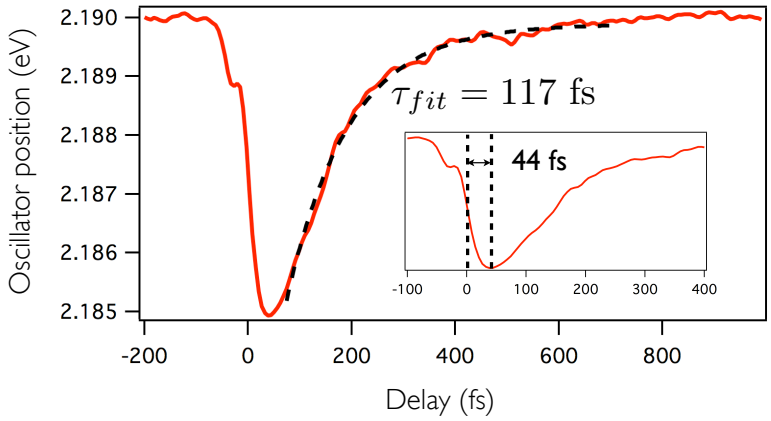

Figure 6.33: Redshift of the charge-transfer oscillator from the equilibrium position due to the external excitation for each delay. The red curve is obtained fitting the transient reflectivity slicing the matrix in Figure 6.32 at each delay. The dynamics of 117 fs (dashed black curve) is obtained fitting the red curve with a single exponential. The inset shows that the maximum redshift (that corresponds to the maximum of the reflectivity variation) is obtained after 44 fs.

In the insets of Figure 6.21 we have reported $\delta\phi(t)$ obtained through SVD (see Figure 6.21) In order to fit these curves we

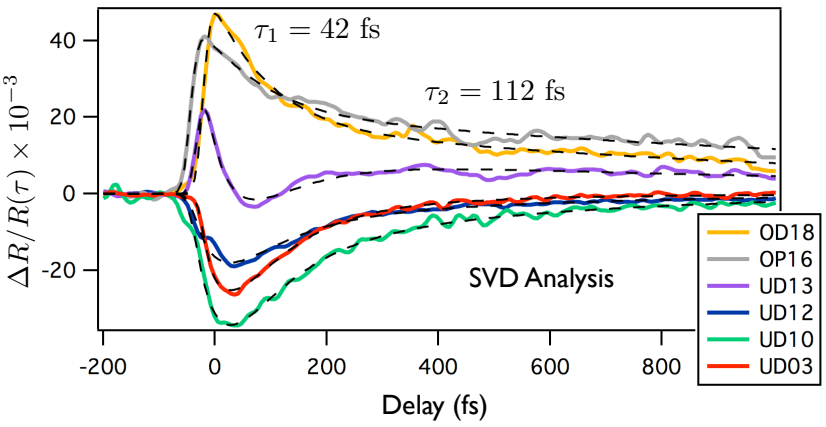

Figure 6.34: Transient reflectivity $\Delta R/R(\tau)$ as a function of the delay for the six doping. These curves are not just a slice of the data matrices at a certain photon energy but are obtained using SVD analysis. The best fits (dashed black lines) have been made using a double exponential decay as fit function. The two parameters, $\tau_1 = 112$ fs and $\tau_2 = 42$ fs, that comes out from the fit are the same for each doping.

have used a triple exponential decay, convolved with a Gaussian curve, which takes into account the temporal profile of the pump and probe pulses (with the full width at half maximum = 25 fs). The exponential decay function used for the fit is given by:

$$f(t) = I_1 e^{-t/\tau_1} + I_2 e^{-t/\tau_2} + I_3 e^{-t/\tau_3} \tag{6.4}$$

Given the gaussian width of 25 fs (extracted from the convolution between the pump and probe pulses) and the time zero, the free parameters needed to fit the data are six: I_1, I_2, I_3, τ_1, τ_2 and τ_3. We want to check if the relaxation dynamics are the same for all the samples. To do that we have used a "global fitting" that permits to fit the six traces simultaneously linking together some parameters (in this case the decay times τ_i). It turns out that the three decay times are constant through all the doping and read: $\tau 1 = 42$ fs, $\tau_2 = 112$ fs and $\tau_3 = 1140$ fs.

The positive fast component relative to the decay time τ_1 is responsible for a delayed response of the under-doped samples at the external excitation. This delay is given by the position of the maximum in respect to the time-zero and it is of the order of $\tau_1 \simeq 40$ fs. This is consistent with the results shown in Figure 6.33 where we had found that the maximum redshift of the charge-transfer oscillator occurred at 44 fs in UD12 sample.

The third exponential component has a very slow decay ($\tau_3 = 1140$ fs) and it reproduces the $\Delta R/R(t)$ at long delays when the system is completely thermalized.

The main differences in the fitting results with the doping regards the coefficient I_2. Even though its relative decay time τ_2 remains constant, I_2 changes sign and intensity moving from the over to the under doped regime. Figure 6.35 shows the intensity of I_2, as a function of the hole doping, extracted by the best fit. In the overdoped sample I_2 is positive and decreases (changing sign) until the $p = 0.10$ and $p = 0.03$ doping where it is almost constant.

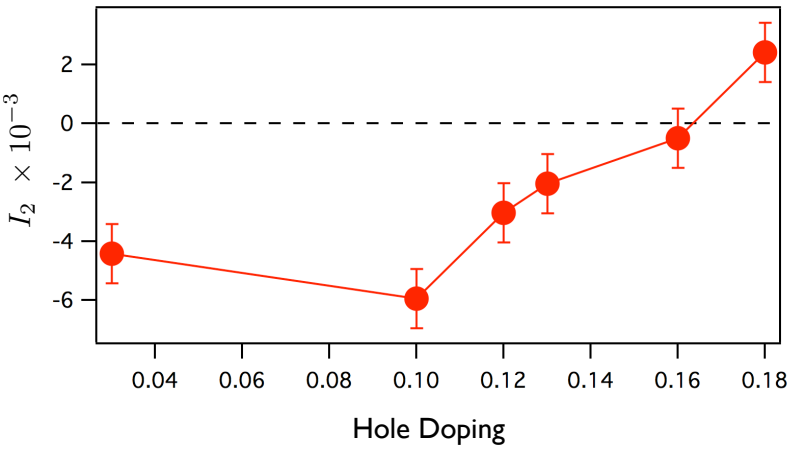

Figure 6.35: Evolution of the coefficient I_2 with the doping. Its values are extracted by fitting the experimental data in Figure 6.34. Between $p = 0.18$ and $p = 0.16$ doping, I_2 changes sign and becomes negative.

No negative signal is present in the OD18 and OP16[4]. If we set I_2 to zero for the OD18 and OP16 and we consider I_2 only when it is negative, i.e. in the UD samples, we can compare the results of

[4] within the error bar, we can consider $I_2 = 0$ for the OP16.

the analysis in the time-domain (Figure 6.35) with the analysis in the frequency-domain (Figure 6.29). We report the intensity of the negative reflectivity variation I_2 together with amount of the redshift $\Delta\omega_0$) of the charge-transfer oscillator at 2 eV in Figure 6.36. Their behaviour is very similar confirming that the time and the frequency domain analysis are consistent.

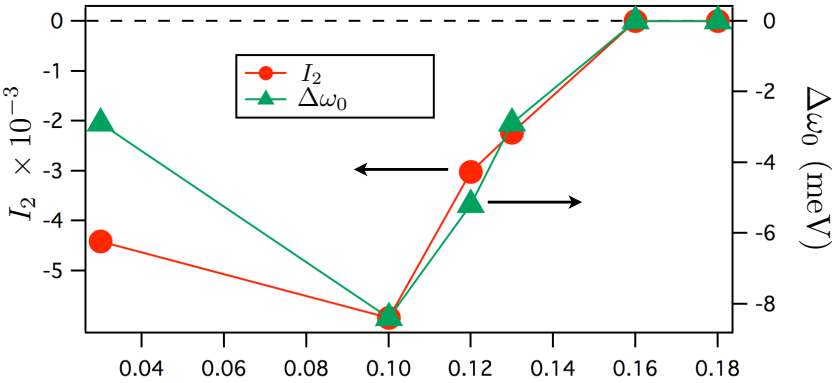

Figure 6.36: Intensity of the negative reflectivity variation I_2 (red) together with amount of the redshift $\Delta\omega_0$) of the charge-transfer oscillator at 2 eV (green).

A last comment can be done on the time domain behaviour of the UD10 sample from the data obtained with the oscillator-based system and already shown in Figure 6.23. The fit analysis on the negative variation of the reflectivity at 2.05 eV (Figure 6.37) shows that the dynamics can be reproduce using just a single exponential with a decay time $\tau = 132$ fs. This is confident with the $\tau_2 = 112$ fs obtained on the OPA system with a much higher time resolution.

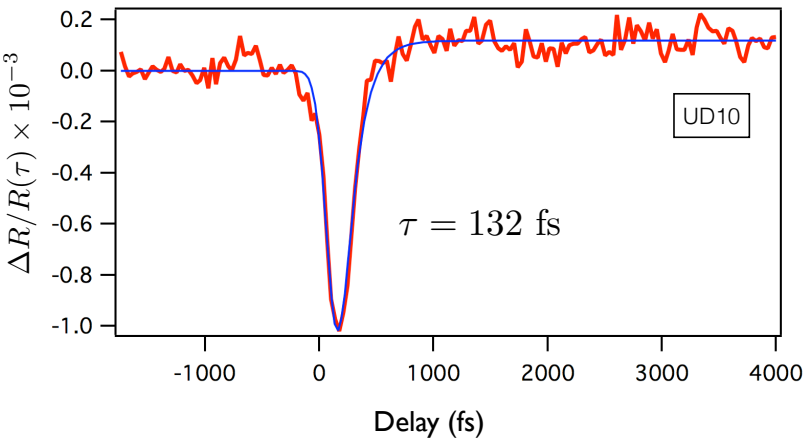

Figure 6.37: Dynamics of the UD10 sample at 2.05 eV of photon energy. The trace is described by a single negative exponential with a decay time $\tau = 132$ fs. The data are taken with the oscillator system with a pulse length of 120 fs.

To conclude we have seen that the transient reflectivity obtained by the experimental data have the same relaxation times for all the

doping and are characterized by: 1) a finite build-time of the order of 40 fs that suggest a formation of the excited state that mediated by spin fluctuations [Lenarčič and Prelovšek, 2013] [Golež et al., 2014]; 2) the decay time of $\sim$ 110 fs that is compatible with a "cooling" of the system that exchange energy with the strong coupled phonon [Dal Conte et al., 2012] before being thermalized with the rest of the lattice on a longer time scale. The global fitting analysis assures that, even in the under doped samples, where the redshift of the charge-transfer oscillator occurs, the cooling is realistically correlated to the electron-phonon coupling.

6.6.5 *Discussion and Conclusions*

Our analysis lead to a clear result: exists a precise doping level which separates two regions in the doping-temperature phase diagram of Bi2201. In these two regions, the response of the system to an external ultrafast excitation can be rationalized in the following way:

- at $p < p_{cr}$, the effect of the pump excitation is to redsfhit the oscillator describing the charge-transfer excitation at 2 eV;
- at $p > p_{cr}$, the effect of the pump is just a more conventional increase of the effective temperature of the system with a consequent increase of the number of bosons through which the electrons can dissipate the stored energy. No modification of the oscillators parameters at high energy occurs.

Thanks to the time-resolved technique, that permits to investigate the state of the system out of equilibrium, we have demonstrated a discontinuity of the ultrafast dynamics of Bi2201 at $p = P_{cr}$ and $T = 300$ K. This critical doping is very close to the optimal doping that define the doping at which the maximum critical temperature T_C for the superconductivity occurs. The region around the optimal doping has attracted the attention of the scientists because there are many experimental evidences that suggest the presence of a quantum critical point at zero temperature. For example, there are evidences (from specific heat data [Tallon et al., 1994] and from recent Fermi velocity anomaly [Vishik et al., 2012]) that the quantum critical point can involve the termination of the pseudogap order inside the superconducting dome. Moreover, X-ray measurements on YBCO [Ghiringhelli et al., 2012] [Achkar et al., 2012], $Bi_2Sr_{2-x}La_xCuO_{6+\delta}$ [Comin et al., 2014], and $Bi_2Sr_2CaCu_2O_8$ [da Silva Neto et al., 2014] detected a static incommensurate charge-density-wave (CDW) order. The onset temperature $T_{CDW}(p)$ of the CDW order was found to be smaller than $T^*(p)$ but follows a similar doping dependence. Furthermore ARPES measurements deep under the superconducting dome

have found [He et al., 2011] [Zhao et al., 2013] a dramatic change in the form of the superconductive gap anisotropy with reduced carrier concentration at a certain doping, and were interpreted as evidence for the existence of a quantum-critical point (QCP) at $p = p_{cr}$, at which a new order emerges. It is tempting to associate this emerging order with CDW. Other experimental evidences have pointed out the presence of another quantitative order parameter representing intra-unit-cell nematicity in cuprates, i.e. the breaking of rotational symmetry by the electronic structure within each CuO_2 unit cell [Lawler et al., 2010]. Concomitantly to all these charge orders it has been recently shown that the electronic symmetry-breaking tendencies weaken with increasing p and disappear close to a critical doping p_{cr} giving origin to a discontinuity on the topology of the Fermi surface in cuprates [Fujita et al., 2014].

In recent theoretical studies [Wang and Chubukov, 2014] it has been demonstrated that, within the spin-fermion model[5] in hole-doped cuprates continuous and discrete symmetry breaking occurs giving origin to different orders under the pseudogap. Upon lowering temperature, at a certain $T_n < T^*$ the system develops a nematic order [Fernandes et al., 2012]. Then, at a smaller $T_t \leq T_n$ another composite order parameter becomes nonzero breaking the time-reversal symmetry [Tsvelik and Chubukov, 2014]. Finally, below $T_{CDW \leq T_t}$ the system develops a CDW order. T_{CDW} decreases when the magnetic correlation length ξ decreases and vanishes at some finite ξ, setting up a charge QCP at some distance away from the magnetic instability. The ideas about a nonmagnetic QCP at around optical doping have been presented in earlier publications [Varma, 1997] [Castellani et al., 1994] [Varma, 2006]. The onset temperatures of nematic and TRS-breaking composite orders follow the same doping dependence as T_{CDW} and near the critical ξ T_{SC} is higher than both T_{CDW} and T_n, and at larger dopings (smaller ξ) only superconducting order develops.

A comprehensive phase diagram of this picture is shown in Figure 6.39. Anyway, the existence and the precise location of the CDW QCP is still a point of debate. Does the QCP exist at finite doping p_{cr} and, if this is the case, which is the value of that doping concentration? Is the actual position of p_{cr} an accidental consequence or it is a result of a reorganization of the electronic properties that occurs already at much higher temperatures? With our work we want to give a contribution in answering these fundamental questions. In the present work we have shown that the ultrafast dynamics of the charge-transfer oscillator at 2eV unveils a novel scenario for the phase diagram of Bi2201.

[5] This model describes low-energy fermions with the FS shown in Figure 6.38 and with four-fermion interaction mediated by soft spin collective excitations peaked at or near (π, π)

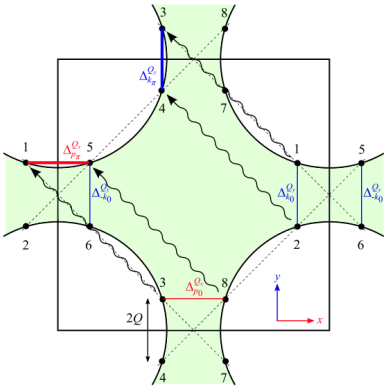

Figure 6.38: The Fermi surface, Brillouin zone, and magnetic Brillouin zone (dashed line) of the spin-fermion model. Hot spots are defined as intersections of the FS with magnetic Brillouin zone. The hot spot pairs 1-2 and 3-4 denote the CDW pairing we consider. They are coupled through the antiferromagnetic exchange interaction peaked at momentum (π, π), as shown by the dashed arrows.

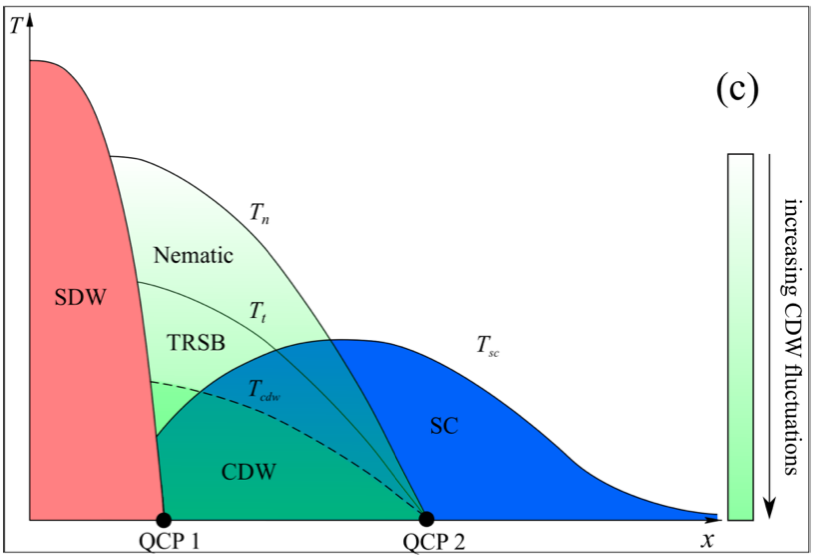

Figure 6.39: The full phase diagram, which includes the competition between superconductivity and charge order. QCP1 and QCP2 are quantum-critical points towards SDW and CDW order, respectively. The behavior of superconducting T_{SC} and the onset temperatures for charge order T_n, T_t, and T_{CDW} are shown. T_n is the preemptive nematic transition temperature, and T_t is the temperature below which a $q = 0$ order emerges, breaking time-reversal symmetry. [Wang and Chubukov, 2014]

Charge-Transfer Redshift and CDW In order to compare the doping evolution of the transient redshift of the CT transition to that of the CDW order, we report in Figure 6.40 the intensity of the negative exponential decay (I_2, see Figure 6.36) which is proportionals to the amplitude of the CT redshift, and the intensity of the REXS measurements performed on the same sample ($Bi_2Sr_{2-x}La_xCuO_{6+\delta}$). REXS uses X-ray photons to exchange momentum with the electrons and the ionic lattice, in order to gain information on the electronic charge distribution. As opposed to conventional X-ray diffraction, which is widely used for structural studies, in REXS the photon energy is tuned to resonance with one of the element-specific absorption lines. This results in a strong enhancement of the sensitivity to the valence electrons, and allows the detection of very small variations in the electronic density profile within the CuO_2 planes [Abbamonte et al., 2005], which are difficult to determine using nonresonant methods. The amplitude of the signal related to the CDW peak vanishes at the doping $p_{cr} = 0.16 \pm 0.01$, that can be considered as the doping at which the zero temperature QCP occurs. The doping evolution of the redshift of the charge-transfer oscillator follows the same behavior and vanishes at the same doping ($p = 0.16 \pm 0.01$). Therefore, we can conclude that the pump excitation induces an ultrafast redshift of the CT peak only below a critical doping level that is the same that identifies the presence of a QCP at zero temperature, i.e. $p_{cr} = 0.16 \pm 0.01$. It is crucial to stress that the ultrafast technique directly probes the high energy scale (2 eV) associated to the CT excitation, that is inaccessible to conventional equilibrium spectroscopies which are

sensitive to the thermal excitations extending over an energy range of kT from the fermi level.

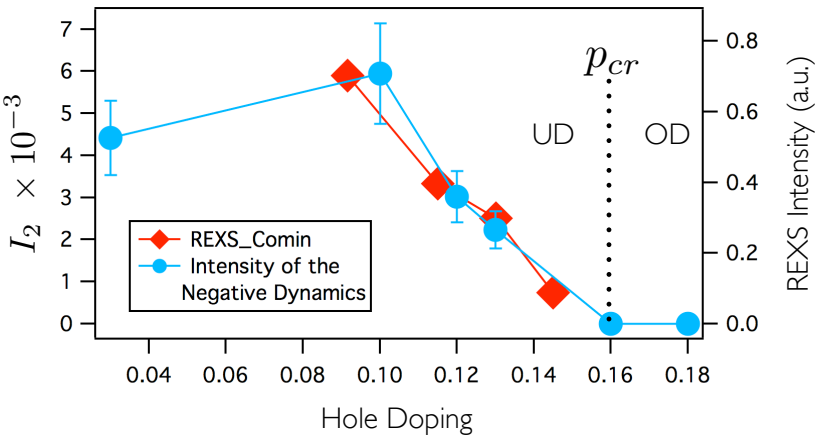

Figure 6.40: Comparison between the evolution of the coefficient I_2 and the intensity of the REXS on Bi2201 with the doping. The level of doping where both of them vanishes is $p = 0.16 \pm 0.01$ and it is the same.

Origin of the Charge-Transfer Redshift In the following section we try to give a microscopic explanation of the origin of the observed redshift of the CT transition. We start discussing the CT process in the insulating parent compound. In this case, as we have already seen in Section 2.1, the electronic structure is mainly determined by the CuO layers. In Figure 6.41 we reports the $3d_{x^2-y^2}$ orbitals of the copper (blue) with the $2p_{x,y}$ orbitals of the oxygen (orange). The

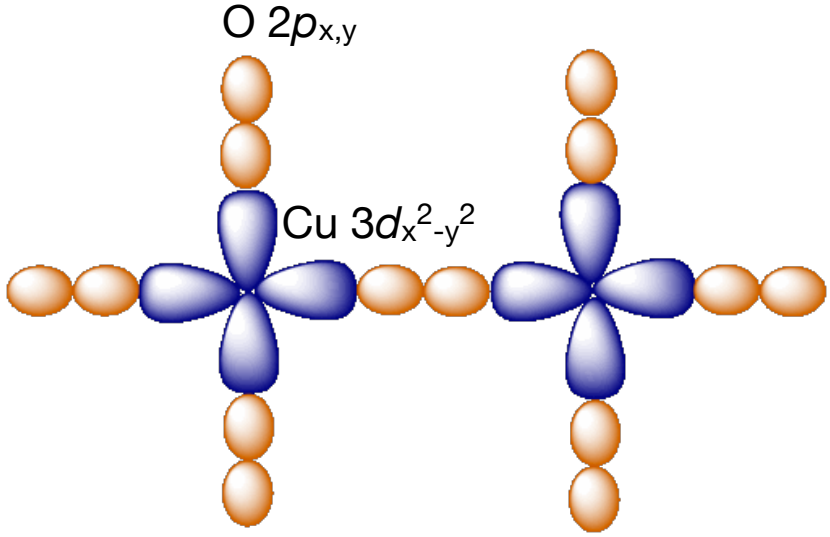

Figure 6.41: Configuration of oxygen $2p_{x,y}$ and copper $3d_{x^2-y^2}$ orbitals in cuprates.

fundamental excitation of this system occurs when $\hbar\omega > \Delta_{CT}$. The

effect is to remove an electron from the oxygen $2p_{x,y}$ and move it on the copper $3d_{x^2-y^2}$. The effect is to create a double occupation on the copper orbital (doublon) and have no occupation on the oxygen orbital (holon). Alternatively we can think to a hole that moves from the copper to the oxygen giving origin to a so called *CT exciton*. The situation is presented in Figure 6.42 This kind of exciton is called

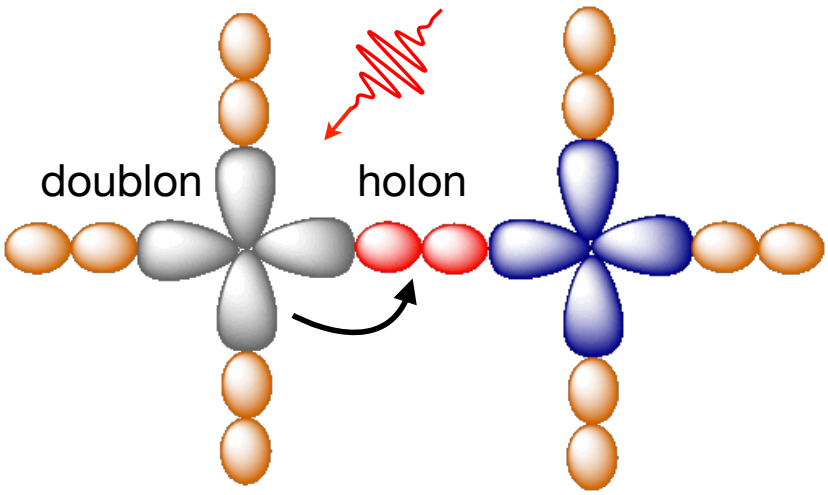

Figure 6.42: Frenkel exciton. One electron from the oxygen $2p_{x,y}$ is removed and transferred to the copper $3d_{x^2-y^2}$ orbital. The effect is a formation of a polaron with a double occupation on the copper (doublon) and a vacancy on the oxygen (holon). This state is a localized state that eventually can move around in the system but keeps being bounded.

Frenkel exciton that, contrary to the Mott-Wannier variety which are spread out over many unit cells, has a short-range nature and involves two nearest neighbours in the same unit cell. It has been demonstrated [Falck et al., 1992] that this exciton, if coupled with a phonon or, more in general with any boson excitations, leads to a shift of the charge-transfer band edge with a defined temperature dependence. For such excitons, the T dependence of the exciton self-energy causes a shift [Fan, 1951] of the band edge given by:

$$E_g(T) = E_g^0 - 2\hbar\omega_0\alpha_p[n(\hbar\omega_0/k_BT) + 1] \tag{6.5}$$

where n is the Bose-Einstein occupation number, ω_0 is the frequency of the mediating boson and the exciton coupling constant is defined as:

$$\alpha_p = \frac{1}{2}\frac{e^2}{2\hbar\omega_0}\left[\frac{1}{\epsilon_\infty} - \frac{1}{\epsilon_s}\right]\left[\frac{2m\omega_0}{\hbar}\right]^{1/2} \tag{6.6}$$

A representation of the mechanism of the formation of a polaron mediated by a boson is sketched in Figure 6.43. This formalism has been successfully used, for example, to describe the temperature evolution of the charge-transfer edge in the La_2CuO_4 [Falck et al., 1992] (see Figure 6.44).

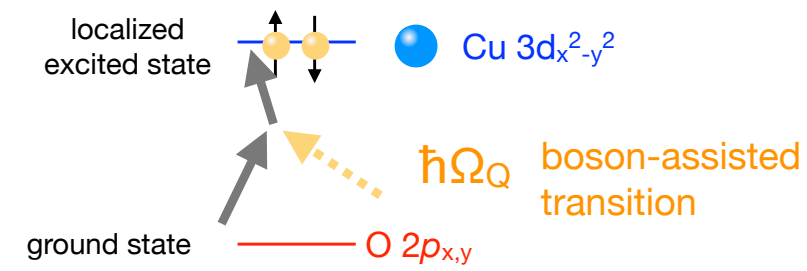

Figure 6.43: Dressed exciton. The energy gap between the ground state of the oxygen $2p_{x,y}$ and the excited localized state of the copper $3d_{x^2-y^2}$ is reduced by the absorption of a quantum of boson with energy $\hbar\Omega_Q$

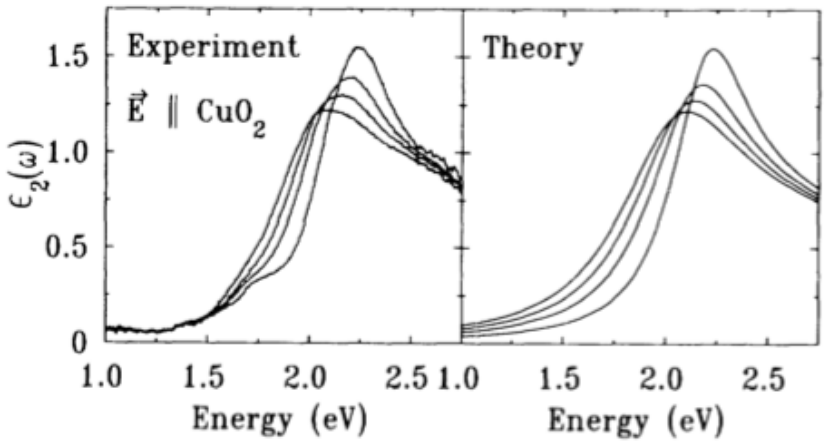

Figure 6.44: The in-plane $\epsilon_2(\omega)$ for four different temperatures together with the best fit to the La_2CuO_4 data using the formalism explained in the text. All four temperatures are shown in the upper panel; theory and experiment are compared for individual temperatures in the lower panel.

Regarding a doped material as the $Bi_2Sr_{2-x}La_xCuO_{6+\delta}$, we have seen, from our experimental data, that there is a critical doping below which the redshift of the CT oscillator occurs. The doping level is related to the correlation of the system: the lower the doping the larger the correlation. The formation of the Frenkel exciton is possible only in a correlated system where the correlation strength is enough to generate a short-range electron-hole interaction in the same unit cell. On the contrary, when the final state of the excitation is a completely delocalized wave function, i.e. when the wave function of the electron snatched from the oxygen orbital is spread out over a large number of unit cells, the Frenkel exciton is prevented. The excited state is so screened by the very large dielectric function of a metal-like system and no redshift of the CT excitation occurs.

At this point it is possible to divide the phase diagram of the cuprates in two regions delimited by the critical doping at wich a redshift of the charge transfer oscillator occurs. The result is shown in Figure 6.45 where we have indicated with red(blue) dots the doping concentrations at which the photoinduced redshift of the CT is (not) observed. The red line indicates the position of the critical doping $p = 0.16$. Panel b) reports the same graph than Figure 6.40 to underling the fact that the critical doping extracted from our analysis on the charge-transfer redshift corresponds to the critical doping extracted from the REXS data.

In order to summarize the main results of the present work we can say that in the $Bi_2Sr_{2-x}La_xCuO_{6+\delta}$ it is possible to define a critical doping level p_{cr} or, alternatively a critical correlation length ξ_{cr}, that separates two distinct region of the doping-temperature phase diagram of this material. The response of the system to an external excitation is different in the two regions:

- below the critical doping the external excitation, due to a laser pulse, causes a redshift of the CT oscillator. This redshift is a direct consequence of the formation of a hole-electron polaron that occurs between the $Cu - 3d_{x^2-y^2}$ and $O - 2p_{x,y}$ orbitals when the excitation between the oxygen ground state to the copper double occupation is mediated by a boson. The CT peak redshift is independent of the pump energy (1.5, 1.9, 3 eV). From the time domain analysis comes out that the build up time of such localized polaron is not instantaneous but is compatible with AF fluctuations (40 fs) [Lenarčič and Prelovšek, 2013] [Golež et al., 2014]. The decay time of the excited state is compatible with the electron-phonon "cooling" (100 fs). The critical doping $p_{cr} = 0.16 \pm 0.01$ marks out the transition in the Fermi surface topology (nematicity), the transition in the charge-ordering and now the transition in the high-energy physics (CT redshift) at 300

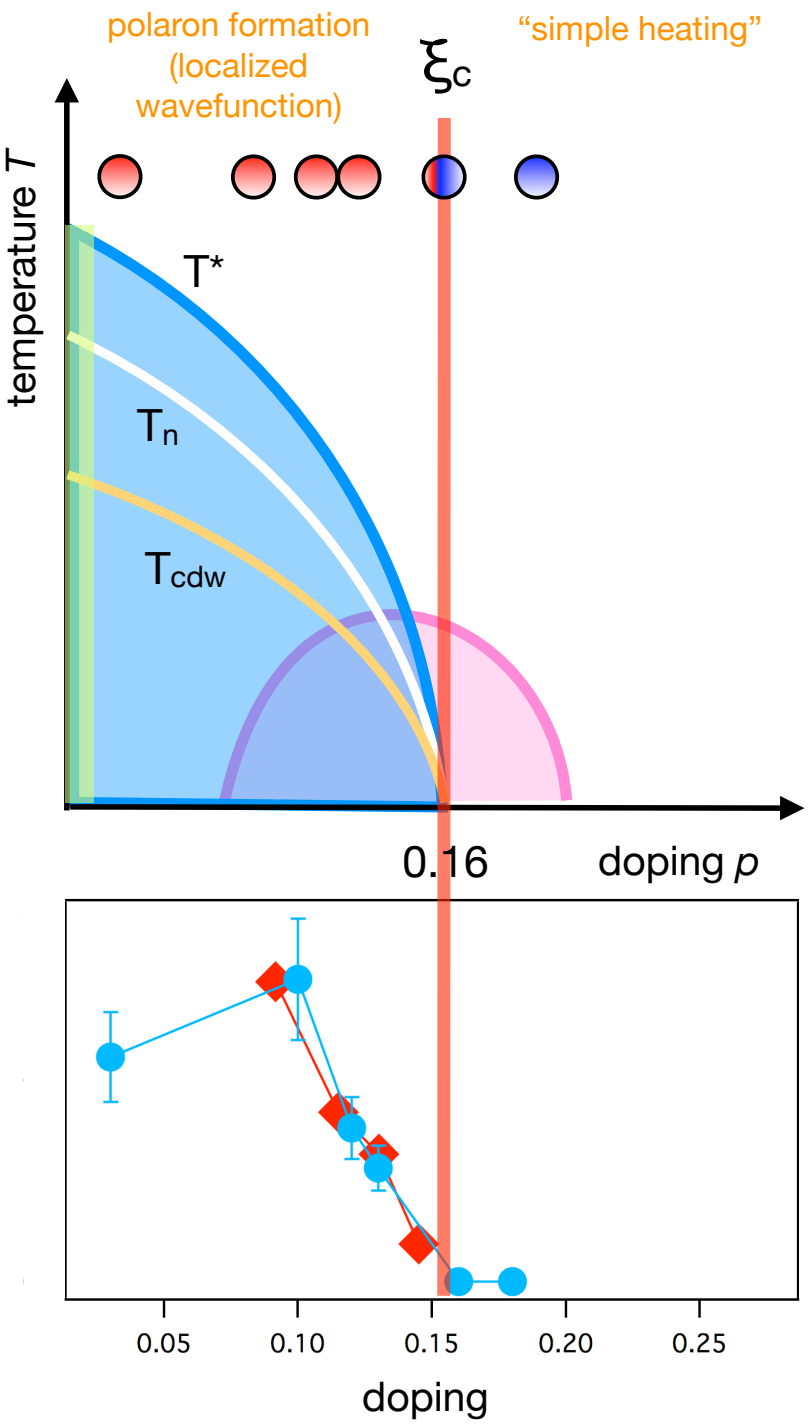

Figure 6.45: Comprehensive phase diagram of the Bi2201. Together with the doping and temperature evolution of the charge-ordered phases (already discussed in Figure 6.39) we have indicated with red(blue) dots the doping concentrations at which the photoinduced redshift of the CT is (not) observed. The vertical red line indicates the position of the critical doping above which REXS intensity and redshift of the charge transfer oscillator disappear.

K. The presence of the QCP at this precise doping $p_{cr} = 0.16 \pm 0.01$, suggested by low-energy technique, is a direct consequence of the modification of the electronic properties that occurs already at higher temperatures.

- above the critical doping the system moves toward a more conventional metal-like behaviour where the formation of hole-electron excitons is no longer a good description. The states are no longer localized but are spread out over many unit cells and the effect of the external excitation can be reduced to a simple heating of the effective temperature of the system well described by an increasing of the number of bosons through which the system relaxes with the characteristic decay time electron-phonon coupling.

7 UV time-resolved photoemission on the doped double-layer copper oxide Bi2212

Among the main issues of high-temperature superconductivity that defy an explanation in the framework of the Bardeen-Cooper-Schrieffer (BCS) theory of conventional superconductors, we focus on the following issue: In the BCS theory of conventional superconductors, the superconducting phase transition is accompanied by a modification of the electronic density of states over a frequency range of the order of the superconducting gap (SC), without significantly affecting the physical properties at higher energies [Tinkham, 2004]. In contrast to this, in strongly correlated systems like cuprates, the electronic properties at the Fermi energy (E_F) are intertwined with those at high-energy scales. One of the pivotal challenges in the field of high-temperature superconductivity is to understand whether and how the high-energy scale physics associated to high-energy Mott-like excitations ($|E - E_F| > 1$) is involved in the condensate formation. A huge effort is currently devoted to develop novel spectroscopic techniques, beyond conventional spectroscopies at equilibrium, to provide new informations and solve this issue, paving the way to finally develop a theory to explain high- temperature superconductivity.

The very recent development of novel time- and frequency-resolved spectroscopies, based on the supercontinuum light produced by a photonic crystal fiber seeded by a short pulse, allowed to finally solve the question about the origin of the superconductivity-induced modifications of the high-energy optical properties. Being able to disentangle the ultrafast modifications of the electronic processes from the slower broadening of the Drude-like peak induced by the complete electron-phonon thermalization, the interplay between particular many-body electronic excitations at 1.5 and 2 eV and the onset of superconductivity has been demonstrated [Giannetti et al., 2011]. However, although the relation between high-energy optical

transitions and superconductivity has been finally proved, many questions are still to be answered. The rate of an optical transition depends on three terms: i) the strength of the matrix element describing the transition; ii) the density of states of the initial filled levels; iii) the density of states of the final empty levels. The superconductivity-induced variation of optical transitions at 1.5-2 eV can be attributed to any of these three causes, without any clue to unambiguously solve the problem. In order to do that, one could use traditional time-resolved ARPES, but the maximum photon energy 6 eV, combined with the work function of the material, is not enough to investigate these states with $E_B = 1.5 - 2$ eV. Here we report time-resolved measurements performed at the beamline ARTEMIS of the Rutherford Appleton Labs (UK). Exploiting high-harmonics (>15 eV) generated in gas jet, we have measured, for the first time, the dynamics of the states at $E_B \simeq 1.5$ eV. We have demonstrated a spectral weight variation related to the holes excitation in the conduction band. The understanding of the origin of such phenomenon and of the mechanism of the energy exchange between the holes and the electrons that occupy the oxygen bands at 1.5-2 eV binding energy, may be the key to understand their connection with the superconductivity.

7.1 *Electronic structure*

The bismuth strontium calcium copper oxide superconductors are the most studied high-temperature superconductors together with yttrium barium copper oxides (abbreviated YBCO).

The general chemical composition of these compounds is $Bi_2Sr_2Ca_nCu_{n+1}O_{2n+6+\delta}$. The $n = 1$ sample is called Bi2212 and has attracted more attention than the other compounds of the same family. The main building blocks of the crystal structure are the CuO_2 planes that are separated each others by additional BiO, SrO and Ca planes as we can see looking at the unit cell of the Bi2212 shown in Figure 7.1. The superconductive currents are localized in the two-dimensional CuO2 planes and they start to occur at low temperature upon doping the system with holes. This effect is obtained by adding interstitial oxygen atoms which take position in the BiO planes: the critical temperature strongly depends on the amount of extra-holes and in the specific case of $Bi_2Sr_2CaCu_2O_{8+\delta}$, it reaches the maximum value of 95 K in correspondence with an excess density of about 0.16 holes per Cu atom.

All the measurements we will show in the next chapters are performed on Yttrium doped Bi2212. The substitution of Yttrium for Calcium atoms has the effect to stabilize the 1:1 ratio between Bi and Sr sites and, for 8% of Y doping, to increase the maximum critical

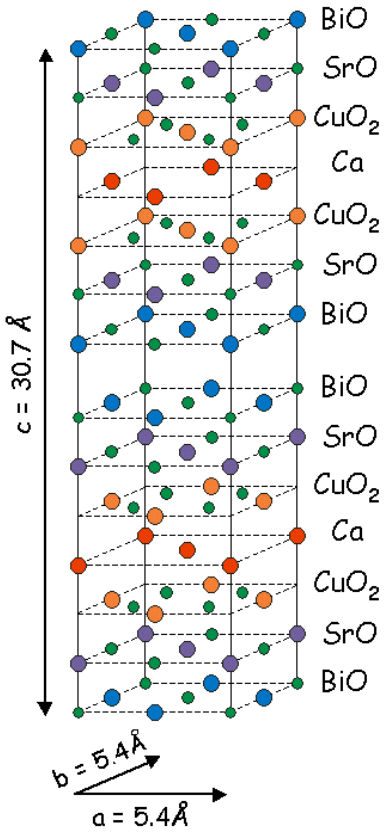

Figure 7.1: The unit cell of Bi2212

temperature to the value of 96 K [Eisaki et al., 2004]. The resulting chemical formula of this compounds is: $Bi_2Sr_2Ca_{0.92}Y_{0.08}Cu_2O_{8+\delta}$.

7.2 *Optical properties at equilibrium*

The electronic properties of the Bi2212, as in the other cuprates, are mainly determined by the CuO_2. For this reason we refer to Section 2.1 for a detailed description of the copper-oxygen electronic properties in cuprates.

Here we present the optical properties of the Bi2212 at equilibrium. The following data have been already published in [Giannetti et al., 2011] and help in the comprehension of the optical properties of the Bi2212 at equilibrium. In Figure 7.2 the imaginary part of the dielectric function $\epsilon_2(\omega)$ and the real part $\epsilon_1(\omega)$ (in the inset) of Bi2212 is shown. The intraband optical region under 1.25 eV

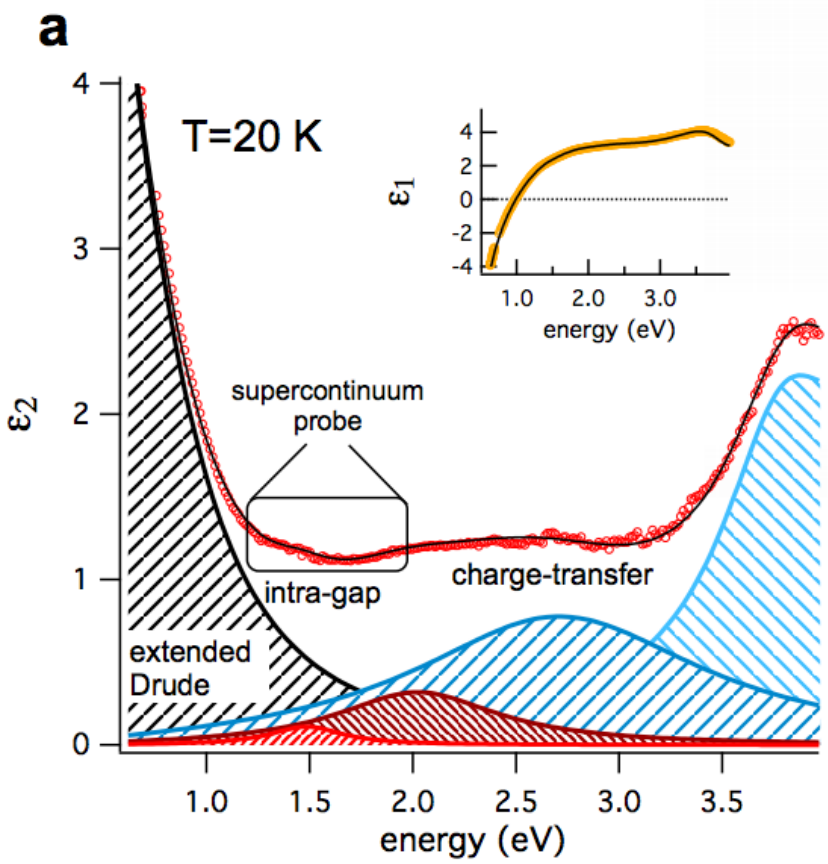

Figure 7.2: The high-energy region of the imaginary part of the in-plane dielectric function, measured at T=20 K for the OP96 sample is shown. The thin black line is the fit to the data described in the text. The contributions of the individual interband oscillators at $\omega_{0,i}$=1.46, 2, 2.72 and 3.85 eV are indicated as colour-patterned areas. [Giannetti et al., 2011]

(10000 cm^{-1}) is dominated by a broad Drude peak. In the high energy region ($\hbar\omega > 1.25$) the optical response is dominated by the interband optical transitions. The best fit to the data (solid line), as

the analysis of Bi2201 in the previous chapter, is obtained modelling the equilibrium optical conductivity $\sigma_{eq}(T,\omega)$ as in Equation 6.1. The optical properties are satisfactorily reproduced over the whole spectrum, considering, in addition to the extended Drude model, two mid-infrared (MIR) peaks in the intraband region ($\sim$0.5, 0.8 eV), whose origin has been already discussed in Section 3.4. The interband transitions in the near-IR/visible/UV spectral range are reproduced using six Lorentz oscillators at $\simeq$1.45, 2, 2.7, 3.85, 4.36 and 5 eV. The identification of the interband transitions with specific electronic excitations is an open issue as well. Many efforts have been devoted to give a possible interpretation studying the temperature and doping behaviour of the optical conductivity. A common feature observed in all undoped compounds is a suppression of spectral weight below 2 eV due to the presence of a charge-transfer (CT) gap. Adopting the hole-picture, the charge-transfer process is explained in terms of a hole transfer from the upper Hubbard band with $d_{x^2-y^2}$ symmetry to the O-2$p_{x,y}$ orbitals. Increasing the doping level of the sample, the energy region below the gap is partially filled by states at the expense of the spectral weight related to the CT excitations of the undoped compound. However the feature associated to the CT gap clearly persists in the finite doping region.

Dynamical mean field calculations of the electron density of states and optical conductivity in an hole-doped three-band Hubbard model [de' Medici et al., 2008], recently found that the Fermi level moves into a broad ($\simeq$2 eV) and structured band of mixed Cu-O character, corresponding to the Zhang-Rice singlet states, in agreement with previous experimental results [Brookes et al., 2001]. The structures appearing in the optical conductivity at 1-2 eV, i.e. below the reminiscence of the CT gap (2.5-3 eV), are related to transitions between mixed Cu-O singlet states with different symmetries.

One of the possible interpretation of the feature of the optical conductivity at 1.5-2 eV is that it could be linked with the oxygen bands at $E_B = 1.5$ eV. In fact, in [Shen et al., 2004], where ARPES measurements at different doping levels on $Ca_{2-x}Na_xCuO_2Cl_2$ have been performed, they have been proved that the prominent structure at 1-2 eV is due to the oxygen O-2p_π band arranged in an in-plane antibonding configuration at (π,π) (see Figure 7.4) with an estimated separation of $\simeq$3 eV from the bonding configuration at $\mathbf{k} = (\pi,\pi)$ [Mattheiss and Hamann, 1989], although hybridization of the bonding band with the Cu-3d_{xy} orbital modifies this value by up to $\simeq$2 eV [Hayn et al., 1999]. The O-2p_π states are not bonding with the Cu-3$d_{x^2-y^2}$ because they are transversal to them with a weak superposition (see Figure 7.3). Figure 7.4(b) shows the evolution of the position of this band with the doping level.

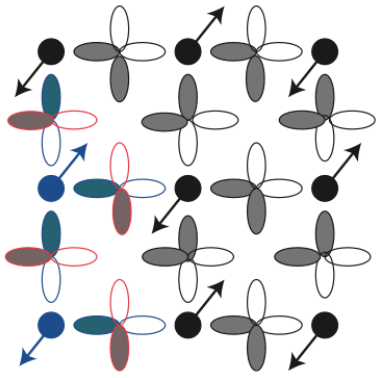

Figure 7.3: Unit cell for Neel AFM order. The black dots are the Cu sites with their respective spins (arrows). The blue orbitals are the O ligand 2$p_{x/y}$. The red orbitals refers to O-2p_π states transversal to the Cu-3$d_{x^2-y^2}$. [Ebrahimnejad et al., 2014]

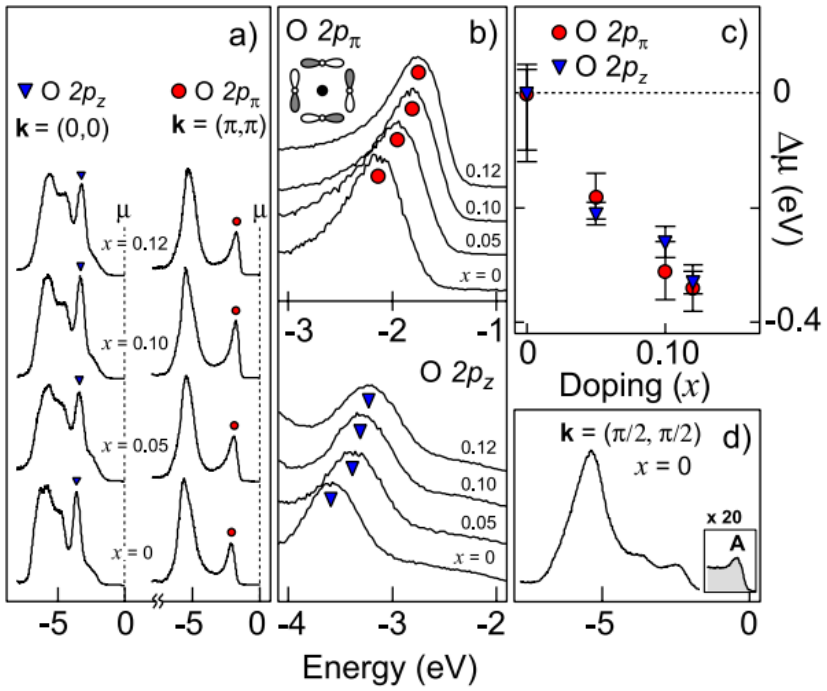

Figure 7.4: (a) Valence band spectra for $x = 0$, 0.05, 0.10, and 0.12 compositions at $\mathbf{k} = (\pi, \pi)$ and $\mathbf{k} = (0, 0)$. O-$2p_z$ and O-$2p_\pi$ states are marked by triangles and circles, respectively. (b) Shifts of the O-$2p_z$ and O-$2p_\pi$ peaks shown on an expanded scale. (c) Doping dependence of μ determined from (b). (d) Valence band at$\mathbf{k} = (\pi/2, \pi/2)$, showing the lower Hubbard band (A) on an expanded scale. [Shen et al., 2004]

7.3 *Doping and Temperature Dependence of the O-2p_π band.*

In order to reach the goal, we needed some preliminary informations on the equilibrium distribution in k-space of the O-2p_π bands and their doping and temperature evolution. For this reasons we have performed our own ARPES measurements on $Bi_2Sr_2Ca_{0.92}Y_{0.08}Cu_2O_{8+\delta}$ at the Quantum Materials Laboratory of the University of British Columbia in the group of Prof. Andrea Damascelli. To achieve an energy resolution in the sub-meV regime combined with angular resolution better than 0.1 degrees, a new prototype of electron spectrometer (SPECS 2D-Phoibos150) has been installed on an ultra- high vacuum (UHV) μ-metal chamber together with a monochromatized high-brightness ultra- violet photon source (SPECS UVS300). The photons used for these experiments was achieved using He Iα resonance line (21.218 eV) as photon source.

Figure 7.5 shows the position, in the momentum-energy distribution, of the O-2p_π band. It is very localized at 1.5 eV binding energy below E_F and it is also well localized in momentum around the Y of the Brilluoin zone at (π, π) (see Figure 7.7 where the momentum distribution at $E_B \simeq 1.5$ eV is reported). This is even more clear if we analyse the EDC's (energy distribution curve) at a fixed momentum in Figure 7.6. The three EDC's are evaluated at three different points of the Brillouin zone: $(0, 0)$, $(\pi/2, \pi/2)$ and (π, π). The intensity

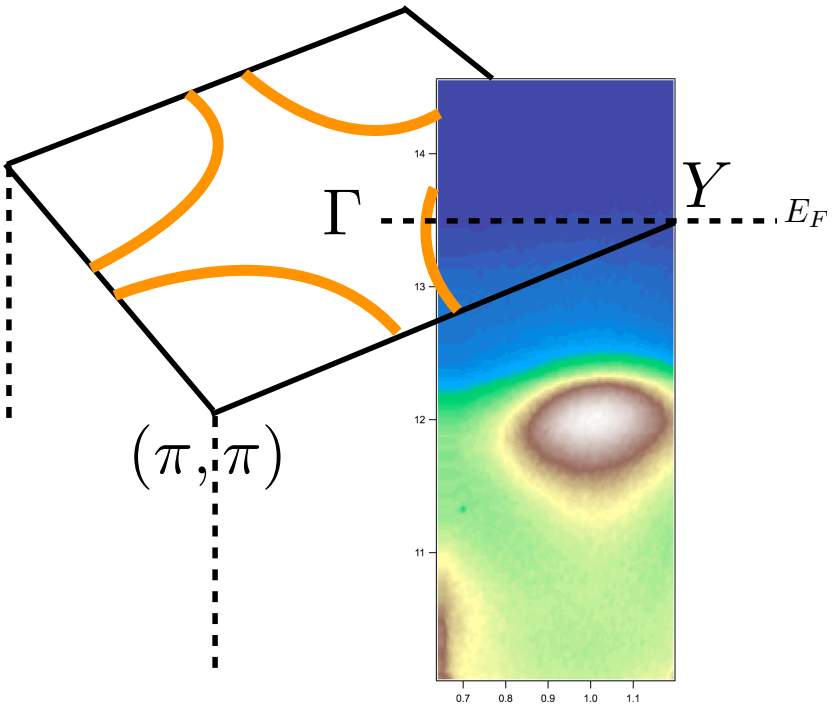

Figure 7.5: Momentum-energy ARPES measurment on $Bi_2Sr_2Ca_{0.92}Y_{0.08}Cu_2O_{8+\delta}$ in the $\Gamma \longrightarrow Y$ direction. A sketch of the Fermi surface of the first Brillouin zone at E_F is also shown.

of the O-2p_π band is localized around the (π, π) zone while it is completely absent in other zones.

The temperature evolution of the peak of the O-2p_π band is displayed in Figure 7.8. To evaluate the differences between the two measurements at 30 K and 110 K we have fitted the peaks with an exponentially modified Gaussian distribution to take into account the asymmetry of the peak. The fitting function writes:

$$f(x, x_0, w, A, \tau) = \frac{A}{\tau} \exp\left(\frac{1}{2}\left(\frac{w}{\tau}\right)^2 - \frac{x - x_0}{\tau}\right)\left(\frac{1}{2} - \frac{1}{2}\mathrm{erf}\left(\frac{1}{\sqrt{2}}\left(\frac{x - x_0}{w} - \frac{w}{\tau}\right)\right)\right) \quad (7.1)$$

where x_0 is the peak position, w is the width of the gaussian, A is its intensity and τ is the decay rate of the exponential, responsible for the asymmetry. The results of the fit show that heating the sample, the O-2p_π band shifts towards lower binding energy with a $\Delta E_B \simeq 80$meV. Also the width of the peak is affected by the temperature, it increases from 0.170 eV at 30K to 0.189 eV at 200K.
In Figure 7.9 we have reported the doping evolution of the O-2p_π band. It is possible to see that, with a larger doping level the peak of the band is shifted towards the Fermi energy. This behaviour is in agreement with the doping behaviour of the same band already discussed in Figure 7.4 [Shen et al., 2004]. So, with these preliminary ARPES measurements at equilibrium, we have demonstrated that

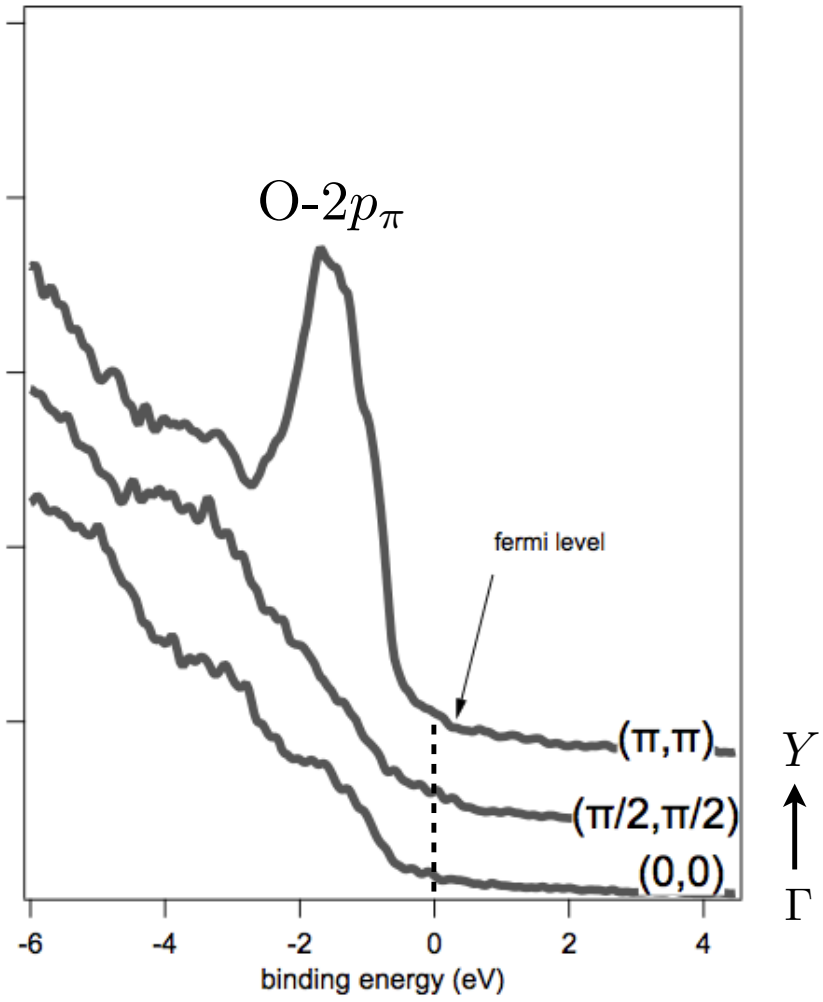

Figure 7.6: EDC curves that show the density of the states at three different parts of the Brillouin zone: $(0,0)$, $(\pi/2,\pi/2)$, (π,π).

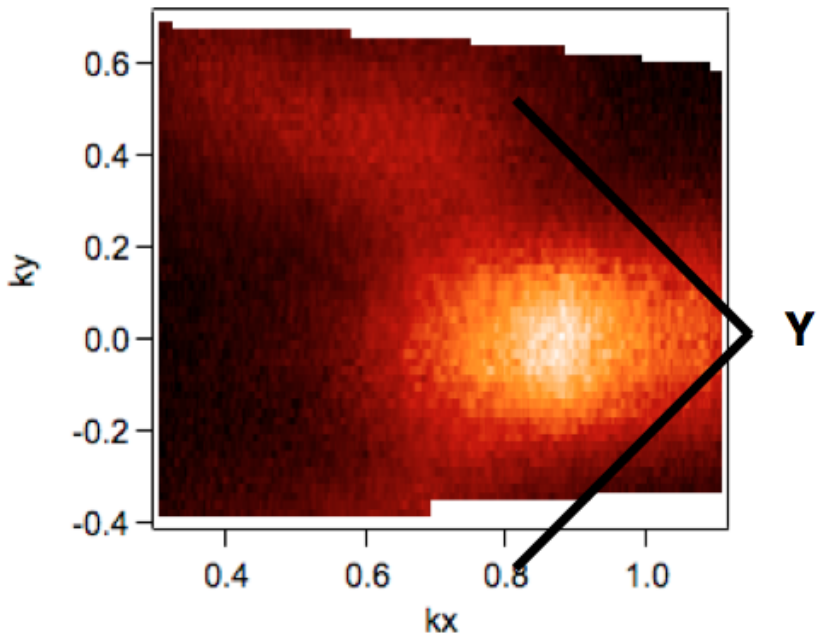

Figure 7.7: ARPES state distribution around the Y zone (π, π) at 1.5 eV binding energy below the E_F. The density of state of the O-2p_π is very localized in momentum.

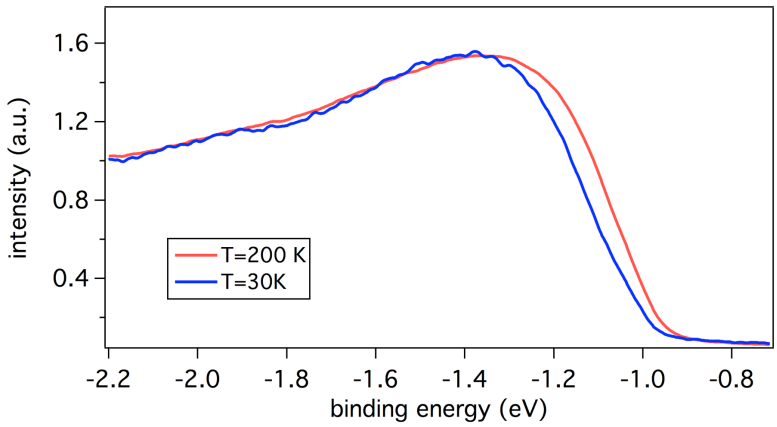

Figure 7.8: Temperature dependence of the O-2p_π band in UD Y-Bi2212. Heating the sample from 30K (blue) to 200K(red)

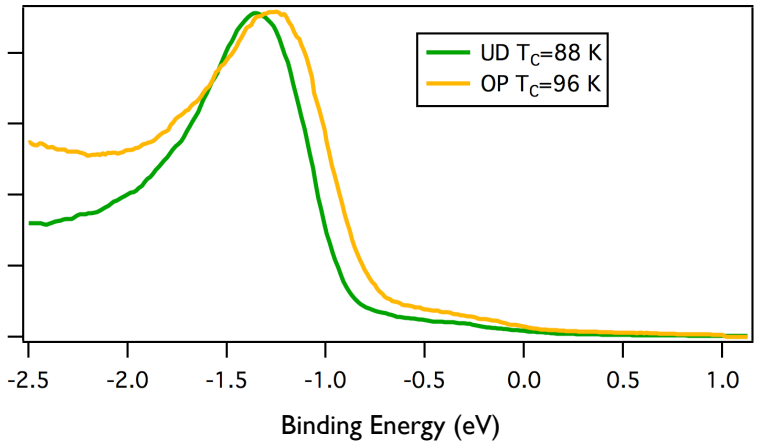

Figure 7.9: Doping dependence of the O-2p_π band in Y-Bi2212. The peak in the optimally doped sample (yellow) is shifted towards E_F in respect to the under doped sample (green)

the phototemission spectrum of the Bi2212 is characterized by the presence of an intense band localized at the (π, π) position of the Brillouin zone. We have already seen that this band is probably due to the O-2p_π orbitals of the CuO planes.

7.4 *Time-Resolved ARPES Measurements*

Time-resolved ARPES measurements have been performed at the ARTEMIS facility in the Central Laser Facilities of Oxford Harwell. The laser beamline ARTEMIS provides XUV probe light tunable to about 20 eV to exactly reproduce the experimental conditions of the ARPES experiments already performed on these samples (for a detailed description of the ARTEMIS setup see 5.3). While the pump intensity should be tuned down to the low fluence regime (about 100 μJ/cm^2), to avoid the impulsive destruction of the superconducting phase [Giannetti et al., 2009], the very high photoemission signal of the 1.5-3 eV bands, as compared to the conduction band, has allowed to perform measurements with a very good signal- to-noise ratio. The temporal resolution of ARTEMIS is . In particular, in this experiment, we have used a probe beam of and a pump beam with 790 nm wavelength with a pump fluence of $\sim 350\mu$J/cm^2.

In Figure 7.10 we have reported the photoemission spectrum (kinetic energy vs momentum) of the O-2p_π band at equilibrium together with three other panels that represent the difference between the pumped spectrum and the one at equilibrium for different delays. Panel b) shows the differential analysis at negative time $t = -150$ and has to be taken as the reference. The sample is at equilibrium and the spectrum is constantly zero. The position of the Fermi energy

($E_B = 0$ eV) and the O-2p_π band ($E_B \simeq -1.5$ eV) is highlighted. Once the pump has come at $t = 0$ (panel c) we can appreciate two different effects: 1) the density of states at the Fermi energy is increased; 2) the band at $E_B \simeq -1.5$ eV have been modified giving origin to a positive variation above the center of the band peak and a negative variation below. The latter effect could be due to a broadening of the band peak or to a modification of its equilibrium position. We will analyse in detail this aspect later in the section. After 2 ps the equilibrium density of state at E_F is recovered while the O-2p_π band presents a decreased intensity of the density of states. Note that this variation is completely different from the variation at $t = 0$. The informations that we get from these data are that the dynamics of the conduction band at E_F is completely different from the dynamics of the O-2p_π. This latter band presents a positive variation that has a faster dynamics than the negative one.

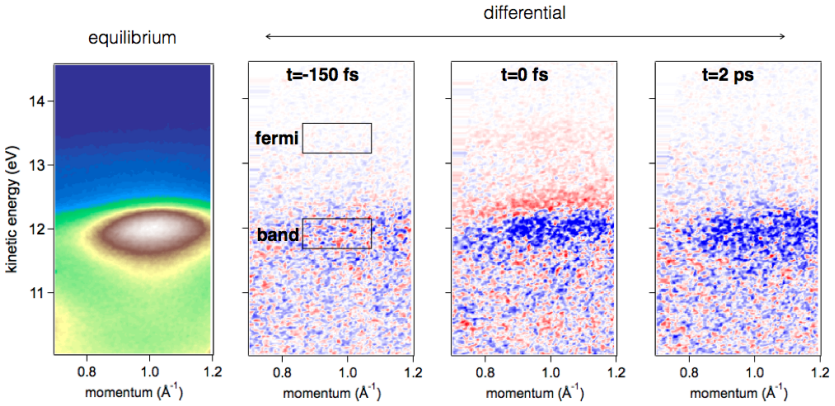

Figure 7.10: Energy-momentum distribution along (π, π) direction of the Brillouin zone. The brown intensity refers to the O-2p_π band with 1.5 eV binding energy. Panel b), c), and d) are differential spectra, referring to the equilibrium one, at three different delays: $t = -0.15$ ps, $t = 0$, $t = 2$ ps respectively.

7·5 *Data Analysis*

As a first step we focus on the states at the Fermi level. We have integrated the photoemission signal, which is proportional to the occupation of the states, over a region confined in the black rectangle labelled "fermi" in Figure 7.10, and we have reported its evolution in Figure 7.11. This evolution can be described by a double exponential decay described by the fast decay time $\tau = 130$fs and a second longer decay time of 2 ps that can be neglect within the error bars. The effect of the pump excitation can be interpreted as a photodoping that transiently increases the occupation of the states close to E_F. This transient photodoping is absorbed on a time scale compatible with the typical relaxation due to the electron-phonon coupling [Dal Conte et al., 2012].

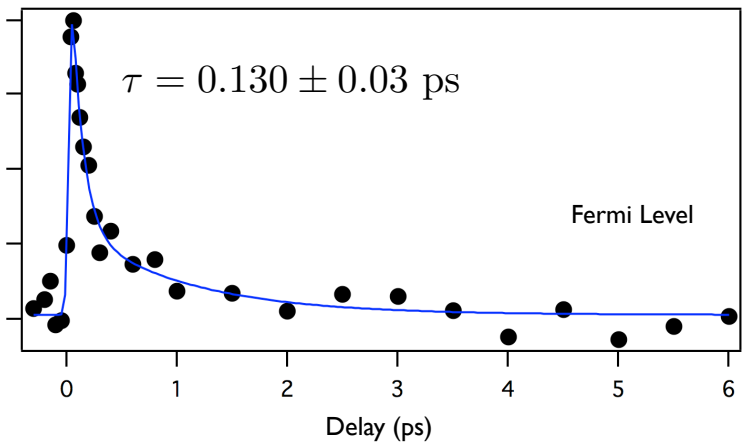

Figure 7.11: Evolution of the density of states integrated over a region confined at the Fermi energy. The region of the integration is highlighted by a black rectangle in Figure 7.10. The solid red line is the best fit of the data.

We now focus on the effect of the pump on the O-2p_π band. Starting from the equilibrium fit of the peak at -1.5 eV energy with Formula 7.1 we want to find what is the effect of the pump on the parameters of such function. The effect could be a depletion of the intensity A, a broadening of the width w, a movement of the central position x_0 or a combination of them. The idea is to fit the differential EDCs (we have chosen a slice of the differential spectra at momentum $k = 1.0\text{Å}^{-1}$) slightly changing the equilibrium parameters of the peak that describes the O-2p_π band, for different delays. In Figure 7.12 we have reported the differential EDC at $t = 0$ (a) and $t = 5.2$ ps (b) together with their best fit. It comes out that at very short delay ($t < 1$ ps) the best fit is obtained by a combination of a depletion and a broadening. The broadening is necessary to fit the positive peak at around $E_B = -0.8$ eV. On the contrary, for very long delays, the residual negative variation can be fitted only with a reduction of the intensity of the O-2p_π. In Table 7.1 the values of the parameters of the O-2p_π peak at equilibrium, $t = 0$ and $t = 5.2$ ps are reported.

Delay (ps)	Peak Pos. (eV)	Peak Int. $\times 10^6$	Peak Width (eV)
Equilibrium	12.240	3.47	0.174
$t = 0$	12.240	3.27	0.183
$t = 5.2$	12.240	3.39	0.174

Table 7.1: Position, intensity and width of the peak that describes the O-2p_π band.

From this first analysis we can say that the effect of the pump on the O-2p_π band has two main characteristics (depletion and broadening) with a very different dynamics. Performing the same differential analysis for each delay measured, we can have a comprehensive scenario of the dynamics of the A and w parameters that describe the peak of the O-2p_π band. In Figure 7.13 we have reported the differential EDCs for each delay measured together with the best fit. The fit

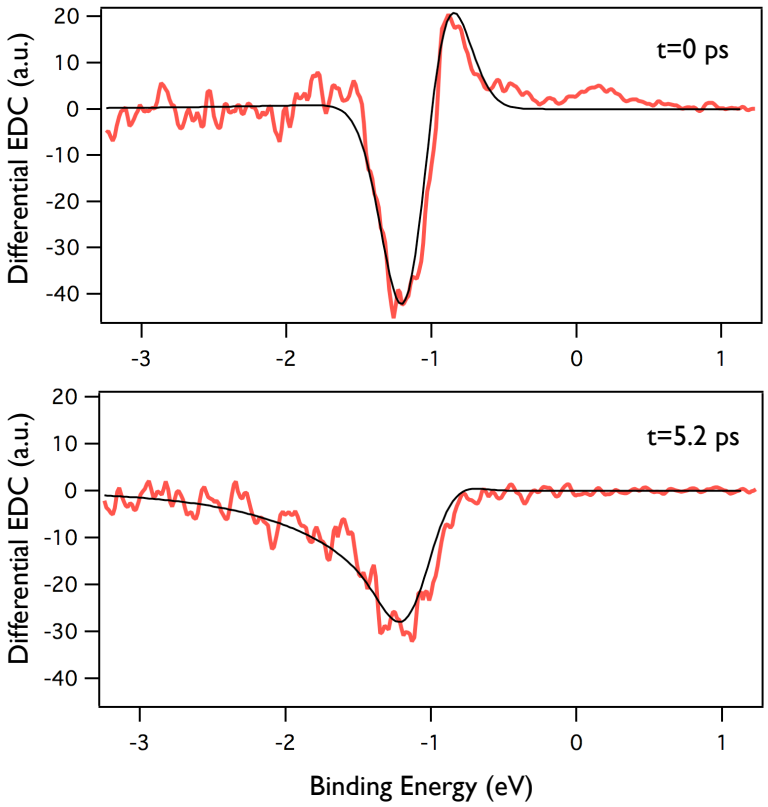

Figure 7.12: Differential EDC at $t = 0$ (a) and $t = 5.2$ ps (b) together with the best fit (black line) obtained changing a) the width and the intensity of the peak; b) the intensity of the peak.

is obtained leaving the parameters A and w free. The results of the fit are reported in Figure 7.14. The panel b) shows the evolution of the spectral weight of the peak of the O-2p_π band. The effect of the pump is to reduce the intensity of the peak. This reduction, has two clear dynamics. The first dynamics has a decay time of 150 ± 40 fs and, within the error bar, is compatible with the dynamics of the transient photodoping at E_F. Again, this relaxation is compatible with the electron-phonon coupling. The second dynamics has a very long decay time that, in the time window investigated, leads to a constant reduction of the spectral weight up to 6 ps.

Looking at the evolution of the parameter that describe the width of the peak (panel a) of Figure 7.14), we can see that the effect of the pump is to broaden the peak. This effect has a relaxation described by a single exponential with a decay time of 120 fs. This decay time is compatible with an energy dissipation due to the electron-phonon coupling and again, within the error bar, has the same dynamics than that of the transient photodoping.

So far we have seen that the dynamics of the transient filling of the states at E_F is the same than the broadening of the O-2p_π band. These three behaviours are most likely related to the same physical effect. We will try to give a detailed explanation of that in the next section. The most important evidence from the experimental data is that the spectral weight of the O-2p_π band follows a completely different dynamics, therefore it is governed by a different physical mechanism. When the broadening of the peak and the transient photodoping are completely relaxed to the equilibrium, there is still a variation of the differential spectrum which can be attribute to a net decrease of the spectral weight of the O-2p_π band.

7.6 *Discussion and Conclusions*

The experimental data reported in the previous section can be rationalized along the following lines: the 1.5 eV pump is able to excite the electrons from the O-2p_π band up to the conduction band at E_F. This effect can be considered as a transient photodoping which results in a transient occupation of the empty states at E_F and a transient depletion of the occupied O-2p_π band. The transient non-thermal population photoexcited in the conduction band rapidly relaxes by exchanging energy with the unexcited electrons and with the bosonic (spin-fluctuations and phonons) bath. In this picture, the transient photodoping is accompanied by the broadening (see Figure 7.8) of the profile of the peak attributed to the O-2p_π band, as a consequence of the increase of the scattering processes.

The most interesting and unexpected result, however, is related to

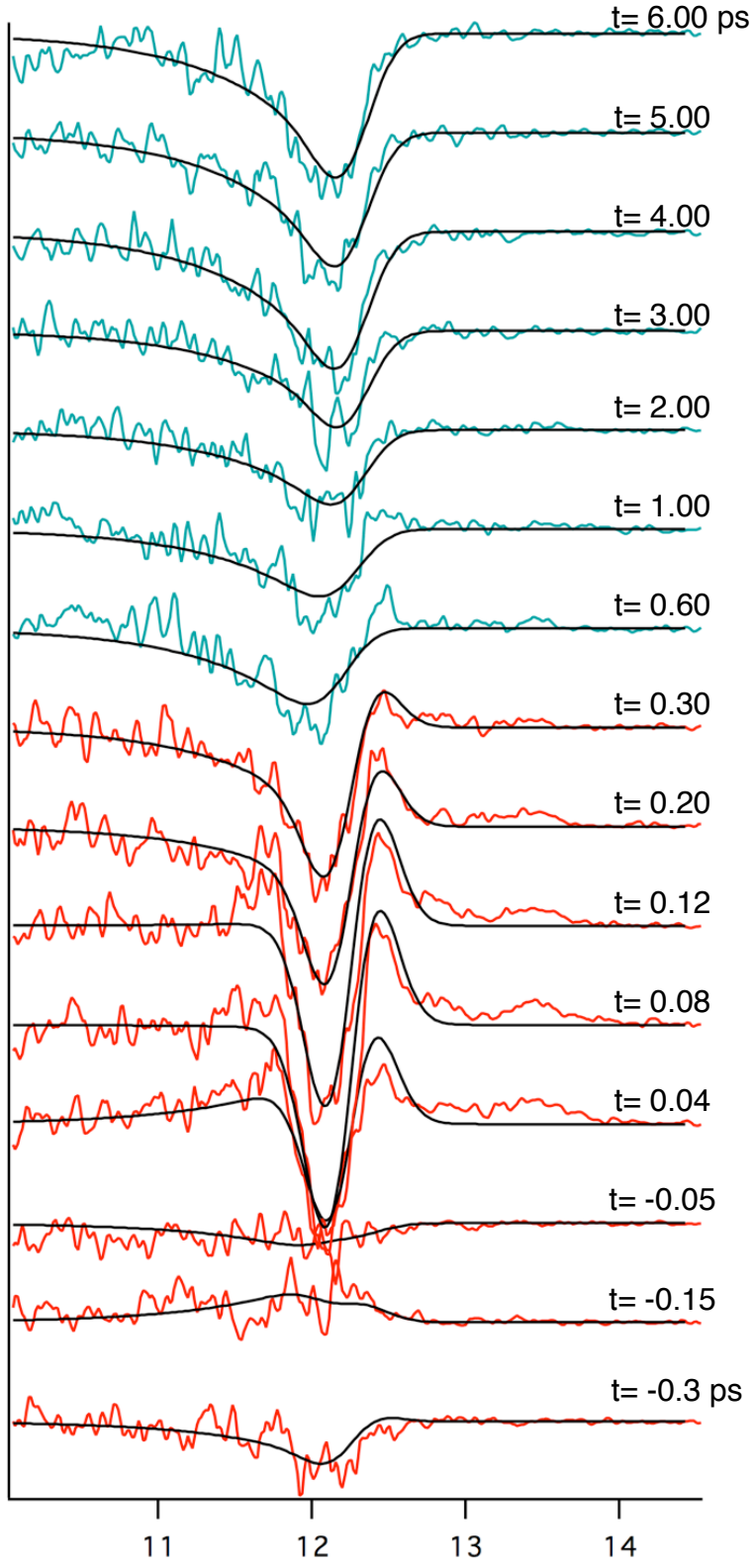

Figure 7.13: EDCs, like in Figure 7.12, at some of the delays mesured together with their best fit. The green curves are fitted using, as the only free parameter, the intensity of the peak.

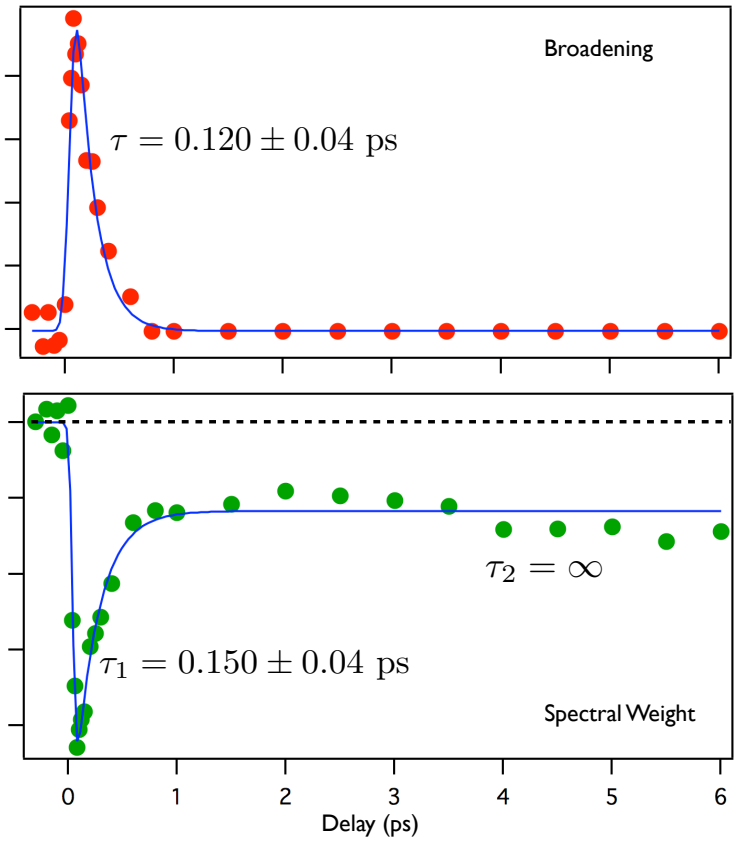

Figure 7.14: Evolution of the peak width (a) and intensity (b) used to obtain the best fit to the EDCs in Figure 7.13.

the dynamics of O-2p_π band which relaxes towards the equilibrium with a rather dynamics. In particular, the spectral weight of the O-2p_π band does not relaxes back to the equilibrium value after the relaxation of the photoexcited non-thermal electron distribution (see Figure 7.14). In order to understand this behaviour, we have to consider the three-band Hubbard model and the interaction of the holes with the antiferromagnetic background. For simplicity, we start discussing the case of the insulator in which a single hole is added. The CuO_2 plane responsible for the electronic structure of the cuprates is formed by one Cu atom and two O atoms, thus involving three orbitals (see Figure 7.15 panel a). The oxygen orbitals shown have the σ character, meaning that they are bonding with the Cu orbitals. Each of these orbitals hosts a particle with a spin. Double occupancy on the Cu sites is forbidden because of the large on-site Hubbard repulsion, so there is a spin-1/2 at each Cu site and the doping hole enters the O2p ligand. If there is the possibility for the holes to hop on the nearest neighbours, this hopping could lead to a spin-flip excitation called *magnon* (see panel b) of Figure 7.15). At this point the antiferromagnetic configuration of the unit cell consists in two Cu atoms and four oxygen orbitals with σ character (Figure 7.15 c)). In a completely paramagnetic system, the possibility for the spins to swap does not affect the dispersion of the quasiparticles. On the contrary, in an antiferromagnetically oredered system, a spin flip costs an energy of 2J, that is the energy needed to introduce a defect in the AFM ordering. It has been proved in [Ebrahimnejad et al., 2014] that, in an antiferromagnetic system, the possibility for the spins to swap reduces the bandwidth of the conduction band because the quasiparticles have a reduced mobility being the hooping not energetically favourable (Figure 7.16).

Starting from such a model, we focused on the oxygen orbitals with the π character. It is possible to add such orbitals in the model leading to a five-band Hubbard model. The picture is sketched in the panel d) of Figure 7.15. The red orbitals are the O-2p_π orbitals non bonding with the Cu. Starting from the Hamiltonian of this model and defining Green's functions it is possible to generate and solve their exact equations of motion. From the calculations for the band dispersions of the five-band Hubbard model it turns out that, including the O-2p_π orbitals, a prominent band at 1.5 eV binding energy arises (see Figure 7.17). Thanks to the projection of such band on the different orbitals we can extract the real character of the band. It comes out that at the (π, π) point of the Brillouin zone the band at 1.5 eV binding energy is completely related to the O-2p_π orbitals with a negligible hybridization with the binding oxygen orbitals O-2p_σ. Furthermore, the O-2p_π orbitals are not hybridized with the

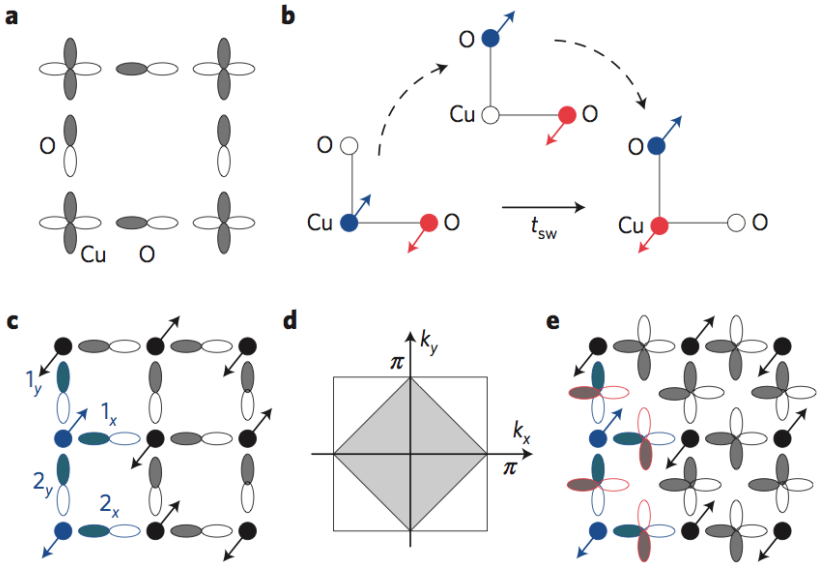

Figure 7.15: a) Cu3$d_{x^2-y^2}$ and the O ligand $2p_{x/y}$ orbitals included in the three-band model. b) Sketch of a spin-swap process that results in hopping of the hole while its spin is swapped with that of the neighbour Cu. c) Unit cell for Neel AFM order, consisting of two Cu spins and four O orbitals (highlighted in blue). d) Magnetic Brillouin zone (shaded area) in the first Brillouin zone. e) Unit cell for Neel AFM order in the five-band model. The additional O orbitals are highlighted in red. [Ebrahimnejad et al., 2014]

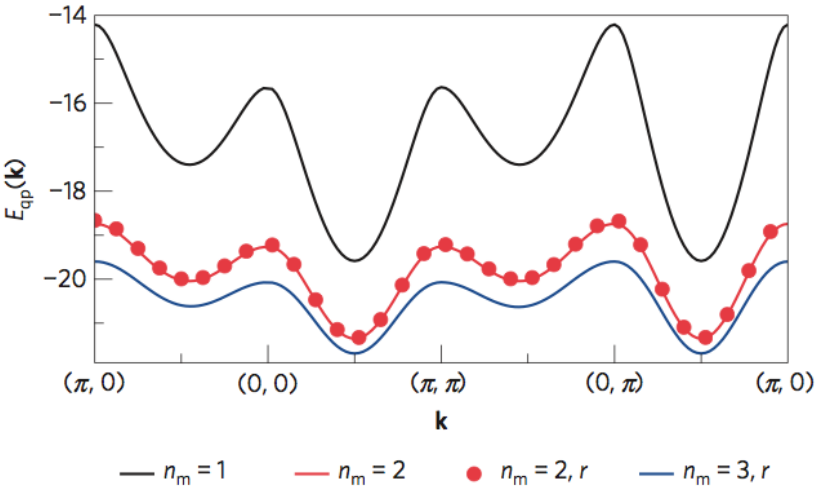

Figure 7.16: Quasiparticle energy (in units of J_{dd}) along various cuts in the Brillouin zone. The results are for the three-band model using $n_m = 1$ (black line), $n_m = 2$ (red line), restricted $n_m = 2$ (red circles) and restricted $n_m = 3$ (blue line) approximations.

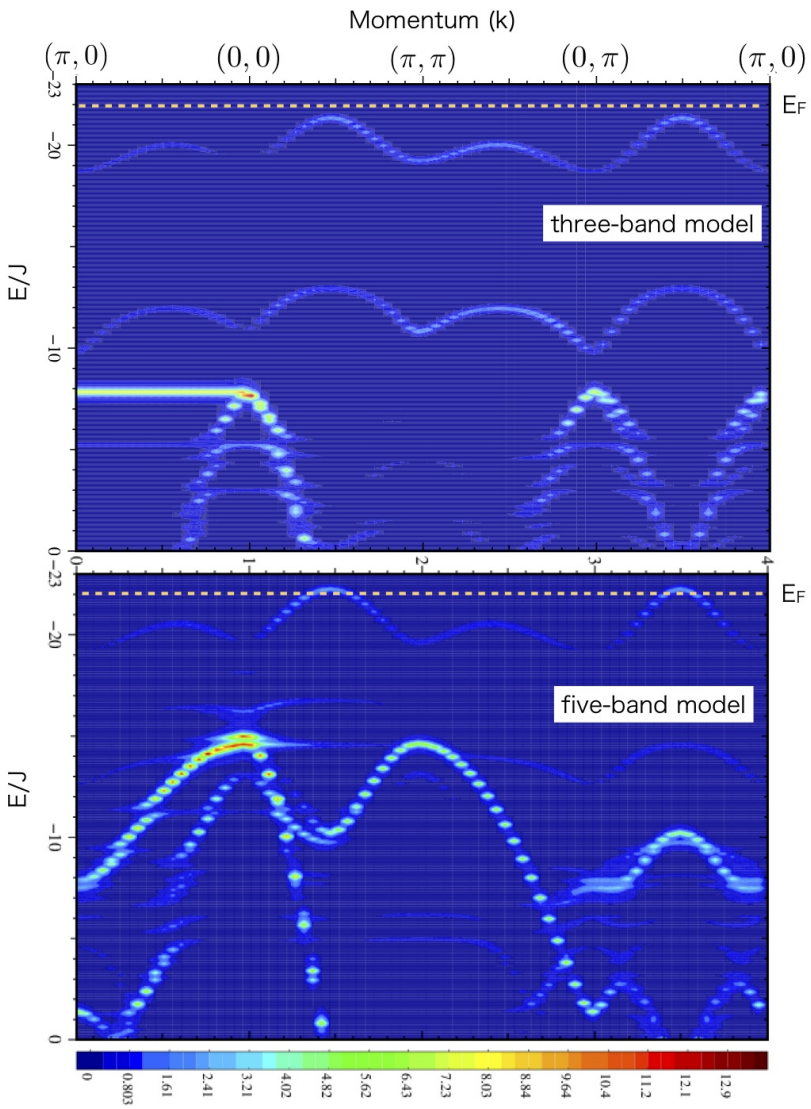

Figure 7.17: Calculated band distributions as a function of the energy and momentum. The energy is in J_{dd} unit. 1 J_{dd} $\sim$ 150 meV so, 10 J_{dd} $\sim$ 1.5 eV. Note that the five-band model, with the addition of the O-2p_π, gives origin to a prominent band at -1.5 eV with a rather flat density of states in both the $(0,0)$ and (π,π) point of the Brillouin zone.

conduction band in contrast with the O-2p_σ (see Figure 7.6). This confirms that the band at 1.5 eV binding energy in the (π, π) position is referred to the O-2p_π orbitals.

Wrapping all these results up we can elaborate the following picture: the pump pulse with photon energy of 1.5eV is absorbed via the creation of electron-hole excitations that result in the injection of holes in the oxygen bands at about 1.5 eV binding energy and electrons in the conduction band. In principle, both the π band (at (π, π)) and the σ band (at $(0, 0)$) exhibit a rather flat density of states which lies about 1.5 eV below the E_F (see panel c) and d) of Figure 7.6). Therefore, it is reasonable to assume that the initial photoexcitation generate a hole excess in both bands. Nonetheless, the relaxation process is expected to be dramatically different of the two types of electron-hole excitations, as a consequence of the different symmetry of the orbitals involved. While the O-2p_σ band is heavily hybridized with the Cu atoms and is strongly affected by the AF background (compare panel a) and c) of Figure 7.6), the O-2p_π band is almost completely non-bonding with the Cu3$d_{x^2-y^2}$ orbitals that participate to the conduction band. Therefore, while the photoexcited holes in the O-2p_σ band can rapidly relax to the conduction band via electron scattering or via the interaction with spin fluctuations or phonons, the photoexcited holes in the O-2p_π band do not have any lower-energy final state with the same symmetry where to decay to. Eventually, also the -1.5 eV holes at (π, π) will decay, as soon as a scattering process provides the momentum (π, π) necessary to elastically scatter to the O-2p_σ band and, from here, to relax to the Fermi level.

In conclusion, the present time-resolved UV photoemission data demonstrate a strong bottleneck in the relaxation of the holes photoexcited in the O-2p_π band at (π, π). This is a consequence of non-bonding nature of these states which are almost non hybridized with the Cu3$d_{x^2-y^2}$ orbitals that mainly participate to the conduction band. Furthermore, these results demonstrate that when the position in the k-space is considered, the photoexcited population has a strongly non thermal nature, characterized by an excess of holes in the O-2p_π band localized at (π, π). This result challenges the state-of-the-art models which aim at describing the relaxation dynamics in copper oxides.

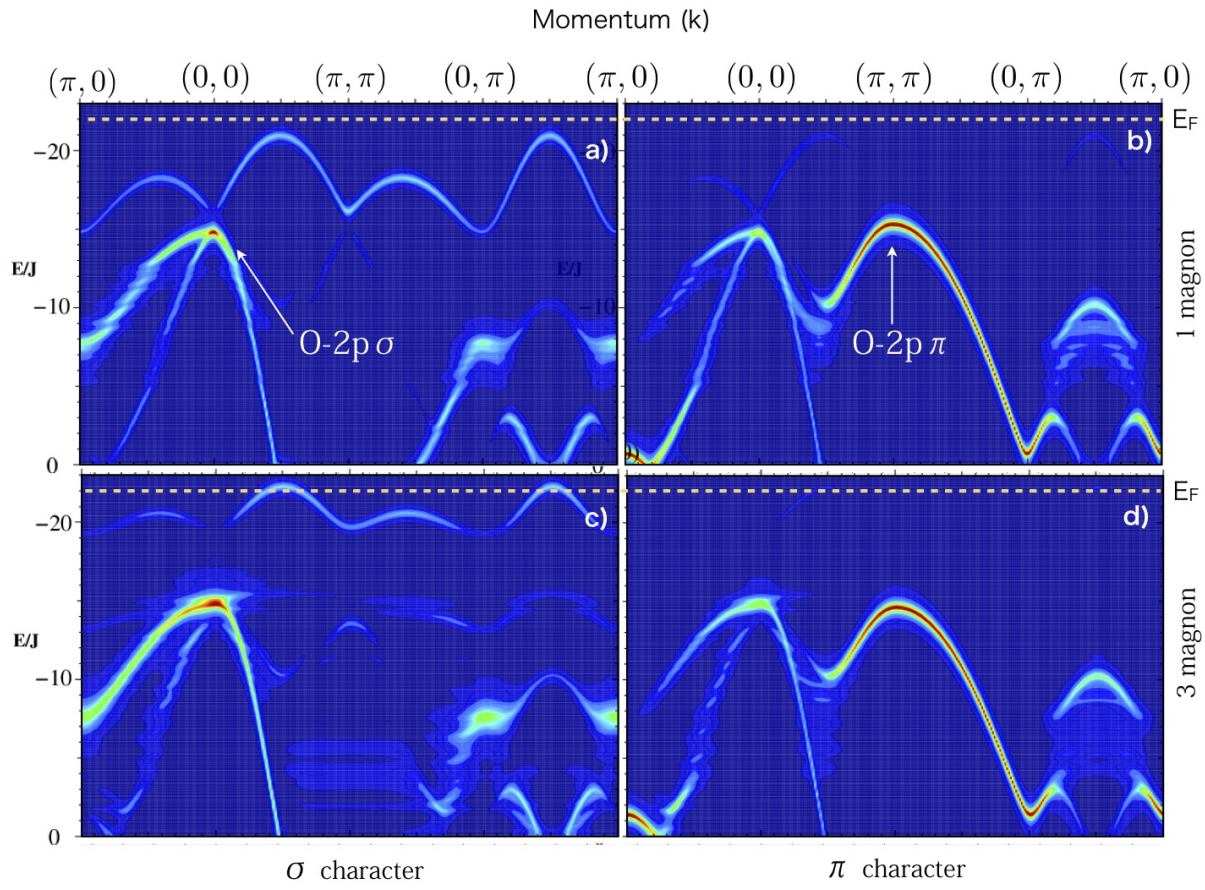

Figure 7.18: Calculated band distributions as a function of the energy and momentum. The energy is in J_{dd} unit. $1J_{dd} \sim 150$ meV so, $10\ J_{dd} \sim 1.5$ eV. The first column (panel a and c) refers to the projection of the bands on the O-2p_σ orbitals. The second column (panel b and d) refers to the π character of the bands. In the first row (panel a and b) there are calculation made with just a single magnon allowed, while in the panel c and d of the second row there are 3 magnons allowed.

8 Conclusions

In this thesis we have studied the out-of-equilibrium physics of cuprates using different techniques: broadband non-equilibrium optical spectroscopy and time-resolved laser- and XUV-ARPES. In particular we have studied $Bi_2Sr_{2-x}La_xCuO_{6+\delta}$ single-layer copper oxide (Bi2201) and $Bi_2Sr_2Ca_{0.92}Y_{0.08}Cu_2O_{8+\delta}$ double-layer copper oxide (Bi2212).

Bi2201 We have performed time-resolved optical spectroscopy experiments by exploiting the supercontinuum coherent spectrum produced by a non-linear photonic crystal fiber and the tunable pulses provided by an optical parametric amplifier system. The time and frequency resolved reflectivity measurements we report and discuss are carried out on different $Bi_2Sr_{2-x}La_xCuO_{6+\delta}$ crystals at $T = 300$ K and at six different dopings. Among the different results obtained, we cite:

- We have shown that the pump excitation (1.9 eV) induces a modification of the charge-transfer transition at >2 eV which strongly depends on the hole concentration. Starting from the equilibrium dielectric function of each sample, we have demonstrated that: 1) in the underdoped regime the pump also induces a redshift of the charge-transfer oscillator at 2 eV. 2) in the overdoped regime no shift of the charge-transfer oscillator is observed. The transient reflectivity can be well described by an increased effective electronic temperature of the system with a consequent increase of the number of bosons through which the electrons can dissipate the stored energy. 3) the transition between these two behaviours corresponds to the critical doping p_{cr} at which the amplitude of the charge ordering peak, as revealed by REXS, disappears.
- Our results unveil a strict relation between the redshift of the 2 eV oscillator at room temperature and the quantum critical point at $T = 0$. We attribute the observed redshift to the formation of local "dressed" exciton. We also argue that the value of the critical doping p_{cr} is regulated by a transition of the

electronic properties at the high energy scales, which can be already observed at high temperature. In particular the final state of the charge transfer process evolves from a correlated state, localized in the real space, to a more conventional delocalized wavefunction. Our work has pointed out the benefit of the out of equilibrium techniques which can be complementary to the conventional equilibrium approach (REXS, ARPES...) and provides many valuable informations.

Bi2212 On these sample we have performed time-resolved XUV photoemissione experiments at the ARTEMIS beamline at the Central Laser Facility (Rutherford-Appleton Laboratories, Harwell-Oxford, UK). In particular, we focused on the dynamics of the O-2p_π band, which is observed at the (π, π) point of the surface Brillouin zone. The main results can be summarized as follows:

- We have observed two components in the relaxation dynamics of this band. The first fast dynamics is due to a broadening of the O-2p_π peak and it relaxes to equilibrium in $\sim$ 130 fs. This dynamics follows the evolution of the variation of the population of the states at the Fermi level in the conduction band. The relaxation time of these two dynamics is compatible with the electron-phonon coupling. The second dynamics of the O-2p_π peak at 1.5 eV is described by a spectral weight decrease that is much slower (6 ps) and completely decoupled from the fast dynamics of the conduction band.
- Our interpretation of the results is that the pump pulse with photon energy of 1.5 eV is absorbed via the creation of electron-hole excitations that result in the injection of holes in the oxygen bands at about 1.5 eV binding energy and electrons in the conduction band. The different nature of the oxygen band at 1.5 eV binding energy, with bonding (σ) and non-bonding (π) character, in relation to the conduction Cu3$d_{x^2-y^2}$ band, determines a fast and a slow decoupled dynamics. In conclusion, the present time-resolved UV photoemission data demonstrate a strong bottleneck in the relaxation of the holes photoexcited in the O-2p_π band at (π, π). Furthermore, these results demonstrate that when the position in the k-space is considered, the photoexcited population has a strongly non thermal nature, characterized by an excess of holes in the O-2p_π band localized at (π, π).

Bibliography

P. Abbamonte, A. Rusydi, S. Smadici, G. D. Gu, G. A. Sawatzky, and D. L. Feng. Spatially modulated 'mottness' in la2-xbaxcu04. *Nat Phys*, 1(3):155–158, 12 2005. URL http://dx.doi.org/10.1038/nphys178.

Elihu Abrahams, S. Schmitt-Rink, and C. M. Varma. High-tc superconductivity mediated by charge transfer excitations. *Physica B+C*, 148(1–3):257–259, 12 1987. DOI: http://dx.doi.org/10.1016/0378-4363(87)90204-X. URL http://www.sciencedirect.com/science/article/pii/037843638790204X.

A. Achkar, R. Sutarto, X. Mao, F. He, A. Frano, S. Blanco-Canosa, M. Le Tacon, G. Ghiringhelli, L. Braicovich, M. Minola, M. Moretti Sala, C. Mazzoli, Ruixing Liang, D. Bonn, W. Hardy, B. Keimer, G. Sawatzky, and D. Hawthorn. Distinct charge orders in the planes and chains of ortho-iii-ordered $yba_2cu_3\mathbf{o}_{6+\delta}$ superconductors identified by resonant elastic x-ray scattering. *Phys. Rev. Lett.*, 109: 167001, Oct 2012. DOI: 10.1103/PhysRevLett.109.167001. URL http://link.aps.org/doi/10.1103/PhysRevLett.109.167001.

P. B. Allen. Electron-phonon effects in the infrared properties of metals. *Phys. Rev. B*, 3:305–320, Jan 1971. DOI: 10.1103/PhysRevB.3.305. URL http://link.aps.org/doi/10.1103/PhysRevB.3.305.

P. W. Anderson. The resonating valence bond state in la2cu04 and superconductivity. *Science*, 235(4793):1196–1198, 1987. DOI: 10.1126/science.235.4793.1196. URL http://www.sciencemag.org/content/235/4793/1196.abstract.

E. Antonides, E. C. Janse, and G. A. Sawatzky. LMM auger spectra of Cu, Zn, Ga and Ge. transition probabilities, term splittings, and effective coulomb interaction. *Phys. Rev. B*, 15:1669–1679, Feb 1977. DOI: 10.1103/PhysRevB.15.1669. URL http://link.aps.org/doi/10.1103/PhysRevB.15.1669.

H. Anzai, A. Ino, M. Arita, H. Namatame, M. Taniguchi, M. Ishikado, K. Fujita, S. Ishida, and S. Uchida. Relation be-

tween the nodal and antinodal gap and critical temperature in superconducting bi2212. *Nat Commun*, 4:1815, 05 2013. URL http://dx.doi.org/10.1038/ncomms2805.

Backus. High power ultrafast lasers. *Review of Scientific Instruments*, 69(1207), 1998.

Andrius Baltuška, Takao Fuji, and Takayoshi Kobayashi. Visible pulse compression to 4 fs by optical parametric amplification and programmable dispersion control. *Opt. Lett.*, 27(5):306–308, Mar 2002. DOI: 10.1364/OL.27.000306. URL http://ol.osa.org/abstract.cfm?URI=ol-27-5-306.

J. Bardeen, L. N. Cooper, and J. R. Schrieffer. Microscopic theory of superconductivity. *Phys. Rev.*, 106:162–164, Apr 1957. DOI: 10.1103/PhysRev.106.162. URL http://link.aps.org/doi/10.1103/PhysRev.106.162.

Neven Barisic, Sven Badoux, Mun K. Chan, Chelsey Dorow, Wojciech Tabis, Baptiste Vignolle, Guichuan Yu, Jerome Beard, Xudong Zhao, Cyril Proust, and Martin Greven. Universal quantum oscillations in the underdoped cuprate superconductors. *Nat Phys*, 9(12):761–764, 12 2013. URL http://dx.doi.org/10.1038/nphys2792.

D. N. Basov and T. Timusk. Electrodynamics of high-T_c superconductors. *Rev. Mod. Phys.*, 77:721–779, Aug 2005. DOI: 10.1103/RevModPhys.77.721. URL http://link.aps.org/doi/10.1103/RevModPhys.77.721.

Richard A. Baumgartner and R. Byer. Optical parametric amplification. *Quantum Electronics, IEEE Journal of*, 15(6):432–444, Jun 1979. ISSN 0018-9197. DOI: 10.1109/JQE.1979.1070043.

J. G. Bednorz and K. A. Müller. Possible high T_c superconductivity in the Ba-La-Cu-O system. *Zeitschrift fur Physik B Condensed Matter*, 64:189–193, June 1986. DOI: 10.1007/BF01303701.

J. G. Bednorz, M. Takashige, and K. A. M?ller. Susceptibility measurements support high- t c superconductivity in the ba-la-cu-o system. *EPL (Europhysics Letters)*, 3(3):379, 1987. URL http://stacks.iop.org/0295-5075/3/i=3/a=021.

J. Georg Bednorz and K. Alex Müller. Perovskite-type oxides—the new approach to high-T_c superconductivity. *Rev. Mod. Phys.*, 60:585–600, Jul 1988. DOI: 10.1103/RevModPhys.60.585. URL http://link.aps.org/doi/10.1103/RevModPhys.60.585.

J.G. Bednorz and K.A. Müller. *Earlier and recent aspects of superconductivity: lectures from the International School, Erice, Trapani, Sicily, July 4-16, 1989*. Springer series in solid-state sciences. Springer, 1990. ISBN 9783540521563. URL http://books.google.co.uk/books?id=mh6aAAAAIAAJ.

H. Bethe. Theorie der beugung von elektronen an kristallen. *Annalen der Physik*, 392(17):55–129, 1928. ISSN 1521-3889. DOI: 10.1002/andp.19283921704. URL http://dx.doi.org/10.1002/andp.19283921704.

R.W. Boyd. *Nonlinear Optics*. Electronics & Electrical. Academic Press, 2003. ISBN 9780121216825. URL http://books.google.it/books?id=30t9VmOmOGsC.

N. B. Brookes, G. Ghiringhelli, O. Tjernberg, L. H. Tjeng, T. Mizokawa, T. W. Li, and A. A. Menovsky. Detection of zhang-rice singlets using spin-polarized photoemission. *Phys. Rev. Lett.*, 87: 237003, Nov 2001. DOI: 10.1103/PhysRevLett.87.237003. URL http://link.aps.org/doi/10.1103/PhysRevLett.87.237003.

C. Castellani, C. Di Castro, and W. Metzner. Dimensional crossover from fermi to luttinger liquid. *Phys. Rev. Lett.*, 72:316–319, Jan 1994. DOI: 10.1103/PhysRevLett.72.316. URL http://link.aps.org/doi/10.1103/PhysRevLett.72.316.

G. Cerullo, M. Nisoli, S. Stagira, and S. De Silvestri. Sub-8-fs pulses from an ultrabroadband optical parametric amplifier in the visible. *Opt. Lett.*, 23(16):1283–1285, Aug 1998. DOI: 10.1364/OL.23.001283. URL http://ol.osa.org/abstract.cfm?URI=ol-23-16-1283.

G. Cerullo, M. Nisoli, S. Stagira, S. De Silvestri, G. Tempea, F. Krausz, and K. Ferencz. Mirror-dispersion-controlled sub-10-fs optical parametric amplifier in the visible. *Opt. Lett.*, 24 (21):1529–1531, Nov 1999. DOI: 10.1364/OL.24.001529. URL http://ol.osa.org/abstract.cfm?URI=ol-24-21-1529.

Giulio Cerullo. Ultrafast optical parametric amplifiers. *Review of Scientific Instruments*, 74(1), 2003.

J. Chang, E. Blackburn, A. T. Holmes, N. B. Christensen, J. Larsen, J. Mesot, Ruixing Liang, D. A. Bonn, W. N. Hardy, A. Watenphul, M. v. Zimmermann, E. M. Forgan, and S. M. Hayden. Direct observation of competition between superconductivity and charge density wave order in yba2cu3o6.67. *Nat Phys*, 8(12):871–876, 12 2012. URL http://dx.doi.org/10.1038/nphys2456.

Z Chen, Y Y Peng, Z Wang, Y J Song, J Q Meng, X J Zhou, and J Q Li. Compositional evolution of the anti-phase stripe superstructure in $Bi_2Sr_{2-x}La_xCuO_{6+\delta}$ revealed by transmission electron microscopy. *Superconductor Science and Technology*, 26(5):055010, 2013. URL http://stacks.iop.org/0953-2048/26/i=5/a=055010.

T. R. Chien, Z. Z. Wang, and N. P. Ong. Effect of zn impurities on the normal-state hall angle in single-crystal $yba_2cu_{3-x}zn_xo_{7-ffi}$, url = http://link.aps.org/doi/10.1103/PhysRevLett.67.2088, volume = 67, year = 1991, bdsk-url-1 = http://link.aps.org/doi/10.1103/PhysRevLett.67.2088, bdsk-url-2 = http://dx.doi.org/10.1103/PhysRevLett.67.2088. *Phys. Rev. Lett.*, pages 2088–2091, Oct . DOI: 10.1103/PhysRevLett.67.2088.

Federico Cilento, Claudio Giannetti, Gabriele Ferrini, Stefano Dal Conte, Tommaso Sala, Giacomo Coslovich, Matteo Rini, Andrea Cavalleri, and Fulvio Parmigiani. Ultrafast insulator-to-metal phase transition as a switch to measure the spectrogram of a supercontinuum light pulse. *Applied Physics Letters*, 96(2):–, 2010. URL http://scitation.aip.org/content/aip/journal/apl/96/2/10.1063/1.3291105.

G. Cirmi, D. Brida, C. Manzoni, M. Marangoni, S. De Silvestri, and G. Cerullo. Few-optical-cycle pulses in the near-infrared from a noncollinear optical parametric amplifier. *Opt. Lett.*, 32 (16):2396–2398, Aug 2007. DOI: 10.1364/OL.32.002396. URL http://ol.osa.org/abstract.cfm?URI=ol-32-16-2396.

R. Comin, G. Levy, B. Ludbrook, Z.-H. Zhu, C. N. Veenstra, J. A. Rosen, Yogesh Singh, P. Gegenwart, D. Stricker, J. N. Hancock, D. van der Marel, I. S. Elfimov, and A. Damascelli. na_2iro_3. *Phys. Rev. Lett.*, 109:266406, Dec 2012. DOI: 10.1103/PhysRevLett.109.266406. URL http://link.aps.org/doi/10.1103/PhysRevLett.109.266406.

R. Comin, A. Frano, M. M. Yee, Y. Yoshida, H. Eisaki, E. Schierle, E. Weschke, R. Sutarto, F. He, A. Soumyanarayanan, Yang He, M. Le Tacon, I. S. Elfimov, Jennifer E. Hoffman, G. A. Sawatzky, B. Keimer, and A. Damascelli. Charge order driven by fermi-arc instability in $Bi_2Sr_{2-x}La_xCuO_{6+\delta}$. *Science*, 343(6169):390–392, 2014. DOI: 10.1126/science.1242996. URL http://www.sciencemag.org/content/343/6169/390.abstract.

S. Dal Conte. Snapshots of the retarded interaction of charge carriers with ultrafast fluctuations in cuprates. *Nature Physics*, Accepted not published, 2014.

M. K. Crawford, M. A. Subramanian, R. L. Harlow, J. A. Fernandez-Baca, Z. R. Wang, and D. C. Johnston. Structural and magnetic studies of sr_2iro_4. *Phys. Rev. B*, 49:9198–9201, Apr 1994. DOI: 10.1103/PhysRevB.49.9198. URL http://link.aps.org/doi/10.1103/PhysRevB.49.9198.

Eduardo H. da Silva Neto, Pegor Aynajian, Alex Frano, Riccardo Comin, Enrico Schierle, Eugen Weschke, András Gyenis, Jinsheng Wen, John Schneeloch, Zhijun Xu, Shimpei Ono, Genda Gu, Mathieu Le Tacon, and Ali Yazdani. Ubiquitous interplay between charge ordering and high-temperature superconductivity in cuprates. *Science*, 343(6169):393–396, 01 2014. URL http://www.sciencemag.org/content/343/6169/393.abstract.

Elbio Dagotto. Correlated electrons in high-temperature superconductors. *Rev. Mod. Phys.*, 66:763–840, Jul 1994. DOI: 10.1103/RevModPhys.66.763. URL http://link.aps.org/doi/10.1103/RevModPhys.66.763.

T. Dahm, V. Hinkov, S. V. Borisenko, A. A. Kordyuk, V. B. Zabolotnyy, J. Fink, B. Buchner, D. J. Scalapino, W. Hanke, and B. Keimer. Strength of the spin-fluctuation-mediated pairing interaction in a high-temperature superconductor. *Nat Phys*, 5(3):217–221, 03 2009. URL http://dx.doi.org/10.1038/nphys1180.

S. Dal Conte, C. Giannetti, G. Coslovich, F. Cilento, D. Bossini, T. Abebaw, F. Banfi, G. Ferrini, H. Eisaki, M. Greven, A. Damascelli, D. van der Marel, and F. Parmigiani. Disentangling the electronic and phononic glue in a high-tc superconductor. *Science*, 335(6076):1600–1603, 03 2012. URL http://www.sciencemag.org/content/335/6076/1600.abstract.

Andrea Damascelli, Zahid Hussain, and Zhi-Xun Shen. Angle-resolved photoemission studies of the cuprate superconductors. *Rev. Mod. Phys.*, 75:473–541, Apr 2003. DOI: 10.1103/RevModPhys.75.473. URL http://link.aps.org/doi/10.1103/RevModPhys.75.473.

Luca de' Medici, Antoine Georges, and Gabriel Kotliar. Sum-rules for raman scattering off strongly correlated electron systems. *Phys. Rev. B*, 77:245128, Jun 2008. DOI: 10.1103/PhysRevB.77.245128. URL http://link.aps.org/doi/10.1103/PhysRevB.77.245128.

T. P. Devereaux, T. Cuk, Z.-X. Shen, and N. Nagaosa. Anisotropic electron-phonon interaction in the cuprates. *Phys. Rev. Lett.*, 93:117004, Sep 2004. DOI: 10.1103/PhysRevLett.93.117004. URL http://link.aps.org/doi/10.1103/PhysRevLett.93.117004.

H. Ding, T. Yokoya, J. C. Campuzano, T. Takahashi, M. Randeria, M. R. Norman, T. Mochiku, K. Kadowaki, and J. Giapintzakis. Spectroscopic evidence for a pseudogap in the normal state of underdoped high-tc superconductors. *Nature*, 382(6586):51–54, 07 1996. URL http://dx.doi.org/10.1038/382051a0.

Hadi Ebrahimnejad, George A. Sawatzky, and Mona Berciu. The dynamics of a doped hole in a cuprate is not controlled by spin fluctuations. *Nat Phys*, 10(12):951–955, 12 2014. URL http://dx.doi.org/10.1038/nphys3130.

H. Eisaki, N. Kaneko, D. L. Feng, A. Damascelli, P. K. Mang, K. M. Shen, Z.-X. Shen, and M. Greven. Effect of chemical inhomogeneity in bismuth-based copper oxide superconductors. *Phys. Rev. B*, 69:064512, Feb 2004. DOI: 10.1103/PhysRevB.69.064512. URL http://link.aps.org/doi/10.1103/PhysRevB.69.064512.

V. J. Emery. Theory of high-t_c superconductivity in oxides. *Phys. Rev. Lett.*, 58:2794–2797, Jun 1987. DOI: 10.1103/PhysRevLett.58.2794. URL http://link.aps.org/doi/10.1103/PhysRevLett.58.2794.

H. Eskes, L. H. Tjeng, and G. A. Sawatzky. Cluster-model calculation of the electronic structure of cuo: A model material for the high-T_c superconductors. *Phys. Rev. B*, 41:288–299, Jan 1990. DOI: 10.1103/PhysRevB.41.288. URL http://link.aps.org/doi/10.1103/PhysRevB.41.288.

Turcu et al. Ultrafast science and development at the artemis facility. volume 7469, pages 746902–746902–15, 2009. URL http://dx.doi.org/10.1117/12.867540.

J. P. Falck, A. Levy, M. A. Kastner, and R. J. Birgeneau. Charge-transfer spectrum and its temperature dependence in la_2cuo_4. *Phys. Rev. Lett.*, 69:1109–1112, Aug 1992. DOI: 10.1103/PhysRevLett.69.1109. URL http://link.aps.org/doi/10.1103/PhysRevLett.69.1109.

H. Y. Fan. Temperature dependence of the energy gap in semiconductors. *Phys. Rev.*, 82:900–905, Jun 1951. DOI: 10.1103/PhysRev.82.900. URL http://link.aps.org/doi/10.1103/PhysRev.82.900.

F.Bloch. Bemerkung zur elektronentheorie des ferromagnetismus und der elektrischen leitfähigkeit. *Zeitschrift für Physik*, 57(7-8):545–555, 1929.

Peter J. Feibelman and D. E. Eastman. Photoemission spectroscopy—correspondence between quantum theory and experimental phenomenology. *Phys. Rev. B*, 10:4932–4947, Dec 1974. DOI:

10.1103/PhysRevB.10.4932. URL http://link.aps.org/doi/10.1103/PhysRevB.10.4932.

R. Fernandes, A. Chubukov, J. Knolle, I. Eremin, and J. Schmalian. Preemptive nematic order, pseudogap, and orbital order in the iron pnictides. *Phys. Rev. B*, 85:024534, Jan 2012. DOI: 10.1103/PhysRevB.85.024534. URL http://link.aps.org/doi/10.1103/PhysRevB.85.024534.

D. K. Finnemore, J. E. Ostenson, S. L. Bud'ko, G. Lapertot, and P. C. Canfield. Thermodynamic and transport properties of superconducting mg$^{10}B_2$. *Phys. Rev. Lett.*, 86:2420–2422, Mar 2001. DOI: 10.1103/PhysRevLett.86.2420. URL http://link.aps.org/doi/10.1103/PhysRevLett.86.2420.

F.Mott. On the transition to metallic conduction in semiconductors. *Canadian Journal of Physics*, 34(12A):1356–1368, 1956.

F.Mott. *Metal-Insulator transitions*. London: Taylor & Francis, 1990.

K. Fujita, Chung Koo Kim, Inhee Lee, Jinho Lee, M. H. Hamidian, I. A. Firmo, S. Mukhopadhyay, H. Eisaki, S. Uchida, M. J. Lawler, E. A. Kim, and J. C. Davis. Simultaneous transitions in cuprate momentum-space topology and electronic symmetry breaking. *Science*, 344(6184):612–616, 05 2014. URL http://www.sciencemag.org/content/344/6184/612.abstract.

G. M. Gale, M. Cavallari, T. J. Driscoll, and F. Hache. Sub-20-fs tunable pulses in the visible from an 82-mhz optical parametric oscillator. *Opt. Lett.*, 20(14):1562–1564, Jul 1995. DOI: 10.1364/OL.20.001562. URL http://ol.osa.org/abstract.cfm?URI=ol-20-14-1562.

G. M. Gale, M. Cavallari, and F. Hache. Femtosecond visible optical parametric oscillator. *J. Opt. Soc. Am. B*, 15(2):702–714, Feb 1998. DOI: 10.1364/JOSAB.15.000702. URL http://josab.osa.org/abstract.cfm?URI=josab-15-2-702.

Antoine Georges, Gabriel Kotliar, Werner Krauth, and Marcelo Rozenberg. Dynamical mean-field theory of strongly correlated fermion systems and the limit of infinite dimensions. *Rev. Mod. Phys.*, 68:13–125, Jan 1996. DOI: 10.1103/RevModPhys.68.13. URL http://link.aps.org/doi/10.1103/RevModPhys.68.13.

G. Ghiringhelli, M. Le Tacon, M. Minola, S. Blanco-Canosa, C. Mazzoli, N. B. Brookes, G. M. De Luca, A. Frano, D. G. Hawthorn, F. He, T. Loew, M. Moretti Sala, D. C. Peets, M. Salluzzo, E. Schierle, R. Sutarto, G. A. Sawatzky, E. Weschke, B. Keimer,

and L. Braicovich. Long-range incommensurate charge fluctuations in (y,nd)ba2cu3o6+x. *Science*, 337(6096):821–825, 2012. DOI: 10.1126/science.1223532. URL http://www.sciencemag.org/content/337/6096/821.abstract.

Claudio Giannetti, Giacomo Coslovich, Federico Cilento, Gabriele Ferrini, Hiroshi Eisaki, Nobuhisa Kaneko, Martin Greven, and Fulvio Parmigiani. Discontinuity of the ultrafast electronic response of underdoped superconducting $bi_2sr_2cacu_2o_{8+\delta}$ strongly excited by ultrashort light pulses. *Phys. Rev. B*, 79:224502, Jun 2009. DOI: 10.1103/PhysRevB.79.224502. URL http://link.aps.org/doi/10.1103/PhysRevB.79.224502.

Claudio Giannetti, Federico Cilento, Stefano Dal Conte, Giacomo Coslovich, Gabriele Ferrini, Hajo Molegraaf, Markus Raichle, Ruixing Liang, Hiroshi Eisaki, Martin Greven, Andrea Damascelli, Dirk van der Marel, and Fulvio Parmigiani. Revealing the high-energy electronic excitations underlying the onset of high-temperature superconductivity in cuprates. *Nat Commun*, 2:353, 06 2011. URL http://dx.doi.org/10.1038/ncomms1354.

J. A. Giordmaine and Robert C. Miller. Tunable coherent parametric oscillation in $linbo_3$ at optical frequencies. *Phys. Rev. Lett.*, 14:973–976, Jun 1965. DOI: 10.1103/PhysRevLett.14.973. URL http://link.aps.org/doi/10.1103/PhysRevLett.14.973.

Denis Golež, Janez Bonča, Marcin Mierzejewski, and Lev Vidmar. Mechanism of ultrafast relaxation of a photo-carrier in antiferromagnetic spin background. *Phys. Rev. B*, 89:165118, Apr 2014. DOI: 10.1103/PhysRevB.89.165118. URL http://link.aps.org/doi/10.1103/PhysRevB.89.165118.

A. Gozar, G. Logvenov, L. Fitting Kourkoutis, A. T. Bollinger, L. A. Giannuzzi, D. A. Muller, and I. Bozovic. High-temperature interface superconductivity between metallic and insulating copper oxides. *Nature*, 455(7214):782–785, 10 2008. URL http://dx.doi.org/10.1038/nature07293.

Giuseppe Grosso and Giuseppe Pastori Parravicini. *Preface*. Academic Press, London, 2000. ISBN 978-0-12-304460-0. DOI: http://dx.doi.org/10.1016/B978-012304460-0/50000-1. URL http://www.sciencedirect.com/science/article/pii/B9780123044600500001.

R. Hayn, H. Rosner, V. Yushankhai, S. Haffner, C. Dürr, M. Knupfer, G. Krabbes, M. Golden, J. Fink, H. Eschrig, D. Singh, N. Hien, A. Menovsky, Ch. Jung, and G. Reichardt. Analysis of the

valence-band photoemission spectrum of $sr_2cuo_2cl_2$ along the high-symmetry directions. *Phys. Rev. B*, 60:645–658, Jul 1999. DOI: 10.1103/PhysRevB.60.645. URL http://link.aps.org/doi/10.1103/PhysRevB.60.645.

Rui-Hua He, M. Hashimoto, H. Karapetyan, J. D. Koralek, J. P. Hinton, J. P. Testaud, V. Nathan, Y. Yoshida, Hong Yao, K. Tanaka, W. Meevasana, R. G. Moore, D. H. Lu, S. K. Mo, M. Ishikado, H. Eisaki, Z. Hussain, T. P. Devereaux, S. A. Kivelson, J. Orenstein, A. Kapitulnik, and Z. X. Shen. From a single-band metal to a high-temperature superconductor via two thermal phase transitions. *Science*, 331(6024):1579–1583, 03 2011. URL http://www.sciencemag.org/content/331/6024/1579.abstract.

C. C. Homes, T. Timusk, R. Liang, D. A. Bonn, and W. N. Hardy. Optical conductivity of c axis oriented $yba_2cu_3o_{6.70}$: Evidence for a pseudogap. *Phys. Rev. Lett.*, 71:1645–1648, Sep 1993. DOI: 10.1103/PhysRevLett.71.1645. URL http://link.aps.org/doi/10.1103/PhysRevLett.71.1645.

J. Hubbard. Electron correlations in narrow energy bands. ii. the degenerate band case. *Proceedings of the Royal Society of London. Series A. Mathematical and Physical Sciences*, 277 (1369):237–259, 1964. DOI: 10.1098/rspa.1964.0019. URL http://rspa.royalsocietypublishing.org/content/277/1369/237.abstract.

J. and Hubbard. Electron correlations in narrow energy bands. *Proceedings of the Royal Society of London A: Mathematical, Physical and Engineering Sciences*, 276(1365):238–257, 11 1963. URL http://rspa.royalsocietypublishing.org/content/276/1365/238.abstract.

S. Hüfner. *Photoelectron Spectroscopy: Principles and Applications*. Springer-Verlag, 1995. ISBN 9780387191089. URL http://books.google.it/books?id=Xt_FQgAACAAJ.

N E Hussey. Phenomenology of the normal state in-plane transport properties of high- t c cuprates. *Journal of Physics: Condensed Matter*, 20(12):123201, 2008. URL http://stacks.iop.org/0953-8984/20/i=12/a=123201.

J. Hwang, T. Timusk, E. Schachinger, and J. P. Carbotte. Evolution of the bosonic spectral density of the high-temperature superconductor $bi_2sr_2Cacu_2o_{8+\delta}$. *Phys. Rev. B*, 75:144508, Apr 2007. DOI: 10.1103/PhysRevB.75.144508. URL http://link.aps.org/doi/10.1103/PhysRevB.75.144508.

Masatoshi Imada, Atsushi Fujimori, and Yoshinori Tokura. Metal-insulator transitions. *Rev. Mod. Phys.*, 70:1039–1263, Oct 1998. DOI: 10.1103/RevModPhys.70.1039. URL http://link.aps.org/doi/10.1103/RevModPhys.70.1039.

K. Ishii, I. Jarrige, M. Yoshida, K. Ikeuchi, J. Mizuki, K. Ohashi, T. Takayama, J. Matsuno, and H. Takagi. Momentum-resolved electronic excitations in the mott insulator sr_2iro_4 studied by resonant inelastic x-ray scattering. *Phys. Rev. B*, 83:115121, Mar 2011. DOI: 10.1103/PhysRevB.83.115121. URL http://link.aps.org/doi/10.1103/PhysRevB.83.115121.

T. Ito, K. Takenaka, and S. Uchida. Systematic deviation from t-linear behavior in the in-plane resistivity of $yba_2cu_3o_{7-y}$: Evidence for dominant spin scattering. *Phys. Rev. Lett.*, 70:3995–3998, Jun 1993. DOI: 10.1103/PhysRevLett.70.3995. URL http://link.aps.org/doi/10.1103/PhysRevLett.70.3995.

S. Johnston. Evidence for forward scattering and coupling to acoustic phonon modes in high-tc cuprate superconductors. http://arxiv.org/pdf/1101.1302.pdf, 2011.

Masato Kakihana, Minoru Osada, Mikael Käll, Lars Börjesson, Hiromasa Mazaki, Hiroshi Yasuoka, Masatomo Yashima, and Masahiro Yoshimura. Raman-active phonons in $bi_2sr_2ca_{1-x}y_xcu_2o_{8+d}$ (x =0–1): Effects of hole filling and internal pressure induced by y doping for ca, and implications for phonon assignments. *Phys. Rev. B*, 53:11796–11806, May 1996. DOI: 10.1103/PhysRevB.53.11796. URL http://link.aps.org/doi/10.1103/PhysRevB.53.11796.

B. J. Kim, Hosub Jin, S. J. Moon, J.-Y. Kim, B.-G. Park, C. S. Leem, Jaejun Yu, T. W. Noh, C. Kim, S.-J. Oh, J.-H. Park, V. Durairaj, G. Cao, and E. Rotenberg. Novel $J_{\text{eff}} = 1/2$ mott state induced by relativistic spin-orbit coupling in sr_2iro_4. *Phys. Rev. Lett.*, 101: 076402, Aug 2008. DOI: 10.1103/PhysRevLett.101.076402. URL http://link.aps.org/doi/10.1103/PhysRevLett.101.076402.

B. J. Kim, H. Ohsumi, T. Komesu, S. Sakai, T. Morita, H. Takagi, and T. Arima. Phase-sensitive observation of a spin-orbital mott state in sr2iro4. *Science*, 323(5919):1329–1332, 2009. DOI: 10.1126/science.1167106. URL http://www.sciencemag.org/content/323/5919/1329.abstract.

Charles Kittel. *Introduction to Solid State Physics*. John Wiley & Sons, Inc., New York, 6th edition, 1986.

J. D. Koralek, J. F. Douglas, N. C. Plumb, Z. Sun, A. V. Fedorov, M. M. Murnane, H. C. Kapteyn, S. T. Cundiff, Y. Aiura, K. Oka,

H. Eisaki, and D. S. Dessau. Laser based angle-resolved photoemission, the sudden approximation, and quasiparticle-like spectral peaks in $bi_2sr_2cacu_2o_{8+\delta}$. *Phys. Rev. Lett.*, 96:017005, Jan 2006. DOI: 10.1103/PhysRevLett.96.017005. URL http://link.aps.org/doi/10.1103/PhysRevLett.96.017005.

A. A. Kordyuk, S. V. Borisenko, M. S. Golden, S. Legner, K. A. Nenkov, M. Knupfer, J. Fink, H. Berger, L. Forró, and R. Follath. Doping dependence of the fermi surface in $(Bi,Pb)_2sr_2cacu_2o_{8+\delta}$. *Phys. Rev. B*, 66:014502, Jun 2002. DOI: 10.1103/PhysRevB.66.014502. URL http://link.aps.org/doi/10.1103/PhysRevB.66.014502.

N. N. Kovaleva, A. V. Boris, T. Holden, C. Ulrich, B. Liang, C. T. Lin, B. Keimer, C. Bernhard, J. L. Tallon, D. Munzar, and A. M. Stoneham. *c*. *Phys. Rev. B*, 69:054511, Feb 2004. DOI: 10.1103/PhysRevB.69.054511. URL http://link.aps.org/doi/10.1103/PhysRevB.69.054511.

M. J. Lawler, K. Fujita, Jhinhwan Lee, A. R. Schmidt, Y. Kohsaka, Chung Koo Kim, H. Eisaki, S. Uchida, J. C. Davis, J. P. Sethna, and Eun-Ah Kim. Intra-unit-cell electronic nematicity of the high-tc copper-oxide pseudogap states. *Nature*, 466(7304):347–351, 07 2010. URL http://dx.doi.org/10.1038/nature09169.

Y. S. Lee, Kouji Segawa, Z. Q. Li, W. J. Padilla, M. Dumm, S. V. Dordevic, C. C. Homes, Yoichi Ando, and D. N. Basov. Electrodynamics of the nodal metal state in weakly doped high-T_c cuprates. *Phys. Rev. B*, 72:054529, Aug 2005. DOI: 10.1103/PhysRevB.72.054529. URL http://link.aps.org/doi/10.1103/PhysRevB.72.054529.

Zala Lenarčič and Peter Prelovšek. Ultrafast charge recombination in a photoexcited mott-hubbard insulator. *Phys. Rev. Lett.*, 111:016401, Jul 2013. DOI: 10.1103/PhysRevLett.111.016401. URL http://link.aps.org/doi/10.1103/PhysRevLett.111.016401.

A. G. Loeser, Z.-X. Shen, D. S. Dessau, D. S. Marshall, C. H. Park, P. Fournier, and A. Kapitulnik. Excitation gap in the normal state of underdoped bi2sr2cacu208+Î´. *Science*, 273(5273):325–329, 1996. DOI: 10.1126/science.273.5273.325. URL http://www.sciencemag.org/content/273/5273/325.abstract.

S. Lupi, D. Nicoletti, O. Limaj, L. Baldassarre, M. Ortolani, S. Ono, Yoichi Ando, and P. Calvani. Far-infrared absorption and the metal-to-insulator transition in hole-doped cuprates. *Phys. Rev. Lett.*, 102:206409, May 2009. DOI: 10.1103/PhysRevLett.102.206409. URL http://link.aps.org/doi/10.1103/PhysRevLett.102.206409.

Cristian Manzoni, Dario Polli, and Giulio Cerullo. Two-color pump-probe system broadly tunable over the visible and the near infrared with sub-30fs temporal resolution. *Review of Scientific Instruments*, 77 (2):023103, 2006. DOI: http://dx.doi.org/10.1063/1.2167128. URL http://scitation.aip.org/content/aip/journal/rsi/77/2/10.1063/1.2167128.

D. S. Marshall, D. S. Dessau, A. G. Loeser, C-H. Park, A. Y. Matsuura, J. N. Eckstein, I. Bozovic, P. Fournier, A. Kapitulnik, W. E. Spicer, and Z.-X. Shen. Unconventional electronic structure evolution with hole doping in $bi_2sr_2cacu_2O_{8+\delta}$: Angle-resolved photoemission results. *Phys. Rev. Lett.*, 76:4841–4844, Jun 1996. DOI: 10.1103/PhysRevLett.76.4841. URL http://link.aps.org/doi/10.1103/PhysRevLett.76.4841.

F. Marsiglio and J. P. Carbotte. Electron - Phonon Superconductivity. *eprint arXiv:cond-mat/0106143*, June 2001.

S. Martin, A. T. Fiory, R. M. Fleming, L. F. Schneemeyer, and J. V. Waszczak. Normal-state transport properties of $bi_{2+x}sr_{2-y}cuo_{6+ffi}$ crystals. *Phys. Rev. B*, 41:846–849, Jan 1990. DOI: 10.1103/PhysRevB.41.846. URL http://link.aps.org/doi/10.1103/PhysRevB.41.846.

L. Mattheiss and D. Hamann. Oxygen hole symmetry and banding in cuprate superconductors. *Phys. Rev. B*, 40:2217–2224, Aug 1989. DOI: 10.1103/PhysRevB.40.2217. URL http://link.aps.org/doi/10.1103/PhysRevB.40.2217.

S. J. Moon, Hosub Jin, W. S. Choi, J. S. Lee, S. S. A. Seo, J. Yu, G. Cao, T. W. Noh, and Y. S. Lee. Temperature dependence of the electronic structure of the $J_{\text{eff}} = \frac{1}{2}$ mott insulator sr_2iro_4 studied by optical spectroscopy. *Phys. Rev. B*, 80:195110, Nov 2009. DOI: 10.1103/PhysRevB.80.195110. URL http://link.aps.org/doi/10.1103/PhysRevB.80.195110.

Mott and Peierls. Discussion of the paper by de boer and verwey. *Proceedings of the Royal Society of London. Series A. Mathematical and Physical Sciences*, 49(4S):72, 1937.

N F Mott. The basis of the electron theory of metals, with special reference to the transition metals. *Proceedings of the Physical Society. Section A*, 62(7):416, 1949. URL http://stacks.iop.org/0370-1298/62/i=7/a=303.

Hiroki Nakano, Yoshinori Takahashi, and Masatoshi Imada. Drude weight of the two-dimensional hubbard model –reexamination of finite-size effect in exact diagonalization study–. *Journal of the Physical*

Society of Japan, 76(3):034705, 2007. DOI: 10.1143/JPSJ.76.034705. URL http://dx.doi.org/10.1143/JPSJ.76.034705.

M. R. Norman and A. V. Chubukov. High-frequency behavior of the infrared conductivity of cuprates. *Phys. Rev. B*, 73:140501, Apr 2006. DOI: 10.1103/PhysRevB.73.140501. URL http://link.aps.org/doi/10.1103/PhysRevB.73.140501.

M. R. Norman, H. Ding, M. Randeria, J. C. Campuzano, T. Yokoya, T. Takeuchi, T. Takahashi, T. Mochiku, K. Kadowaki, P. Guptasarma, and D. G. Hinks. Destruction of the fermi surface in underdoped high-tc superconductors. *Nature*, 392(6672):157–160, 03 1998. URL http://dx.doi.org/10.1038/32366.

Masao Ogata and Hidetoshi Fukuyama. The t – j model for the oxide high- t c superconductors. *Reports on Progress in Physics*, 71(3):036501, 2008. URL http://stacks.iop.org/0034-4885/71/i=3/a=036501.

Hiroaki Onishi. Spin-orbital state induced by strong spin-orbit coupling. *Journal of Physics: Conference Series*, 391, 2012.

S. Ono and Yoichi Ando. Evolution of the resistivity anisotropy in $Cu-O$ layer cuprate $Bi_2Sr_{2-x}La_xCuO_{6+\delta}$ single crystals for a wide range of hole doping. *Phys. Rev. B*, 67:104512, Mar 2003. DOI: 10.1103/PhysRevB.67.104512. URL http://link.aps.org/doi/10.1103/PhysRevB.67.104512.

Joseph Orenstein, G. A. Thomas, A. J. Millis, S. L. Cooper, D. H. Rapkine, T. Timusk, L. F. Schneemeyer, and J. V. Waszczak. Frequency- and temperature-dependent conductivity in $yba_2cu_3o_{6+x}$ crystals. *Phys. Rev. B*, 42:6342–6362, Oct 1990. DOI: 10.1103/PhysRevB.42.6342. URL http://link.aps.org/doi/10.1103/PhysRevB.42.6342.

Chan Park and Robert L. Snyder. Structures of high-temperature cuprate superconductors. *Journal of the American Ceramic Society*, 78(12):3171–3194, 1995. ISSN 1551-2916. DOI: 10.1111/j.1151-2916.1995.tb07953.x. URL http://dx.doi.org/10.1111/j.1151-2916.1995.tb07953.x.

N. Plakida. *High-Temperature Cuprate Superconductors: Experiment, Theory, and Applications*. Springer Series in Solid-State Sciences. Springer, 2010. ISBN 9783642126338. URL http://books.google.co.uk/books?id=6h253TfrKYUC.

A V Puchkov, D N Basov, and T Timusk. The pseudogap state in high-t_c superconductors: an infrared study. *Journal of Physics:*

Condensed Matter, 8(48):10049, 1996. URL http://stacks.iop.org/0953-8984/8/i=48/a=023.

Murray K. Reed, Michael K. Steiner-Shepard, and Daniel K. Negus. Widely tunable femtosecond optical parametric amplifier at 250 khz with a ti:sapphire regenerative amplifier. *Opt. Lett.*, 19(22): 1855–1857, Nov 1994. DOI: 10.1364/OL.19.001855. URL http://ol.osa.org/abstract.cfm?URI=ol-19-22-1855.

Ch. Renner, B. Revaz, J.-Y. Genoud, K. Kadowaki, and Ø. Fischer. Pseudogap precursor of the superconducting gap in under- and overdoped $bi_2sr_2cacu_2O_{8+\delta}$. *Phys. Rev. Lett.*, 80:149–152, Jan 1998. DOI: 10.1103/PhysRevLett.80.149. URL http://link.aps.org/doi/10.1103/PhysRevLett.80.149.

J. Rohler. Nonlinear doping of cuprates superconductor - the case of $Bi_2Sr_{2-x}La_xCuO_{6+\delta}$. *Physica C: Superconductivity*, 470(1):S39–S41, 2020.

S. Sachdev. *Quantum Phase Transitions*. Cambridge University Press, 2001. ISBN 9780521004541. URL http://books.google.it/books?id=Ih_E05N5TZQC.

G. A. Sawatzky. Testing fermi-liquid models. *Nature*, 342(6249):480–481, 11 1989. URL http://dx.doi.org/10.1038/342480a0.

D. J. Scalapino, E. Loh, and J. E. Hirsch. $d-$wave pairing near a spin-density-wave instability. *Phys. Rev. B*, 34:8190–8192, Dec 1986. DOI: 10.1103/PhysRevB.34.8190. URL http://link.aps.org/doi/10.1103/PhysRevB.34.8190.

M. P. Seah and W. A. Dench. Quantitative electron spectroscopy of surfaces: A standard data base for electron inelastic mean free paths in solids. *Surface and Interface Analysis*, 1(1):2–11, 1979. ISSN 1096-9918. DOI: 10.1002/sia.740010103. URL http://dx.doi.org/10.1002/sia.740010103.

1911-2008 Seitz, Frederick. *The modern theory of solids*. McGraw-Hill Book Company, inc., New York, London, 1940. URL http://search.library.wisc.edu/catalog/ocm00534858.

K. Shen, F. Ronning, D. Lu, W. Lee, N. Ingle, W. Meevasana, F. Baumberger, A. Damascelli, N. Armitage, L. Miller, Y. Kohsaka, M. Azuma, M. Takano, H. Takagi, and Z.-X. Shen. Missing quasiparticles and the chemical potential puzzle in the doping evolution of the cuprate superconductors. *Phys. Rev. Lett.*, 93:267002, Dec 2004. DOI: 10.1103/PhysRevLett.93.267002. URL http://link.aps.org/doi/10.1103/PhysRevLett.93.267002.

Y.R. Shen. *The principles of nonlinear optics*. Wiley classics library. Wiley-Interscience, 2003. ISBN 9780471430803. URL http://books.google.it/books?id=xeg9AQAAIAAJ.

Akira Shirakawa, Isao Sakane, and Takayoshi Kobayashi. Pulse-front-matched optical parametric amplification for sub-10-fs pulse generation tunable in the visible and near infrared. *Opt. Lett.*, 23(16):1292–1294, Aug 1998. DOI: 10.1364/OL.23.001292. URL http://ol.osa.org/abstract.cfm?URI=ol-23-16-1292.

N. V. Smith, P. Thiry, and Y. Petroff. Photoemission linewidths and quasiparticle lifetimes. *Phys. Rev. B*, 47:15476–15481, Jun 1993. DOI: 10.1103/PhysRevB.47.15476. URL http://link.aps.org/doi/10.1103/PhysRevB.47.15476.

E.M. Stoudenmire and Steven R. White. Studying two-dimensional systems with the density matrix renormalization group. *Annual Review of Condensed Matter Physics*, 3(1):111–128, 2012. DOI: 10.1146/annurev-conmatphys-020911-125018. URL http://dx.doi.org/10.1146/annurev-conmatphys-020911-125018.

S. Tajima, T. Noda, H. Eisaki, and S. Uchida. *c*-axis optical response in the static stripe ordered phase of the cuprates. *Phys. Rev. Lett.*, 86:500–503, Jan 2001. DOI: 10.1103/PhysRevLett.86.500. URL http://link.aps.org/doi/10.1103/PhysRevLett.86.500.

J.L. Tallon, G.V.M. Williams, M.P. Staines, and C. Bernhard. Energy and length scales in the superconducting phase diagram for {HTSC} cuprates. *Physica C: Superconductivity*, 235–240, Part 3(0):1821 – 1822, 1994. ISSN 0921-4534. DOI: http://dx.doi.org/10.1016/0921-4534(94)92132-6. URL http://www.sciencedirect.com/science/article/pii/0921453494921326.

I. Terasaki, S. Tajima, H. Eisaki, H. Takagi, K. Uchinokura, and S. Uchida. Optical reflectivity spectra of single-crystal $bi_2sr_2ca_{n-1}cu_no_{2n+4+x}$ (n=1 and 2). *Phys. Rev. B*, 41:865–868, Jan 1990. DOI: 10.1103/PhysRevB.41.865. URL http://link.aps.org/doi/10.1103/PhysRevB.41.865.

M. Tinkham. *Introduction to Superconductivity: Second Edition*. Dover Books on Physics. Dover Publications, 2004. ISBN 9780486435039. URL http://books.google.it/books?id=k6AO9nRYbioC.

J. M. Tranquada, B. J. Sternlieb, J. D. Axe, Y. Nakamura, and S. Uchida. Evidence for stripe correlations of spins and holes in copper oxide superconductors. *Nature*, 375(6532):561–563, 06 1995. URL http://dx.doi.org/10.1038/375561a0.

C. C. Tsuei and J. R. Kirtley. Pairing symmetry in cuprate superconductors. *Rev. Mod. Phys.*, 72:969–1016, Oct 2000. DOI: 10.1103/RevModPhys.72.969. URL http://link.aps.org/doi/10.1103/RevModPhys.72.969.

A. M. Tsvelik and A. V. Chubukov. Composite charge order in the pseudogap region of the cuprates. *Phys. Rev. B*, 89:184515, May 2014. DOI: 10.1103/PhysRevB.89.184515. URL http://link.aps.org/doi/10.1103/PhysRevB.89.184515.

P. Tzankov, I. Buchvarov, and T. Fiebig. Broadband optical parametric amplification in the near uv–vis. *Optics Communications*, 203(1–2):107 – 113, 2002. ISSN 0030-4018. DOI: http://dx.doi.org/10.1016/S0030-4018(02)01107-0. URL http://www.sciencedirect.com/science/article/pii/S0030401802011070.

Pancho Tzankov, Jiaan Zheng, Mark Mero, Dario Polli, Cristian Manzoni, and Giulio Cerullo. 300 μj noncollinear optical parametric amplifier in the visible at 1 khz repetition rate. *Opt. Lett.*, 31(24): 3629–3631, Dec 2006. DOI: 10.1364/OL.31.003629. URL http://ol.osa.org/abstract.cfm?URI=ol-31-24-3629.

S. Uchida, T. Ido, H. Takagi, T. Arima, Y. Tokura, and S. Tajima. Optical spectra of $la_{2-x}sr_xcuo_4$: Effect of carrier doping on the electronic structure of the cuo_2 plane. *Phys. Rev. B*, 43:7942–7954, Apr 1991. DOI: 10.1103/PhysRevB.43.7942. URL http://link.aps.org/doi/10.1103/PhysRevB.43.7942.

S. Uchida, K. Tamasaku, and S. Tajima. *c*-axis optical spectra and charge dynamics in $La_{2-x}Sr_xCuO_4$. *Phys. Rev. B*, 53:14558–14574, Jun 1996. DOI: 10.1103/PhysRevB.53.14558. URL http://link.aps.org/doi/10.1103/PhysRevB.53.14558.

E. van Heumen. Doping-dependent optical properties of bi2201 doping-dependent optical properties of bi2201 doping-dependent optical properties of bi2201 doping-dependent optical properties of bi2201. *New J. Phys*, 11(055067), 2009.

M. A. van Veenendaal and G. A. Sawatzky. Doping dependence of Ni2p x-ray-absorption spectra of $M_xni_{1-x}O$ (m = Li, Na). *Phys. Rev. B*, 50:11326–11331, Oct 1994. DOI: 10.1103/PhysRevB.50.11326. URL http://link.aps.org/doi/10.1103/PhysRevB.50.11326.

C. Varma. Theory of the pseudogap state of the cuprates. *Phys. Rev. B*, 73:155113, Apr 2006. DOI: 10.1103/PhysRevB.73.155113. URL http://link.aps.org/doi/10.1103/PhysRevB.73.155113.

C. M. Varma. Non-fermi-liquid states and pairing instability of a general model of copper oxide metals. *Phys. Rev. B*, 55:14554–14580, Jun 1997. DOI: 10.1103/PhysRevB.55.14554. URL http://link.aps.org/doi/10.1103/PhysRevB.55.14554.

C. M. Varma, P. B. Littlewood, S. Schmitt-Rink, E. Abrahams, and A. E. Ruckenstein. Phenomenology of the normal state of cu-o high-temperature superconductors. *Phys. Rev. Lett.*, 63:1996–1999, Oct 1989. DOI: 10.1103/PhysRevLett.63.1996. URL http://link.aps.org/doi/10.1103/PhysRevLett.63.1996.

I. M. Vishik, M. Hashimoto, Rui-Hua He, Wei-Sheng Lee, Felix Schmitt, Donghui Lu, R. G. Moore, C. Zhang, W. Meevasana, T. Sasagawa, S. Uchida, Kazuhiro Fujita, S. Ishida, M. Ishikado, Yoshiyuki Yoshida, Hiroshi Eisaki, Zahid Hussain, Thomas P. Devereaux, and Zhi-Xun Shen. Phase competition in trisected superconducting dome. *Proceedings of the National Academy of Sciences*, 109(45):18332–18337, 2012. DOI: 10.1073/pnas.1209471109. URL http://www.pnas.org/content/109/45/18332.abstract.

Yuxuan Wang and Andrey Chubukov. Charge-density-wave order with momentum $(2q, 0)$ and $(0, 2q)$ within the spin-fermion model: Continuous and discrete symmetry breaking, preemptive composite order, and relation to pseudogap in hole-doped cuprates. *Phys. Rev. B*, 90:035149, Jul 2014. DOI: 10.1103/PhysRevB.90.035149. URL http://link.aps.org/doi/10.1103/PhysRevB.90.035149.

W. W. Warren, R. E. Walstedt, G. F. Brennert, R. J. Cava, R. Tycko, R. F. Bell, and G. Dabbagh. Cu spin dynamics and superconducting precursor effects in planes above T_c in $yba_2cu_3o_{6.7}$. *Phys. Rev. Lett.*, 62:1193–1196, Mar 1989. DOI: 10.1103/PhysRevLett.62.1193. URL http://link.aps.org/doi/10.1103/PhysRevLett.62.1193.

William Witczak-Krempa, Gang Chen, Yong Baek Kim, and Leon Balents. Correlated quantum phenomena in the strong spin-orbit regime. *Annual Review of Condensed Matter Physics*, 5(1):57–82, 2014. DOI: 10.1146/annurev-conmatphys-020911-125138. URL http://dx.doi.org/10.1146/annurev-conmatphys-020911-125138.

Jing Xia, Elizabeth Schemm, G. Deutscher, S. A. Kivelson, D. A. Bonn, W. N. Hardy, R. Liang, W. Siemons, G. Koster, M. M. Fejer, and A. Kapitulnik. Polar kerr-effect measurements of the high-temperature $yba_2cu_3o_{6+x}$ superconductor: Evidence for broken symmetry near the pseudogap temperature. *Phys. Rev. Lett.*, 100:127002, Mar 2008. DOI: 10.1103/PhysRevLett.100.127002. URL http://link.aps.org/doi/10.1103/PhysRevLett.100.127002.

J. Zaanen, G. A. Sawatzky, and J. W. Allen. Band gaps and electronic structure of transition-metal compounds. *Phys. Rev. Lett.*, 55:418–421, Jul 1985. DOI: 10.1103/PhysRevLett.55.418. URL http://link.aps.org/doi/10.1103/PhysRevLett.55.418.

Jan Zaanen and Olle Gunnarsson. Charged magnetic domain lines and the magnetism of high-T_c oxides. *Phys. Rev. B*, 40:7391–7394, Oct 1989. DOI: 10.1103/PhysRevB.40.7391. URL http://link.aps.org/doi/10.1103/PhysRevB.40.7391.

F. C. Zhang and T. M. Rice. Effective hamiltonian for the superconducting cu oxides. *Phys. Rev. B*, 37:3759–3761, Mar 1988. DOI: 10.1103/PhysRevB.37.3759. URL http://link.aps.org/doi/10.1103/PhysRevB.37.3759.

Junjing Zhao, Utpal Chatterjee, Dingfei Ai, David G. Hinks, Hong Zheng, G. D. Gu, John-Paul Castellan, Stephan Rosenkranz, Helmut Claus, Michael R. Norman, Mohit Randeria, and Juan Carlos Campuzano. Universal features in the photoemission spectroscopy of high-temperature superconductors. *Proceedings of the National Academy of Sciences*, 110(44):17774–17777, 2013. DOI: 10.1073/pnas.1302932110. URL http://www.pnas.org/content/110/44/17774.abstract.

List of Publications

A. Aronne, E. Fanelli, P. Pernice, S. Peli, C. Giannetti, G. Ferrini. Crystallization and second harmonic generation in potassium sodium niobiosilicate glasses. *Journal of Solid State Chemistry* **182**, (2009)

F. Cilento, S. Dal Conte, G. Coslovich, S. Peli, N. Nembrini, S. Mor, F. Banfi, G. Ferrini, H. Eisaki, M. K. Chan, C. J. Dorow, M. J. Veit, M. Greven, D. van der Marel, R. Comin, A. Damascelli, L. Rettig, U. Bovensiepen, M. Capone, C. Giannetti & F. Parmigiani. Photo-enhanced antinodal conductivity in the pseudogap state of high-T_C cuprates. *Nature Communications* **5**, (2014)

S. Dal Conte, L. Vidmar, D. Golez, M. Mierzejewski, G. Soavi, S. Peli, F. Banfi, G. Ferrini, R. Comin, B. Ludbrook, L. ChauviÃ¨re, N. Zhigadlo, H. Eisaki, M. Greven, S. Lupi, A. Damascelli, D. Brida, M. Capone, J. Bonca, G. Cerullo & C. Giannetti. Snapshots of the retarded interaction of charge carriers with ultrafast fluctuations in cuprates. *Accepted for publication on Nature Physics* (January 2015)

S. Peli et al. Transition from localized to delocalized high-energy excitations as the mechanism originating the low-temperature quantum critical point of cuprates. *In preparation*.

S. Peli et al. Ultrafast dynamics of the O-2p bands in Bi2212. *In preparation*.

Acknowledgements

I would like to thank the following people for their contributions to the present work:
POLITECNICO DI MILANO: Stefano Dal Conte, Giulio Cerullo and Daniele Brida for their help in performing measurements with their OPA-based setup.
UNIVERSITY OF BRITISH COLUMBIA: Andrea Damascelli, Riccardo Comin and Giorgio Levy for the ARPES measurements and for giving me the opportunity to develop a laser-ARPES system and for the precious help not only in photoemission. Thanks also for providing us the Bi2212 samples. David Jones and Arthur Mills for their hints on the optical part of the laser-ARPES system. Mona Berciu and George Sawatzky for the theoretical and interpretative aspects of the experimental data on Bi2212.
SISSA (TRIESTE): Massimo Capone, who accepted to be the referee of this work, for theoretical calculations of the optical conductivity of Bi2201 via DMFT theory.
ELETTRA (TRIESTE): Federico Cilento, ALberto Crepaldi and Fluvio Parmiginai for the precious help in performing time-resolved ARPES measurements with the XUV photoemission system of the ARTEMIS Lab at the Central Laser Facility.
CENTRAL LASER FACILITY (RUTHERFORD-APPLETON LABORATORIES - UK): Cephise Cacho and Emma Springate for their useful presence during the XUV-photoemission experiments at the ARTEMIS beamline.
SAPIENZA UNIVERSITA' DI ROMA: Stefano Lupi for providing the Bi2201 samples with different doping concentrations.